Numerical Analysis of a Nonlinear Mechanical-Electrical-Acoustical Model of the Cochlea

by

Amir Nankali

A dissertation submitted in partial fulfillment
of the requirements for the degree of
Doctor of Philosophy
(Mechanical Engineering)
in The University of Michigan
2018

Doctoral Committee:

Professor Karl Grosh, Chair
Professor Daniel J. Inman
Associate Professor Elizabeth S. Olson
Professor Noel Perkins
Assistant Professor Bogdan I. Popa

nankali@umich.edu

ORCID ID: 0000-0003-3076-4389

This thesis is dedicated to my wife and my parents

ACKNOWLEDGEMENTS

First and foremost, I am grateful to God for the good health and wellbeing that were necessary to complete this project.

I am extremely grateful to my advisor Dr. Karl Grosh for introducing me to the fascinating research topic of the auditory system and for his invaluable guidance and support throughout this project. A very special thanks to Dr. Elizabeth S. Olson for hosting me in her lab at the University of Columbia and for the valuable experimental training I received. My sincere thanks also goes to my committee members, Dr. Daniel J. Inman, Dr. Noel Perkins and Dr. Bogdan I. Popa for their valuable time and all their support. I thank my fellow labmates in the Acoustic and Vibrations lab for the stimulating discussions and for all their help and support. In particular, I am grateful to Dr. Julien Meaud, Aritra Sasmal and Yi Wang for their valuable advice in modeling and experimentation.

Last but not the least, I would like to thank my family: my wife and my parents for supporting me spiritually throughout writing this thesis and my life in general.

TABLE OF CONTENTS

LIST OF FIGURES

Figure

LIST OF TABLES

Table

LIST OF APPENDICES

Appendix

LIST OF ABBREVIATIONS

TM tectorial membrane

BM basilar membrane

HB hair bundle

OHC outer hair cell

OoC organ of Corti

MET mechanoelectric transducer

RL reticular lamina

SPL sound pressure level

CF characteristic frequency

ST scala tympani

SM scala media

SV scala vestibuli

ABSTRACT

The overarching goal of my research project is to develop a computational model of the mammalian auditory system to gain a deeper underestimating of the mechanics of hearing. This model describes the response of the cochlea to both external acoustic and internal electrical stimulations. The cochlea is the spiral-shaped part of the inner ear where the fluid-borne vibrations are detected by the auditory sensors and then the information, in the form of neural signals, are transferred to the brain by the auditory nerves. The cochlear model will enhance our understanding of failure mechanisms in the cochlea, answering important questions as to the morphological elements of the cochlea that fail and why. A mathematical model of the cochlear response to sound over the entire spectrum will help us understand how important classes of signals are processed in the cochlea (such as speech and music) which can lead to better speech processing algorithms or cochlear implant electrical stimulation paradigms.

One important question in the biophysics of the cochlea is the underlying mechanism of the cochlear active process which enables sound processing over a broad range of frequencies and intensities. Two mechanisms are hypothesized as the main active processes: outer hair cell (OHC) somatic electromotility and hair bundle (HB) motility. The proposed active mechanisms are implemented into our model and their relative contribution on the cochlear nonlinear amplifier is investigated. It is shown that somatic based activity plays a fundamental role in the amplifier while the HB motility contribution remains elusive. We identify two distinct mechanisms through

which the HB activity affects the cochlear dynamics. We posit that it is unlikely that the HB alone is responsible for the amplification seen in the cochlea *in vivo*.

The extracellular voltage is shown to undergo a phase shift at frequencies slightly below the peak, that coincides with the onset of the nonlinear amplification. It is hypothesized that this phase difference between the electrical and mechanical responses gives rise to effective power generation of the OHC somatic force. A three-dimensional model of the cochlea is utilized along with experimental data and it is shown that the electro-mechanical phase transition, generated by the tectorial membrane (TM) shear mechanics, activates the cochlear nonlinear amplifier.

Using the excised cochlear segment experiment conducted by Chan and Hudspeth [3–5] as our model problem, we develop a quasilinear computational model for studying the active *in vitro* response of the organ of Corti (OoC) to acoustical stimulation. It is shown that our model of the electrical, mechanical, and acoustical conditions of the experimental configuration is able to replicate the important finding of these experiments while our interpretation of the results contradicts the Chan and Hudspeth conclusion. It is shown that the OHC somatic electromotility, rather that HB motility, is sufficient to predict the nonlinearities observed in the these experiments.

CHAPTER I

Introduction

The cochlea's primary function is to transduce sound-evoked motions into neural signals which will be processed by the brain. Sound detection takes place within the sensory receptors of the organ of Corti (OoC), situated in the center of the cochlea. The pressure difference across the micro-structure of the OoC produces a vibration that ultimately gives rise to the sensation of sound. Figure 1.1(a) illustrates an schematic of the OoC cross section including structural components such as basilar membrane (BM), tectorial membrane (TM) and hair bundles (HBs). A schematic of our OoC model is demonstrated in Fig. 1.1(b). The kinematics of the OoC model are introduced in the Appendix A, where the BM transverse motion is related to the TM motion in the traverse and radial directions and to the HB rotations.

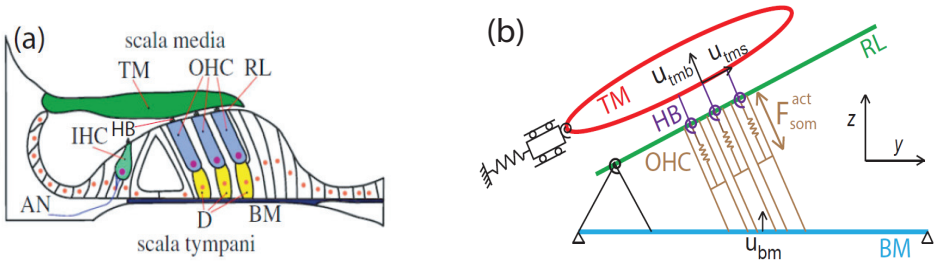

Figure 1.1: (a) A schematic transverse section of the organ of Corti. TM, tectorial membrane; OHC, outer hair cell; RL, reticular lamina; BM, basilar membrane; D, Deiters cell; AN, auditory nerve fibre; HB, hair bundle; and IHC, inner hair cell (image from [6]) (b) Micromechanical model for the organ of Corti structures (x-axis into the page).

1.1 Cochlear Active Process

The OoC displacements are boosted by a distinct nonlinear amplification mechanism that enables sound processing over a broad range of frequencies and intensities. This is reflective of the electromechanical response of the outer hair cell (OHC) which are responsible for mediating the active process necessary for normal hearing. The cochlear active process was first predicted by Gold [7]. Experiments by Johnstone and Boyle [8] and Rhode [9] revealed active mechanical responses in living animals. More evidence of the cochlear activity was later presented by Kemp [10] through the discovery of the *otoacoustic emission*; physiologically vulnerable sound emission elicited from a healthy ear after short stimulus.

Two mechanisms are hypothesized to power the cochlear active process: the HB motility [11–13] and prestin-based OHC somatic electromotility [14–18]. Although *in vitro* experiments have shown that both mechanisms are capable of amplification, the primary source of the nonlinear activity within the complex microstructure of the OoC remains much debated. The active HB motion has been shown to produce all hallmarks of the active process in non-mammals [11], while hair cells in these species do not possess somatic motility [19]. Hence, the active HB motions are likely responsible for mechanical amplification of low-amplitude signals in non-mammals. However, contribution of this mechanism in mammals remains debated [20]. Furthermore, efficiency of the HB motility at high frequencies is questioned, as the highest frequency reported for spontaneous bundle motion is no more than 100 Hz [21]. The principal argument against somatic motility as the amplifier is that the periodic component of the receptor potential will be attenuated by the membrane time constant, hence, this mechanism is not as effective at high frequencies [22]. This issue, however, is explained by the voltage-dependent K^+ conductance which is activated by the depolarized resting potential [23].

The cochlear active processes stem from electromoechanical properties of the

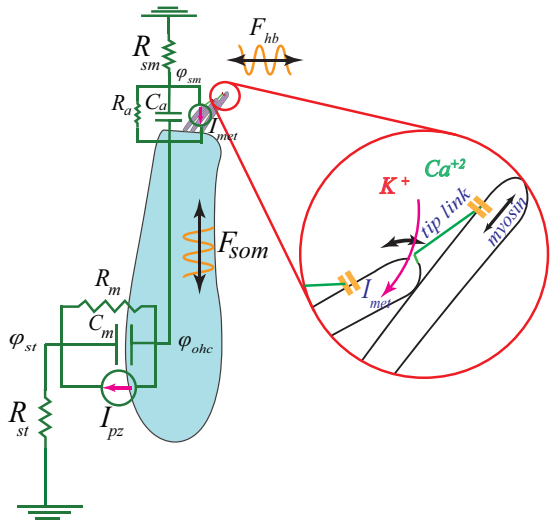

Figure 1.2: Schematic of an OHC and the MET apparatus. Deflection of the HB stereocilia (u_{hb}) relative to the RL gives rise to opening of the MET channels, resulting in the transduction current (I_{met}) flow into the cell. Change in the OHC basolateral membrane potential induces a change in the cells length, due to the OHCs piezoelectric properties [24], and generates the somatic force F_{ohc} along the cell. The zoomed-up inset figure illustrates the HB active mechanism based on the adaption process which produces an active force on the HB (F_{hb}). The two depicted stereocilia are connected by a tip link attached to a transduction channel on the apical part of the shorter stereocilia and the adaptation motor on the taller stereocilia. A circuit model is introduced to describe the current path in the cochlear cross section through the electrical resistances (R) and capacitances (C) of the apical (subscripts a) and basolateral (subscripts m) components of the OHC as well as the SM (sm subscripts) and ST (st subscripts) ducts.

OHCs. A schematic of the OHC along with an electrical circuit showing the current path across the cell are illustrated in Fig. 1.2. The two active processes are implemented in a comprehensive three-dimensional model of the cochlea and their relative contribution on the responses are investigated.

1.1.1 OHC Somatic Electromotility

Since the discovery of OHC somatic electromotility [24] these cells have been the focus of investigation as a mediator of electrical-structural interaction and of amplification. When the cochlea is stimulated with sound of a particular frequency, the pressure gradient across the OoC sets this elastic microstructure into oscillation. The TM

shearing movement deflects the HB (see Fig. 1.1) and causes the opening of the mechanoelectric transducer (MET) channel resulting in a transduction current (I_{met}) to flow into the OHC. The HB transduction current varies nonlinearly with the HB motions and saturates at large deflections. This process is widely accepted as the main source of the cochlear nonlinearity. A first-order Boltzmann function of the HB deflection (u_{hb}) can estimate the MET current flow into the OHC as [25]:

$$I_{met} = \mu \Delta V^0 G^{max} P, \tag{1.1}$$

where G^{max} is the maximum saturating conductance of the HB and μ is the MET scaling factor that controls the nonlinear sensitivity of the channels; $\mu = 0$ represents the passive model. Moreover, ΔV^0 is the resting value of the potential difference between scala media and intracellular OHC potential. The MET channel mechanics is linked to the HB motility through the adaptation mechanism dependency on the open probability of the channels P modeled by a two state Boltzmann function [26]

$$P_{hb}(u_{hb}, x_a) = \frac{1}{\left[1 + exp(\frac{-u_{hb}+x_a}{\Delta X})\right]} \tag{1.2}$$

where $\Delta X = \frac{k_B T}{f_{gs}\gamma}$ is a constant displacement that depends on the single channel gating force (f_{gs}), the Boltzman constant k_B and temperature T. The motion of the adaptation motor x_a is coupled to the HB deflection u_{hb} and oscillates along the stereocilia bundles (see Fig. 1.2). Figure 1.3 demonstrates the HB transduction current (Eq. 1.1) as a function of the bundle deflection (Eq. 1.1) for various values of the MET scaling factor μ. The horizontal dashed lines denote the DC currents for each simulation (differentiated by colors). The sensitivity of the MET channels are controlled by the parameter μ as evidenced in the curves slopes.

In response to changes in the OHC membrane potential, prestin (a protein present

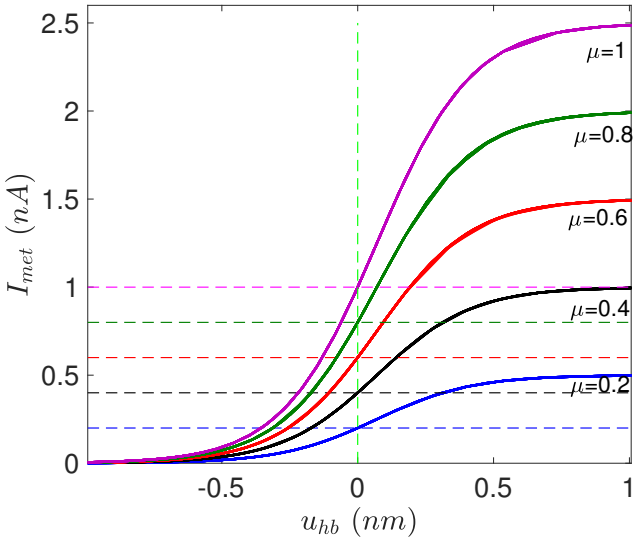

Figure 1.3: The MET transduction current (I_{met}) dependence on the HB deflection relative to the reticular lamina (RL) for a range of MET scaling factors (μ in Eq. 1.1). The dashed lines denote DC currents for resting probability of $P_0 = 0.4$. Values for the parameters introduced in the Eq. 1.1 are $f_{gs} = 23$ pN, $\Delta X = 0.17$ nm, $x_a = X_0 = 0.07nm$, $G_{max} = 5.1 \times 10^{-7}$ S/cm, $\Delta V^0 = 140mV$.

in the OHC) alters its conformation and, consequently, the length of the cell itself [24]. The OHC active force and current are related using the linearized piezoelectric relations:

$$\begin{aligned} F_{ohc} &= K_{ohc} u_{ohc}^{comp} + \varepsilon_3(\phi_{ohc} - \phi_{st}) \\ I_{ohc} &= (\phi_{ohc} - \phi_{st})/Z_m - \varepsilon_3 \frac{du_{ohc}^{comp}}{dt} \,. \end{aligned} \tag{1.3}$$

where $Z_m = R_m/(1-j\omega R_m C_m)$ is the OHC basolateral impedance, ε_3 is the piezoelectric coupling coefficient and K_{ohc} represents the OHC stiffness [27]. The piezoelectric current $I_{pz} = -\varepsilon_3 \frac{du_{ohc}^{comp}}{dt}$ represents a current source generated from the OHC elongation/compression. These set of equations relate the OHC compression u_{ohc}^{comp} (a linear function of the BM and TM displacements as described in the Appendix A) and the transmembrane potential (difference between the intracellular (ϕ_{ohc}) and extracellular

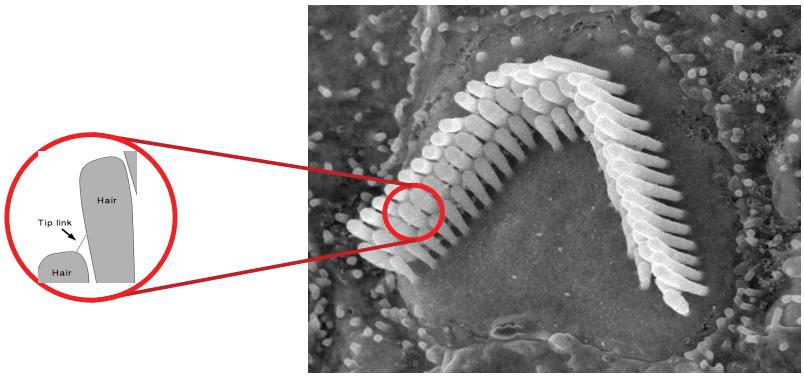

Figure 1.4: Architecture of a HB of human cochlea. The three rows of the OHC-HB stereocilias are connected with tip links and form a V-shape pattern. The scanning electron microscopy image is retrieved from www.medheadarts.wordpress.com

(ϕ_{st}) voltages) to the OHC active force (F_{ohc}) and current (I_{ohc}).

1.1.2 Active HB Motility

Martin and Hudspeth [28], introduced the HB active force as a possible alternative for OHC electromotility which is only available in mammalian cochlea but lacking in nonmammals. They reported physiological evidence that HB can be the source of amplification while still leaving room for other options. A schematic of the HB motility apparatus is shown in the inset subplot of Fig. 1.2. Deflection of the stereocilia bundles relative to the RL opens the transduction channel, allowing K^+ and Ca^{2+} to enter and depolarize the cell. The Ca^{2+} that enters into the cell causes to re-close the channel through the slow (myosin motors) and fast adaptations processes [26]. This process generates a cycle-by-cycle reactive force on th HB (F_{hb}). Different models have been proposed to describe the dynamics of the HB motility. In this study we use a simple two-state model of the active HB motility proposed by Tinevez *et.al.* [1]. This model is based on the gating-spring theory of the mechano-transduction channels [29] that describes the coupled dynamics of the hair bundle and adaptation motor motions.

The stereocilia are assumed to be attached to an adaptation motor through a tip

link [1] as shown in the schematic in Fig. 1.4. Equation 1.4 represents the dynamics interplay between the hair bundle motion (u_{hb}) and the adaptation motor (x_a) [1]:

$$\begin{aligned} \lambda \frac{du_{hb}}{dt} &= -k_{GS}(u_{hb} - x_a - DP) - k_{sp}u_{hb} + F_{ext} \\ \lambda_a \frac{dx_a}{dt} &= k_{GS}(u_{hb} - x_a - DP) - k_{es}x_a - \gamma f_{max}(1 - SP) \end{aligned} \tag{1.4}$$

where, k_{sp} and k_{es} are stiffness of stereocilia pivot and extension spring, respectively, and $k_{GS} = Nk_{gs}\gamma^2$ is apparent combined stiffness of gating springs (k_{gs}) for N number of transduction elements. $D = d/\gamma$, where d is the gating distance and γ is the geometrical gain constant. γ relates the sliding motion of the stereocilia against each other to the motion in the u_{hb} direction. f_{max} is the motor feedback actuation of the adaptation motor and S is the linear approximation of the calcium feedback strength. F_{ext} is the external force applied to the HB from the OoC mechanics (*in vivo*) or a stimulation probe (*in vitro*). In this equation, P represents open probability of the MET channels that can be approximated as a function of the HB and the adaption motor motions (Eq. 1.2). The resting open probability of the channels is fixed ($P_0 = 0.4$ [23]) by applying an intrinsic force on the HB. An internal degree of freedom x_a representing the adaptation motor, modulates the open channel probability (Eq. 1.2).

In this model an active regenerative force is produced through a hysteresis mechanism that adds energy to the system. This mechanism stems form the force-displacement characteristic of the HBs. As shown in Fig. 1.5(a), the HB force varies nonlinearly with the HB motion when the adaptation mechanism is implemented. This leads to a negative effective stiffness for the HBs around the equilibrium (illustrated by asterisk marker insider the figure) which in turn generates spontaneous oscillations (Fig. 1.5(b)) through an Hopf bifurcation mechanism. The parameter values of the HB model used in this study are listed in the Table 5.4.

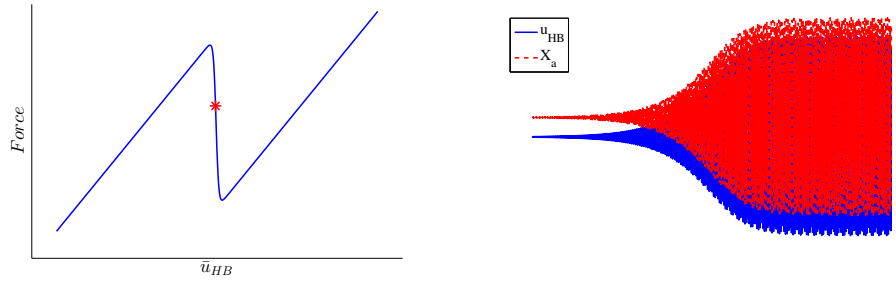

(a) (b)

Figure 1.5: HB adaptation mechanism for an isolated HB. (a) Nonlinear force-displacement relation of a HB; the equilibrium (denoted with an asterisk marker) is located in the unstable region. (b) Spontaneous oscillation of the positions of the HB u_{hb} and the adaptation motor x_a.

1.1.3 The 3-Dimensional Model

A physiologically-based model of the cochlea is developed and the active processes are implemented. In this model electrical and mechanical elements of the OoC are coupled explicitly through kinematic constraints and forces (see [27]). Figure 1.1 depicts a schematic of the OoC and transverse section of the model. The OoC structure is loaded by the fluid pressure difference across the BM. The fluid is assumed inviscid except in the subtectorial space and viscosity is incorporated through damping of the OoC and the BM. The BM is assumed to be a flexural plate pinned at both ends, with a single degree of freedom (u_{bm}) corresponding to the first symmetric mode of vibration. The TM is modeled as a rigid rod attached to the limbal edge, with an elastic spring resisting motion in the radial direction (u_{tms}), and a rotational spring in the transverse direction (u_{tmb}). The transverse motion of the BM is mediated to the radial and transverse motion of the TM through the HBs.The relative shear between the TM and the RL deflects the HBs creating tension in the tip links and opening the MET channels. The kinematics relations between the OoC components are formulated in the Table A.1.

The mathematical modeling, gives rise to a set of coupled PDEs which are ap-

proximated using the finite element method (FEM). The coupled mechanical-fluidic-electrical equations can be represented in the matrix form as

$$\begin{bmatrix} K_f & Q_{fs} & 0 \\ Q_{sf} & K_s & Q_{se} \\ 0 & Q_{es} & K_e \end{bmatrix} \begin{bmatrix} \mathbf{P} \\ \mathbf{U} \\ \mathbf{\Phi} \end{bmatrix} = \begin{bmatrix} f_p \\ 0 \\ 0 \end{bmatrix} \tag{1.5}$$

In this equation $\mathbf{U}$ is the displacement nodal vector of the OoC structural components; including u_{bm},u_{tms} and u_{tmb} for each cross section. Similarly, $\mathbf{\Phi}$ is the voltage nodal vector which encompasses ϕ_{sv}, ϕ_{sm}, ϕ_{ohc} and ϕ_{st} for each cross section. Moreover, $\mathbf{P}$ vector represents nodal fluid pressure in the scala vestibuli (SV) and scala tympani (ST). These vectors represent the finite element approximation of the cochlear structural-electrical-acoustical responses calculated by solving the linear matrix of Eq. 1.5. Structural, electrical and fluid components are denoted by subscripts s , e and f, respectively, while Q represents coupling between the domains. On the right-hand side of this equation, f_p represents the stimulation effect on the boundary conditions.

CHAPTER II

Nonlinear Dynamics of the Cochlear Activity

2.1 Introduction

Cochlear responses are shown to be nonlinear and tuned such that lower sounds receive higher gains relative to higher sound pressure level (SPL). This property is called the cochlear amplifier which enables mammalian auditory system to work over a broad range input sounds. Recently, there has been growing interest in exploring the relative contribution of the two candidates active mechanisms (OHC and HB motility) on the cochlear amplifier [3, 30–33]. It is shown that the two candidate active mechanisms are linked through the MET channels; hence, conducting experiments to perturb one mechanism without effecting the other remains elusive [3, 30–32, 34]. The other approach is to incorporate the active mechanisms into a cochlear model and explore their relative contribution on the cochlear dynamics.

The models aim to be as simple as possible while being able to predict cochlear behaviors correctly. Duifhuis *et al.* [35] developed a network model using a Van der Pol oscillator. This model is based on the idea that sensitivity to low level sounds is due to reduction of low level damping and that cubic distortion products dominates emissions. They argue that spontaneous emissions would arise at points where this reduction is too strong. This model is not physiologically based, however, is able to introduce a possible mechanism for amplification.

The Hopf bifurcation normal form has been introduced [36] as a possible principal mechanism of the cochlear nonlinear amplification. This model predicts a compressive nonlinearity when tuned near the stability boundary. Mechanical responses to acoustic stimuli in this model are close to a cubic form, as observed from the experimental data [6]. Magnasco [37] used Hopf bifurcation to explain the shape of the cochlea tuning curves by analyzing energy flow and dissipation. Kim *et al.* [38] proposed a model including both damping and stiffness nonlinearity. They reported the stiffness nonlinearity, modeled with Duffing equation, increases frequency selectivity at high levels. Ó Maoiléidigh and Jülicher [2] proposed a model considering somatic motility, transduction current adaptation nonlinearity and showed it is consistent with the experimental results by Kennedy *et al.* [22]. They incorporated myosin motor dynamics in their model of OHC which also included electrical domain through charge dynamics. Later Szalai *et al.* [39] simplified Maoiléidighh's model and studied two different bifurcations that may be the source of amplification. They argued that it is not necessary for local model of the OHC dynamics to take form of Hopf oscillator and there is possibility of other type of local bifurcation including saddle-node and cusp.

Although the Hopf model represents the hallmarks of a healthy cochlea (*e.g.* compressive amplification, frequency selectivity, sensitivity and otoacoustic emissions), there are some limitations associated to this model. For instance, the ability of this model to amplify relies on the dynamics being poised on the edge of an oscillatory instability characterized by a Hopf bifurcation [40, 41]. Moreover, this model is limited to low SPL responses hence does predict the cochlear saturation feature that linearizes the response at hight SPLs.

Tinevez *et al.,* [1] introduced a two-state model of the HB dynamics that includes the adaptation process. In this model a cycle by cycle mechanism provides power amplification and gives rise to a regenerative spontaneous oscillation (so called limit

cycle). This model works near the Hopf stability boundary of the dynamics, generating a cubic compressive nonlinearity. Ó Maoiléidigh and Julicher [2] incorporated this model into an integrated system of the OoC that couples the hair bundle motility and electromotility processes. Although, the model provides good qualitative predictions, a truly physiological mechanism remains absent.

The Hopf bifurcation model is proposed as the principal mechanism for the HB activity giving rise to the cochlear amplifier [1, 39, 41]. However, the Hopf bifurcation mechanism is not limited to the HB adaptation process. This mechanism stems from the MET saturating nonlinearity which plays a central role in both active processes: HB motility [42] and OHC somatic motility [43]. In this study, we incorporate both the OHC somatic motility as well as the HB active process in a nonlinear cross-sectional model of the cochlea to study possible interplay between the active mechanisms in an integrated system. This study has been performed in collaboration with PhD student, Aritra Sasmal.

2.2 Cochlear Cross-Section Model

Detail of our cochlear model are introduced in Chapter I and in the Appendix A. Eq. A.14 describes the linearized electromechanical cross section model. In order to explore the cochlear amplifier in this model, a harmonic force $P\sin(\Omega\, t)$ arising from fluid loading is applied on the BM. Parameters used for this study are listed in the Table 2.1.

2.3 Compressive Nonlinearity

Figure 2.1(a) depicts the nonlinear level dependence of the BM response. The simulations correspond to 1 percent off from the Hopf point (controlled by μ in Eq. 1.1) while the stimulation frequency (Ω) is the CF of the measured location. The com-

Table 2.1: Cross section model parameters. x is the distance from the stapes (cm). The diameter size of an OHC ($D_x = 10\mu m$) is used to lump the parameters for the cross section model.

Property	Description	Value
b	BM width	$0.008 + (0.018 - 0.008)x/1.85$ cm
h_{bm}	BM thickness	$0.0007 + (0.00017 - 0.0007)x/1.85$ cm
K_{bm}	BM stiffness per unit length	$1.732 \times 10^6 exp(-4x)(1 + (x/1.85)^3)D_x\ dyn/cm^2$
K_{tms}	TM shear stiffness	$1.65 \times 10^5 exp(-4x)D_x\ dyn/cm$
K_{tmb}	TM bending stiffness	$0.27 \times 10^5 exp(-4x)D_x\ dyn/cm$
K_{rl}	RL stiffness	$6 \times 10^4 exp(-4x)D_x\ dyn/cm$
K_{ohc}	OHC stiffness	$6 \times 10^4 exp(-4x)D_x\ dyn/cm$
K_{st}	Stereocilia stiffness	$0.6 \times 10^5 exp(-4x)D_x\ dyn/cm$
M_{bm}	BM mass per unit length	$2.8 \times 10^{-6} D_x\ gr/cm$
M_{tms}	TM shear mass	$6 \times 10^{-6} exp(1.6x)D_x\ gr$
M_{tmb}	TM bending mass	$4.5 \times 10^{-6} exp(1.6x)D_x\ gr$
c_{bm}	BM damping coefficient	$0.5D_x\ dyns/cm$
c_{tms}	TM shear damping coefficient	$0.3D_x\ dyns/cm$
c_{tmb}	TM bending damping coefficient	$0.3D_x\ dyns/cm$
$G^{max}\Delta V^0$	saturating HB conductance	$3 \times 10^{-4} exp(-4x)(1 + 2(x/1.85)^3 + 3(x/1.85)^4 + 3.5(x/1.85)^5)(150 - 10x)D_x$
ε_3	electromechanical coupling coefficient	$(-(0.008 - (0.008 - 0.01)x/1.85)1.3)D_x\ dyn/mV$

pressive nonlinearity (1/3 power-law slope) for a medium range of stimulations and linearity for the lower and higher levels are in good agreement with the experimental data [44]. The Hopf normal form model cannot predict the linear region for high SPLs [6]. Although, our model is proved mathematically to present the local Hopf bifurcation feature (see Appendix B and [45]), it does not exhibit the shortcoming of the Hopf model for high intensity stimulations. As shown in subplots of Fig. 2.1(a), the HB transduction saturation explains the linearity of the model at high level stimulations. Small plots inside Fig. 2.1a demonstrate the HB current transduction for three different stimulation levels. We can see that HB current transduction nonlinearity gives rise to the BM nonlinear response for medium stimulation levels. These results are consistent with [6] that a physiological coupling between BM and HB through TM, can exhibit the compressive nonlinear amplification even without active HB motility.

It is found that two conditions are essential for presence of compressive nonlinearity in our model and generally in any model which is based on Hopf normal form. First, parameters should be tuned to be close enough to the Hopf point and, second, stimulation frequency should be close to the resonance frequency of the system (called

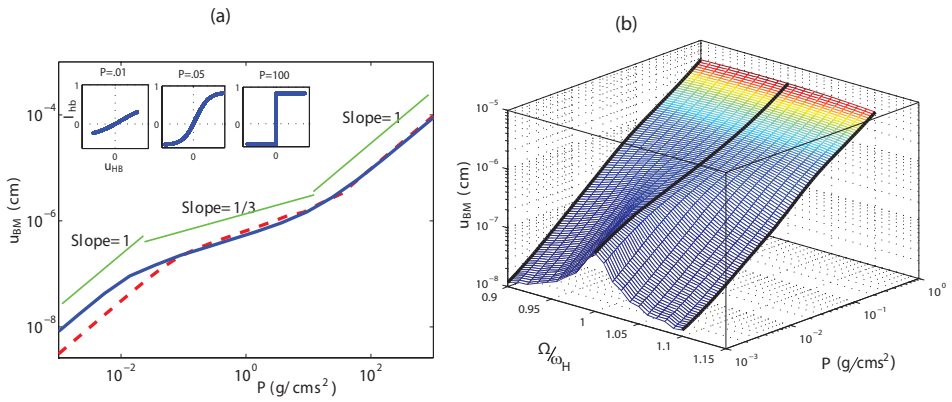

(a) (b)

Figure 2.1: (a) BM nonlinear response to the input fluid loading for parameters close to the Hopf point (log-log scale); solid line: cross section model, dashed line: 3-dimensional global model, thin lines demonstrate the slope for different zones. The three subplots illustrate the HB current transduction versus displacement fo different force loadings (noted on top). (b) The BM displacement versus stimulation amplitude and frequency. The frequency axis is scaled with respect to the imaginary part of the largest eigenvalue at the Hopf point (ω_H). The model is nonlinear for frequency stimulations near the ω_H and linear away from that. The OHC somatic electromotility is the sole mediator of the active process in this simulation.

characteristic frequency in the global cochlea). Possible physiological mechanisms for the first condition in the full cochlea is still under debate, while the second condition is known as the cochlear frequency selectivity. The frequency effect is shown in Fig. 2.1(b) where a 3-D surface plot of the BM displacements with respect to the input force and frequency are presented. The stimulation frequencies are normalized with respect to the CF of the location and it is shown that the compressive nonlinearity only exists near the CF frequency.

2.4 Stability Analysis of the OHC Somatic Based Model

In this section, stability of the OoC cross section model, when the OHC somatic motility is the mediator of the active process and in the absence of HB adaptation, is studied. The MET channels nonlinearity (Eq. 1.1) is linearized (as shown in Eq. A.14) and stability of the OoC dynamics is explored. Figure 2.2 depicts the stability bound-

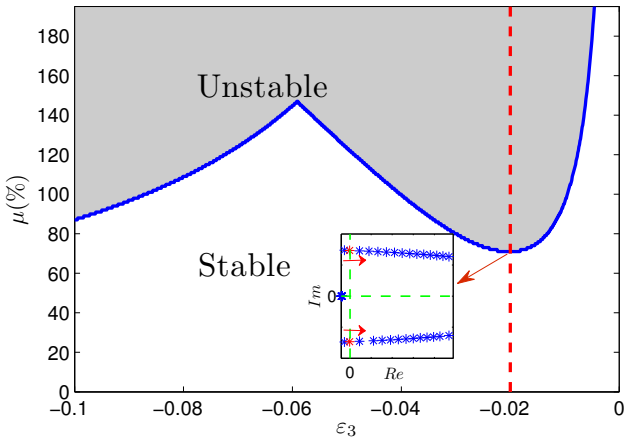

Figure 2.2: Stability chart for the cochlea cross section model with OHC electromotility. The blue line denotes the stability boundary where a complex conjugate paired eigenvalues pass the imaginary axis by increasing MET scaling factor (μ) as shown in the inset plot.

ary in the plane of the MET scaling factor (μ) and the electromechanical coupling coefficient (ε_3 as introduced in Eq. 1.3). It is illustrated that by increasing the MET sensitivity (controlled by μ as introduced in Eq. 1.1) a conjugate paired eigenvalues passes the imaginary axes and causes instability by injecting more energy into the OoC. The values of μ are presented in percentage which indicate the activity level; for instance μ=0 refers to the passive model. We note that for the passive case ($\mu = 0$), the system is stable independent from the ε_3. Moreover, when ε_3=0 (uncoupling between electrical and mechanical domains) the system is stable independent from MET sensitivity. Hence, the passive OoC dynamics is stable.

2.5 Bifurcation Analysis; Nonlinear System

Next, a numerical bifurcation analysis of the fully nonlinear model is performed using a numerical continuation technique [46]. Moreover, the center manifold reduction technique is also utilized for analytical study of the model (see Appendix B). Figure 2.3 shows the bifurcation diagram when μ is considered as the bifurcation parameter. This figure demonstrates generation of a periodic solution, called limit cycle,

through a supercritical Hopf bifurcation. Figure 2.3 illustrates the spontaneous oscillation amplitudes of the BM displacements with respect to the bifurcation parameter μ. As the MET sensitivity is increased beyond μ_{Hopf} (shown in Fig.2.3 with a square marker), the static equilibrium (shown in red dashed lines) becomes unstable and the system undergoes periodic oscillation through a supercritical Hopf bifurcation. Increasing the MET channel sensitivity, pumps more energy into the system through the HB transduction current. At a certain value for MET sensitivity (Hopf point) this energy balances with the damped energy of the system and develops a limit cycle. The BM time response and phase portrait for two cases, before and after bifurcation point, are plotted in Fig. 2.4. Although, the limit cycle oscillation of the system is interesting and has been studied in some detail [45], we shall constrain ourselves to the stable regime below μ_{Hopf} , where an external force acting on the BM can amplify the mechanical motion of the OoC through a feedback loop involving somatic force generation by the OHCs.

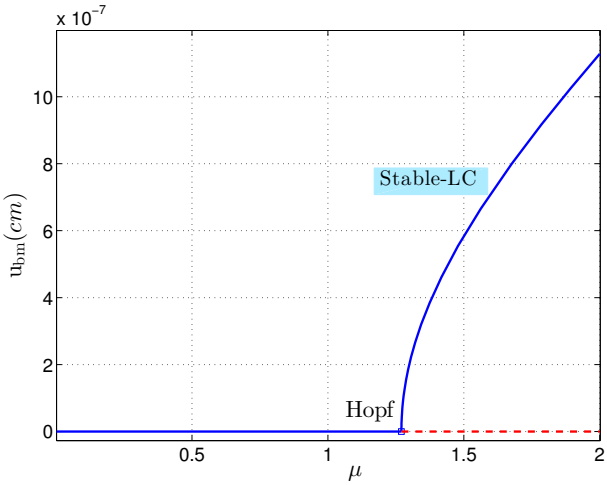

Figure 2.3: Static and dynamic equilibrium of the BM with μ. Red dashed lines show the static equilibrium of the BM as the MET sensitivity scaling factor μ is increased. The MET resting probability is held constant at $P_0 = 0.4$. The static equilibrium is stable for low μ and is unstable beyond a critical value for μ shown with the black arrow. Beyond the Hopf point, the system transitions into limit cycle oscillations through a supercritical Hopf bifurcation. Bifurcation diagram for ε_3=-0.04; LC: limit cycle, solid line: stable; dashed line: unstable

Property	Description	Value
$k_{GS}(mN/m)$	gating spring stiffness	0.95
$k_{es}(mN/m)$	extension spring stiffness	4
$f_{max}(pN)$	motor strength	100
γ	Geometric gain	$0.25 - \left[\frac{x_{gauss}}{1.85}(0.25 - 0.11)\right]$
$d(nm)$	Gating distance	8.7
$\lambda(\mu Ns/m)$	Effective stereocilia damping	0.28
$\lambda_a(\mu Ns/m)$	Adaptation motor damping	1

Table 2.2: Parameters used for the HB active model.

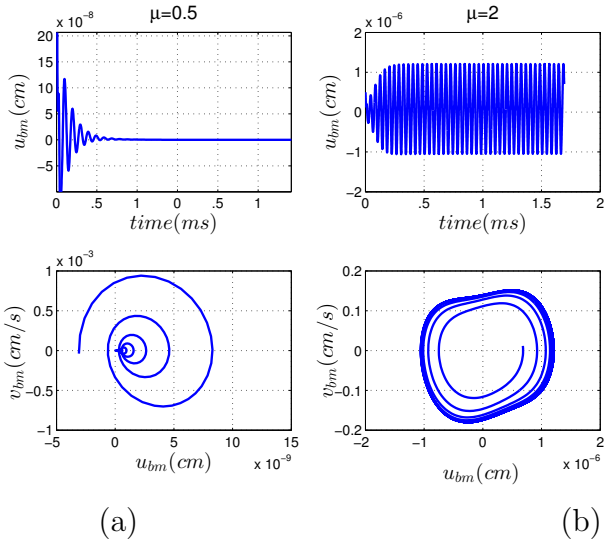

(a) (b)

Figure 2.4: Time response and phase portrait for ε_3=-0.04 and MET coefficient factor below the Hopf point (left panel; μ=0.5) and above the Hopf point (right panel; μ=2).

2.6 Nonlinear Dynamics of the Isolated HB

An active HB model proposed by Tinevez *et al.,* [1] is utilized to simulate the HB adaptation process. This model represents coupling between the hair bundle motion (u_{hb}) and the adaptation motor (x_a) as described in the Chapter I (see Eq. 1.4). Different regimes of HB adaptation operation for an isolated HB, with the adaptation motor controlling the resting tension on the tip links, are explored. First, the fundamental characteristics of the HB activity is studies by linearizing the nonlinear dynamic of the HB adaptation about equilibrium (Eq. 1.4):

$$\begin{pmatrix} \dot{u_{hb}} \\ \dot{x_a} \end{pmatrix} = \begin{bmatrix} \frac{-(\bar{k}_{gs}+k_{sp})}{\lambda} & \frac{\bar{k_{gs}}}{\lambda} \\ \frac{(\bar{k}_{gs}+\bar{k}_f)}{\lambda_a} & \frac{-(\bar{k}_{gs}+k_{es}+\bar{k}_f)}{\lambda_a} \end{bmatrix} \begin{pmatrix} u_{hb} \\ x_a \end{pmatrix} + \begin{pmatrix} \frac{F_{ext}}{\lambda} \\ 0 \end{pmatrix}, \tag{2.1}$$

where, $\bar{\epsilon} = \frac{k_{GS}d^2}{k_BT}$, $\bar{k}_{gs} = k_{gs}(1-\bar{\epsilon})$ and $\bar{k}_f = \frac{\gamma f_{max} S\bar{\epsilon}}{D} = \alpha\bar{\epsilon}k_{gs}$. $\alpha = \frac{f_{max}S}{Nk_{GS}d}$ is a non-dimensional parameter which is the ratio of the feedback strength to the gating strength, and may change from base to apex if the calcium strength or the feedback changes. $\bar{\epsilon}$ is the sensitivity of the MET channel with respect to stereocilia displacement for a passive HB and is given by $\bar{\epsilon} = D\left.\frac{\partial P}{\partial u_{hb}}\right|_{P_0}$. The displacement of the adaptation motor can be written in terms of the HB displacement as

$$x_a = \left[\frac{k_{gs}}{\lambda_a\omega_p}\frac{1+(\alpha-1)\bar{\epsilon}}{\sqrt{1+(\omega/\omega_p)^2}}\angle(\omega/\omega_p)\right] u_{hb}, \tag{2.2}$$

where $\omega_p = \left(\frac{k_{es}+k_{gs}(1+(\alpha-1)\bar{\epsilon}}{\lambda_a}\right)$ is the corner frequency for the adaptation motor response. As the calcium feedback α increases, the ω_p increases, reducing the adaptation motor's response time.

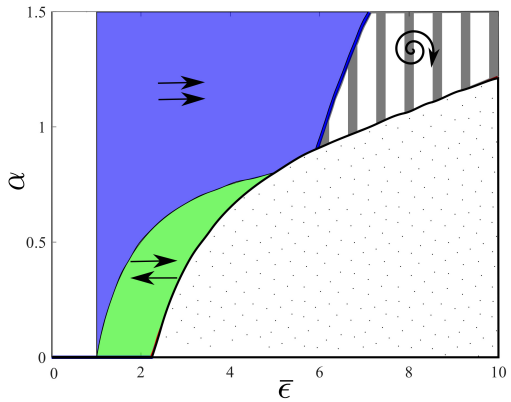

Figure 2.5: Isolated active HB dynamics. Classification of different dynamics of the isolated active HB in $\alpha - \bar{\epsilon}$ space for $P = 0.4$. For $\bar{\epsilon} < 1$, the active mechanism does not generate energy. The region with vertical bars correspond to a region of limit cycles and the dotted region is bistable. The blue region corresponds to parameters for phasic adaptation whereas in the green region the HB adaptation is anti-phasic.

Fig. 2.5 shows the different regimes of HB dynamics in the $\alpha - \bar{\epsilon}$ space. Below $\bar{\epsilon} = 1$, the adaptation mechanism does not generate any energy. The dotted region corresponds to a region of bistability, where the static equilibrium at $P = 0.4$ is unstable and the steady state open probability of the MET channels is close to 0 or 1. The region marked with vertical bars in Fig. 2.5 is a region where the hair bundle undergoes spontaneous oscillation and is bounded by a supercritical Hopf boundary at the top edge and a subcritical Hopf boundary at the bottom edge. For parameters assumed in this study, the frequency of limit cycle oscillation of the isolated hair bundles was found to be less than 1.5 kHz.

The region shown in blue corresponds to a region of phasic adaptation. In this region, the adaptation motor is in phase with the HB displacement at low frequencies, and leads the HB by a quarter cycle at high frequencies. The green region corresponds to anti-phasic adaptation, where the adaptation motor lags the hair bundle by a half cycle at low frequencies and a quarter cycle at high frequencies. The force on the hair bundle by the adaptation motor is out of phase with the hair bundle velocity (dissipative).

Although adaptation generates energy at low frequencies ($\omega << \omega_p$), it is accompanied by a loss of low frequency MET sensitivity due to the in-phase motion of the adaptation motor reducing the tension on the tip-links and consequently decreasing the MET sensitivity. This leads to reduced current flow through the MET channels in the hair bundles which will be further investigated in the next section. The reduction in sensitivity of the MET channels to HB motion is given by

$$\frac{d(P^{x_a} - P)}{du_{hb}} = -\frac{\bar{\epsilon}}{D}\left[\frac{1 - \frac{k_{es}}{\omega_p \lambda_a}}{1 - j\frac{\omega}{\omega_p}}\right]. \tag{2.3}$$

where P^{x_a} is the open probability of the MET channels when the adaption process is included. The interplay between power generation of the HB motility and the

sensitivity of the MET channels (which controls the somatic power generation) is further explored in the next section.

2.7 Interplay Between OHC Somatic Electromotility and HB Motility

In this section we study contribute of the two active processes (HB motility and OHC somatic electromotility) on the cochlear nonlinear amplifier. Modeling of the two active mechanisms are introduced in Chapter I. First, we identify the phasic and anti-phasic regimes for the adaptation process in the plane of the key parameters of the HB and OHC active processes (S and μ, respectively). The parameter S controls the feedback strength (Eq. 2.6) while μ is the scaling factor of the MET channel sensitivity (Eq. 1.1). Fig. 2.6 shows the stability boundary of the system at an apical location ($x = 1.2$ cm from stapes) in the $S - \mu$ space. The dynamics retain flavors of both isolated HB adaptation as well as somatic motility. The calcium feedback parameter, S, divides the space into phasic and anti-phasic HB adaptation and the MET sensitivity factor, μ, modulates the stability of the system. We choose two operating points in the stable regime of the $S - \mu$ space (near the stability boundary) corresponding to phasic adaptation and anti-phasic adaptation, to study the contribution of these mechanisms to power generation and nonlinear compression. In this study, we shall denote the phasic adaptation parameters ($S = 4, \mu = 5.5$) as $\mathcal{P}_1$, while the anti-phasic adaptation parameters ($S = 0.5, \mu = 4.7$) shall be denoted as $\mathcal{P}_2$. It is noted that the the stability boundary shifts slightly for different locations along the cochlea as shown in Fig. 2.6(b).

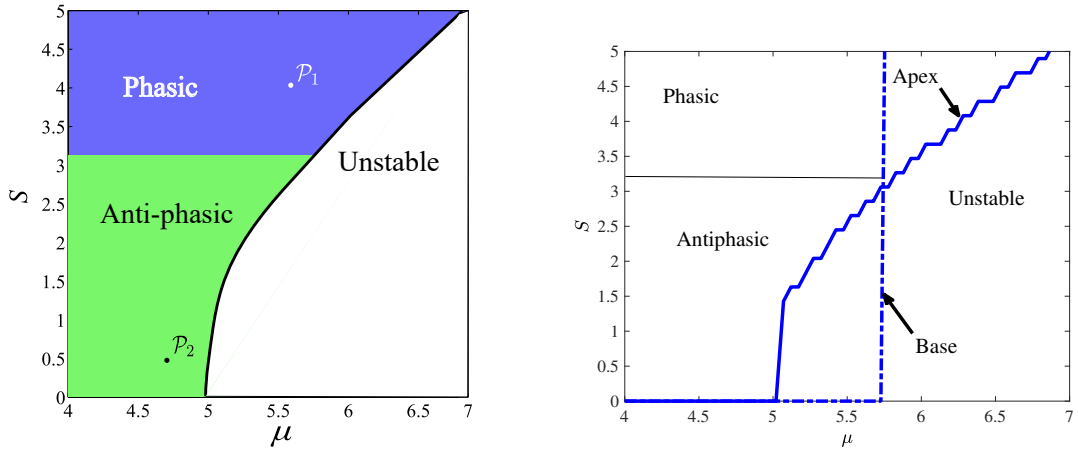

Figure 2.6: Dynamics of the coupled system in the $S-\mu$ space for an apical location ($x = 1.2$ cm from stapes). The dynamics of the coupled system retains flavors of both somatic motility and HB activity. The calcium feedback S primarily controls the phase of adaptation in the stable region. The MET sensitivity μ controls the stability of the system, with the system exhibiting limit cycle oscillations beyond a critical μ, which in the coupled system is calcium feedback (S) dependent. Two sets of parameters, corresponding to phasic adaptation ($\mathcal{P}_1$; $S = 4, \mu = 5.5$) and anti-phasic adaptation ($\mathcal{P}_2$; $S = 0.5, \mu = 4.7$), as discussed in the text are shown in this space. (b) Dynamics of the coupled system in the $S-\mu$ space for apical ($x = 1.2$ cm) and basal ($x = 0.4$ cm) locations along the cochlea.

To ascertain the variation of efficacy of these two adaptation mechanisms throughout the length of the cochlea, we define $\Omega(x)$ as

$$\Omega(x) = \frac{\max\{u_{bm}^{HB+OHC}\}}{\max\{u_{bm}^{OHC}\}}, \tag{2.4}$$

where $\max\{u_{bm}^{HB+OHC}\}$ is the peak BM frequency response of the OoC with both HB activity and OHC somatic motility, and $\max\{u_{bm}^{OHC}\}$ is the peak BM frequency response of the OoC with somatic motility only, at a distance x cm from the stapes.

Fig 2.7 shows the variation of $\Omega(x)$ from base to apex for $\mathcal{P}_1$ with blue line and $\mathcal{P}_2$ with red line. For the $\mathcal{P}_1$ parameters, while the HB activity adds energy into the system, the reduction in MET sensitivity and HB current at low frequencies lead to a

decrease in the somatic force generation (Eq. 1.3), decreasing the BM gain at the apex. For the $\mathcal{P}_2$ parameters, the anti-phasic hair bundle adaptation leads to an increase in HB current, and consequently somatic motility. However, this is significant only at low frequencies and is not effective beyond the corner frequency of the adaptation motor response ($\sim$ 1 kHz).

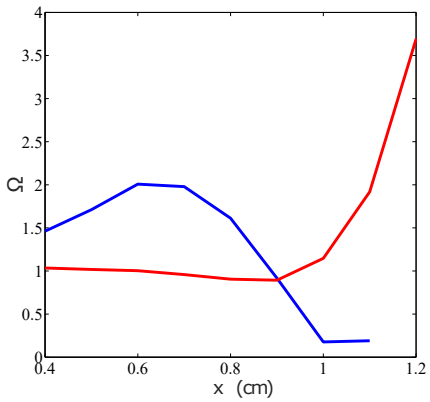

Figure 2.7: Variation of Ω with distance x from the stapes. Ω for phasic adaptation ($\mathcal{P}_1$) is shown with blue lines and that for anti-phasic adaptation ($\mathcal{P}_2$) is shown with red lines.

It is noted that the OHC and HB active processes can interact through the MET apparatus. Hence, the MET sensitivity is influenced by the HB motility. The MET sensitivity is calculated as:

$$Sen = \partial P/\partial u_{hb} = |C_p\,(1 - \partial x_a/\partial u_{hb})\,| \tag{2.5}$$

where $C_p = P_0(1 - P_0)/\Delta X$ is a function of the resting probability of the MET channels $P_0 = 0.4$ and the displacement constant ΔX introduced in Eq. 1.1. A time dependence of $e^{-j\omega t}$ is assumed (where ω is the angular frequency) and the las term of Eq. 2.5 is calculated from the HB dynamics (see Eq. 1.4) as:

$$\partial x_a/\partial u_{hb} = \frac{-k_{gs} + DC_p k_{gs} + \gamma f_{max}(1 - SC_p)}{-k_{gs} + DC_p k_{gs} - k_{es} - \gamma f_{max} SC_p + j\lambda_a \omega}, \tag{2.6}$$

The MET sensitivity of the active HB model is calculated from Eq. 2.5 while for the passive HB we set $\partial x_a/\partial u_{hb} = 0$. Figures 2.8 and 2.9 illustrate variations of the displacement gain (Ω) and MET sensitivity (ratio of Sen of the active to passive HB) with respect to μ and distance from stapes for two values of S=4 (panel a) and S=0.5 (panel b). Moreover, the stability boundary for the active and passive HB models are denoted with dashed and dot-dashed lines, respectively. It is noted that the S=4 gives rise to higher gain at basal locations (higher frequencies) while S=0.5 shows an opposite effect. As shown in Fig. 2.9 the change on gain is linked to the alteration of the MET sensitivity such that decreasing the sensitivity gives rise to lower gains. We also note that the HB motility when S=4 decreases the MET sensitivity for all locations (frequencies) while S=0.5 increases the sensitivity (sensitivity ratio greater than 1).

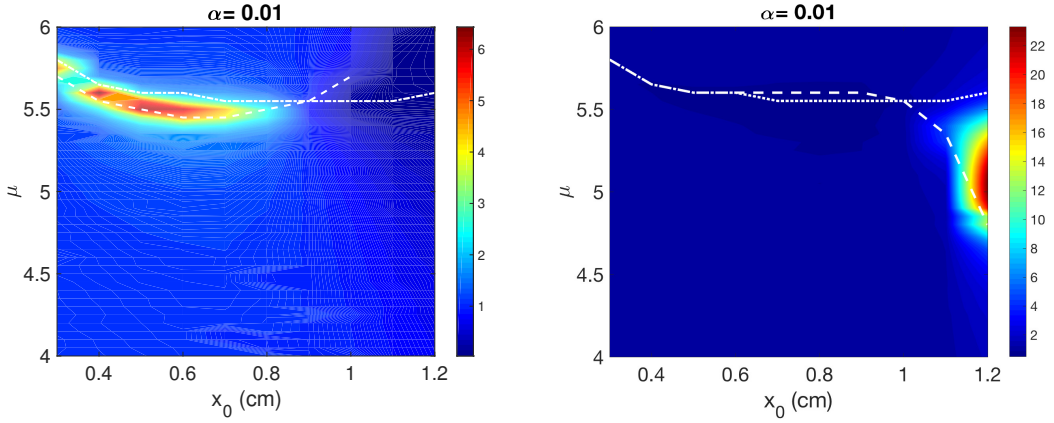

(a) (b)

Figure 2.8: Contour plot of the HB gain Ω in the plane of the activity levels (controlled by μ) and locations along the cochlea (x_0) for (a) S=4 (b) S=0.5. The stability boundary for the active and passive HB models are denoted with dashed and dot-dashed lines, respectively.

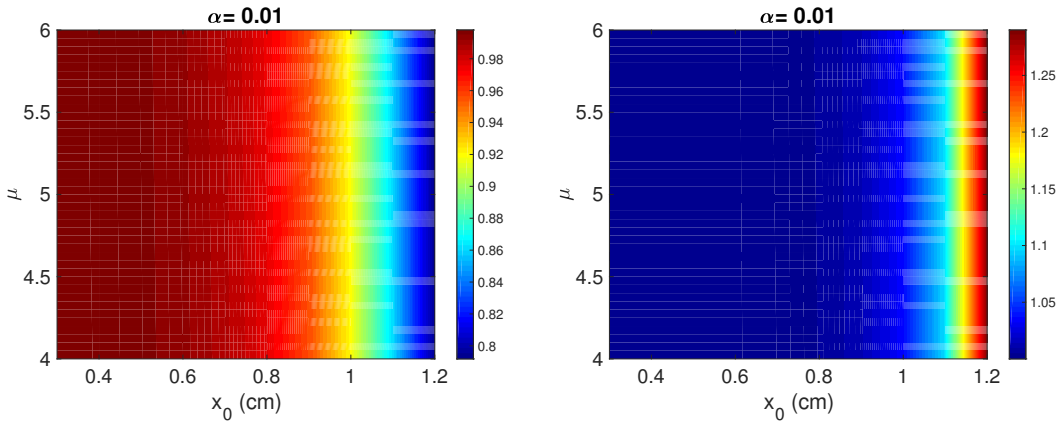

(a) (b)

Figure 2.9: Contour plot of the MET sensitivity ratio between active and passive HB simulations in the plane of the activity levels (controlled by μ) and locations (x_0) along the cochlea for (a) S=4 (b) S=0.5

2.7.1 Active Power

The work done per cycle by the HB activity and the OHC somatic motility normalized to the work done by the BM external force F_{bm}^{ext} is given by:

$$P_{hb}^{*} = \frac{\int_0^T -k_{gs}(u_{hb} - X_a - DP)\dot{u}_{hb}dt}{P_{ext}}, \tag{2.7}$$

$$P_{ohc}^{*} = \frac{\int_0^T -\varepsilon_3 \Delta\phi_{ohc}\dot{u}_{ohc}^{comp}dt}{P_{ext}}, \tag{2.8}$$

where $P_{ext} = \int_0^T -F_{bm}^{ext}\dot{u}_{bm}dt$ and T is the time period. In Eq. 2.8, the OHC active force $F_{ohc} = -\varepsilon_3\Delta\phi_{ohc}$ is multiplied by velocity of the OHC compression $\dot{u}_{ohc}^{comp}$ (defined in Appendix Table A.1) and integrated over time. A positive power gain represents power addition whereas a negative power gain represents power dissipation.

Fig. 2.10 shows the normalized power gain of the HB (P_{hb}^{*}) for varying levels of external stimulation on the BM (F_{bm}^{ext}). Blue curve shows the power gain for the OoC with both HB activity and OHC somatic motility and red curve shows the corresponding quantities for the OoC with somatic motility only. Since the two

adaptation mechanisms (phasic and anti-phasic adaptation) are effective at different locations along the cochlea, we study the power gain for parameters $\mathcal{P}_1$ at the base ($x = 0.4$ cm) and for parameters $\mathcal{P}_2$ at the apex ($x = 1.2$ cm). The HB power gain is zero for both $\mathcal{P}_1$ and $\mathcal{P}_2$ for the OoC without HB activity (red lines) by definition. For $\mathcal{P}_1$ (Fig. 2.10(a)), the phasic adaptation adds power into the system, and the power gain decreases monotonically as the stimulation amplitude is increased. On the other hand, the HB anti-phasic adaptation ($\mathcal{P}_2$) dissipates power (Fig. 2.10(b)).

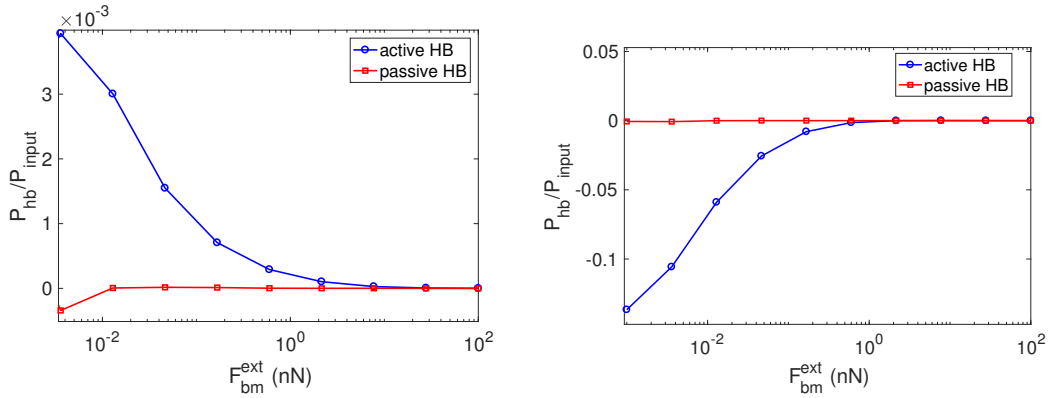

Figure 2.10: Power gain of HB activity for (a) $\mathcal{P}_1$ parameters at 0.4 cm from stapes and (b) $\mathcal{P}_2$ parameters at 1.2 cm from stapes. The blue curve shows the simulation with both active processes (HB and somatic motility) while the red curve shows the passive HB model (by setting the adaptation motor x_a to be stationary).

The normalized power gain by the OHC somatic motility for $\mathcal{P}_1$ and $\mathcal{P}_2$ are shown in Fig. 2.11(a) and Fig. 2.11(b), respectively. The power gain by the OHC somatic motility without HB adaptation is shown with red lines. When hair bundle adaptation is added to the system, the power gain by the somatic motility (blue lines) increases by around 4dB for $\mathcal{P}_1$ at the base and 10 dB for $\mathcal{P}_2$ at the apex. The dramatic increase in power gain at the apical region is due to the anti-phasic HB adaptation increasing the MET current and consequently the OHC somatic force (Eq. 1.3).

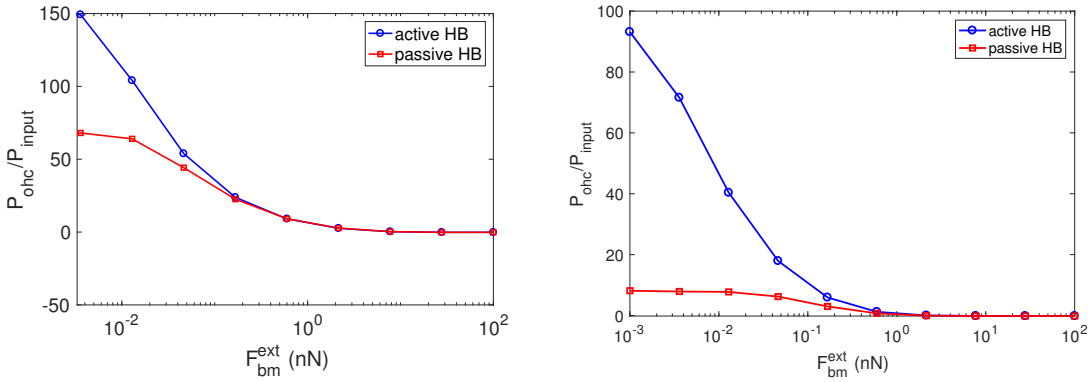

Figure 2.11: Power gain of OHC somatic motility for (a) $\mathcal{P}_1$ parameters at 0.4 cm from stapes and (b) $\mathcal{P}_2$ parameters at 1.2 cm from stapes. The blue curve shows the simulation with both active processes (HB and somatic motility) while the red curve shows the passive HB model (by setting the adaptation motor x_a to be stationary).

2.8 HB Motility Contribution on the Compressive Nonlinearity

Non-linear compression is a key signature of an active cochlea which enables it to operate over a dynamic range of stimuli encompassing many orders of amplitude. The primary cochlear nonlinearity is thought to be that due to the nonlinearity of the MET channels (Eq. 1.1). Fig. 2.12(a) and Fig. 2.12(b) shows the variation of peak BM displacement, for parameters $\mathcal{P}_1$ and $\mathcal{P}_2$, respectively, with amplitude of external force (F^{ext}_{bm}). The peak BM displacement for the OoC with no HB activity is shown with red lines and the peak BM displacement for the OoC with both HB activity and somatic motility is shown with blue lines. Both adaptation mechanisms lead to increased low stimulus BM displacement and an earlier onset of nonlinear compression. The phasic adaptation (Fig. 2.12(a) blue line) achieves this by injecting power generated by the HB activity whereas the anti-phasic adaptation mechanism (Fig. 2.12(b) blue line) increases the somatic power gain.

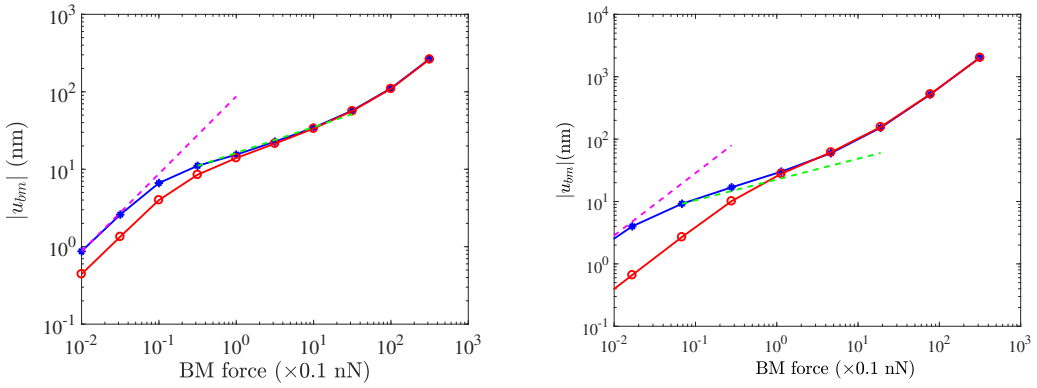

Figure 2.12: The variation of peak BM displacement with amplitude of external stimulation for (a) $\mathcal{P}_1$ parameters at 0.4 cm from stapes and (b) $\mathcal{P}_2$ parameters at 1.2 cm from stapes. The peak BM displacement amplitude for the OoC with somatic motility only is shown in red. When HB activity is added to the system, the low stimulation BM displacement is increased along with a markedly earlier onset of nonlinear compression (blue). The dashed lines illustrates the linear (magenta) and nonlinear (1/3 power low; green) slopes for lower and medium frequency ranges, respectively.

2.9 Discussion

The relative importance of the HB and somatic force generation to amplification of the OoC motion has been long debated. Lagarde et. al. [47] and Santos-Sacchi *et al.,* [17] have proposed that the somatic motility is the basis of OoC amplification. However, more recently, Nin *et al.,* [48] have shown that by blocking the hair bundle motility, the onset of nonlinear is shifted to higher stimulus level along with a decrease in the low stimulus gain. In this study, we have found that the power gain by hair bundle motility is 10^3-10^5 times smaller than the somatic force. Hence, it is unlikely that hair bundle motility itself can amplify OoC motions and that OHC somatic motility is the the primary driver for cochlear amplification. However, Fig. 2.12 shows that by coupling active hair bundle motility to somatic motility, it is possible to hasten the onset of compressive nonlinearity along with an increase in the low stimulus gain. Experiments by Zheng [49] and Cooper [50] have shown that the nonlinear

compression in an active cochlea starts close to 20 dB SPL. Earlier modeling work by Meaud and Grosh [51] has shown that with somatic motility alone, the nonlinearity can be achieved around 40 dB SPL. As shown in Fig. 2.12, the coupling of HB activity with somatic motility can reduce the onset of nonlinearity.

More recently, Nin *et al.,* [48] has shown that the nonlinear compression persists but is reduced when the somatic motility is perturbed or the tip links are broken. This is in line with our results as blocking the somatic motility or the transduction current destroys the coupling of the hair bundle adaptation mechanism to the somatic motility. In this case, the somatic motility can still induce nonlinear compression, albeit at a larger stimulus level and with reduced low stimulus gain. We conclude that the somatic force is the primary force transducer in the OoC and that the hair bundle adaptation mechanism most likely controls the larger somatic force by fine modulation of the gating force and MET current.

CHAPTER III

TM Shear Mechanics Activates the Cochlear Amplifier

3.1 Introduction

Cochlear mechanical responses show a nonlinear characteristic such that the lower SPLs produce higher gains relative to higher sounds [44, 52, 53]. Although nonlinear responses of the cochlea to input sounds are well-known hallmarks of normal hearing, the OoC contribution on the nonlinear amplification is still poorly understood. The onset of the nonlinearities are observed to occur $\sim 1/2$ octave below the characteristic frequency (CF), as shown in the Fig. 3.1 for mice measurements [53].

Table 3.1 shows the frequency corresponding to the onset of the nonlinearity (we will call this frequency f_{shift}) compared to the CF of the measurement location for different experimental data. It is noted that the f_{shift}/CF ratio varies among different experiments (animals), however, it is in the range of 0.6 to 0.7, suggesting that the principal working mechanism could be similar. This observation reveals that a mechanism at the shift frequency possibly activates the cochlear amplifier, serving to localize and thus sharpen the frequency region for lower SPLs.

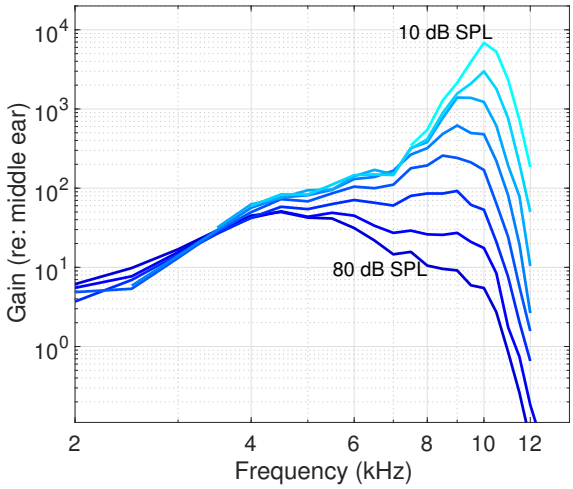

Figure 3.1: BM displacement gain measured from mice cochlea [53]. Gains are calculated by normalizing the displacement magnitudes of the BM for a range of SPLs (10 to 80 dB SPL with 10 dB increment)to the middle ear displacements. At low frequencies BM responses are linear while the nonlinearity onsets at a frequency $\sim$ 1/2 octave below the CF=10 kHz

Table 3.1: Comparison frequency of the onset of nonlinearity (f_{shift}) to the CF of the measurement location from different experimental data.

Animal	CF(kHz)	$f_{shift}(kHz)$	f_{shift}/CF	Source
Chinchilla	10	7	0.7	[44]
Gerbil	13	22	0.6	[52]
Mouse	6	10	0.6	[53]
Guinea pig	15	10	0.66	[54]

Dong and Olson [52] explored the underlying mechanism of the cochlear amplifier by measuring sound-evoked electrical and mechanical responses *in vivo*. They showed that the frequency dependence of relative phase between the OoC motion, intracochlear pressure, and extracellular potential in the ST are related to the conversion of electrical to mechanical energy and to amplification. The extracellular voltage is shown to undergo a phase shift at frequencies slightly below the peak [52, 55], that coincides with the onset of the nonlinear amplification. This phase shift is not observed in the pressure and displacement responses. It is hypothesized that this phase

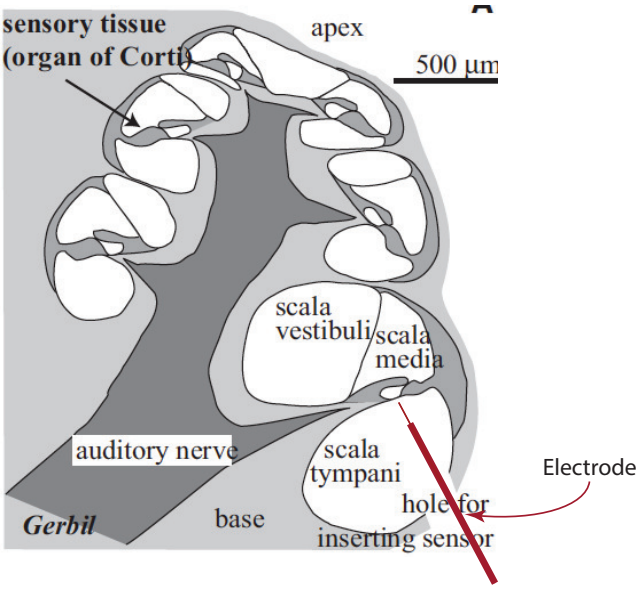

Figure 3.2: Voltage measurements inside the ST. An electrode is inserted inside the ST and positioned close to the BM to measure the receptor potential responses to sound stimulation in gerbil.

difference between the electrical and mechanical responses gives rise to an effective power generation of the OHC somatic force [52]. However, the origin of this phase shift within the mechanics of the cochlea is not well understood. The purpose of this study is to test this hypothesis (phase transition) and identify the underlying mechanism using a mathematical cochlear model.

3.2 Method

The experimental data in conjunction with simulations are used to study nonlinear amplification in the cochlea. The sound-evoked voltage inside the scala tympani was measured for a range of frequencies and pressure levels. The experimental data are from *in vivo* measurements of the gerbil cochlea. Animal preparation and single tone stimulation were as described in Dong and Olson [52] using procedures approved by the Columbia University Medical Center Institutional Animal Care and Use Committee (IACUC). A small hole (diameter $\sim$100 μm) was hand-drilled through the bony

wall of the ST at the first turn of the gerbil cochlea with best frequency (BF) around 15.5 kHz. To ensure a healthy cochlea after cochleostomy, compound action potential (CAP) was measured before and after the fenestration. A tungsten electrode, 75 μm in diameter (FHC Inc, Bowdoin Maine), was inserted into the ST and advanced close to the BM (based on experience with the anatomy, the distance was $\sim$20 - 100 μm) using a micropositioner. The electrode was coated to its tip and had a resistance of $\sim$ 1M Ω. The voltage responses to acoustical stimuli were measured. Figure 3.2 shows a schematic of the experimental configuration.

We have used a 3-dimensional model of the cochlea in order to interpret the experimental data and proposed an underlying mechanism. The parameters used for this study are the same as those introduced in [56] except for the parameters listed in Table 3.2. The active process in this model is incorporated by the piezoelectric-like behavior of the OHCs, arising from their somatic electromotile properties.

Table 3.2: Parameter values that are changed from [56]; x is the longitudinal distance from the stapes (cm)

Parameter	Description	Value
K_{tms}	TM shear stiffness per unit length	$3 \times 10^4 exp(3.75x)\ N/m^2$
C_{tms}	TM shearing damping coefficient per unit length	0
C_{tmb}	TM bending damping coefficient per unit length	$0.1\ Ns/m^2$
C_{bm}	BM damping coefficient per unit length	$0.085\ Ns/m^2$

3.3 Notch in the Electrical Responses

Figure 3.3 shows the *in vivo* measurements of the sound-evoked electrical responses inside the ST for a range of frequencies and sound pressure levels (SPLs). The frequencies in this plot are normalized to the characteristic frequency (f_{CF}^{exp} or CF) defined as the peak frequency of the lowest SPL response. The voltage responses show peaks near to CF (resembling the BM response). The amplitude peak and corresponding

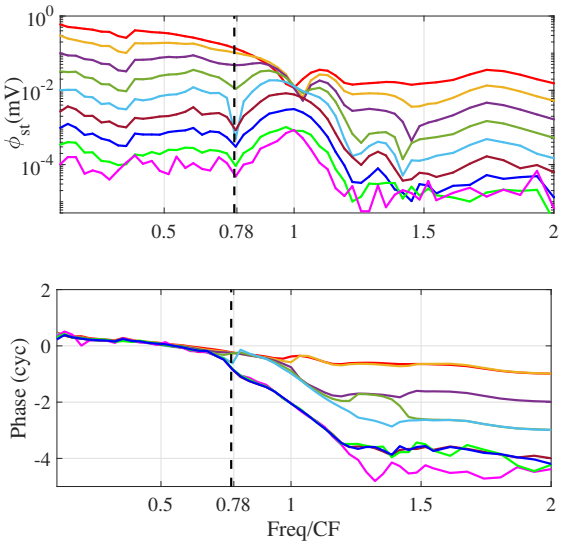

Figure 3.3: In vivo measurements of the electrical responses to pure tone stimuli varying from 0 to 80 dB relative to 20 μPa SPL with 10 dB increment (higher SPLs generates larger voltages). The voltages are measured inside the ST, close to the BM. Frequencies are normalized to the peak frequency of the lowest SPL; CF=15.5 kHz. The dashed lines illustrate the frequency where the notches and the associated phase shift occur near $f^{exp}_{shift} = 0.78CF$.

traveling wave phase accumulation verified that within a frequency region where these are present, the responses are predominantly generated by local OHCs. To further support this statement, in [52] electrical and mechanical responses were recorded together and showed similar tuning and similar traveling wave phase accumulation. This would not happen if the electrical responses were due to current from remote OHCs, in regions with different tuning and phase. The notches and an attendant phase shift occur at frequencies near $f^{exp}_{shift} = 0.78 f^{exp}_{CF}$, illustrated by vertical dashed lines, and are not observed in the mechanical and intracochlear pressure responses [52, 55]. This frequency does locate the lowest frequency of the nonlinear portion of the input-output relations of the BM displacement and pressure in response to acoustic stimuli [52, 55].

Figure 3.4 shows the control test results where the ST voltages are measured for two different electrodes and it is verified that the notches are not artifacts depending

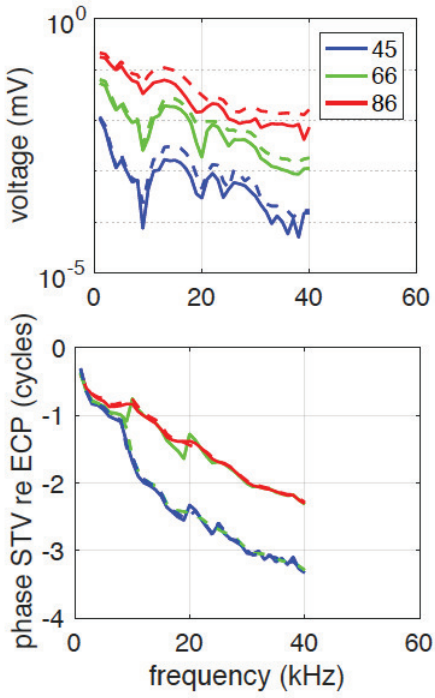

Figure 3.4: Control test measurements. Two different microelectrodes (solid: FHC Inc, Bowdoin Maine and dashed: AM Systems, SequimWA [52]) are tested and it is verified that the notches are not artifact of the electrode type.

on the electrodes characteristics (*e.g.* impedance).

In Fig. 3.5, the model predictions of the ST electrical potential (ϕ_{st}), BM transverse motion (u_{bm}), and the TM shear (u_{tms}) and TM bending (u_{tmb}) motions as well as the OHC HB rotation relative to the RL (u_{hb}) are presented. The amplitudes in this plot are normalized to their individual peak values and the frequencies are normalized to the CF of the BM in our model. The ST voltage shows a peak slightly below the CF and a notch (and corresponding phase shift) at $f^{mod}_{shift} = 0.77 f^{mod}_{CF}$. As found in the experimental data [52, 55], the notch is not observed in the BM responses. Our model predicts a notch in both the HB motion and the ST potential.

In Fig. 3.5, the responses of all variables are seen to be in phase with one another at low frequencies. Above f^{mod}_{shift} the phase relations bifurcate. Predictions of the relative phases between ϕ_{st} and the mechanical response variables are shown at $0.8 f^{mod}_{shift}$ in Fig. 3.6(a) and at CF in Fig. 3.6(b), using the same color code as in the legend of

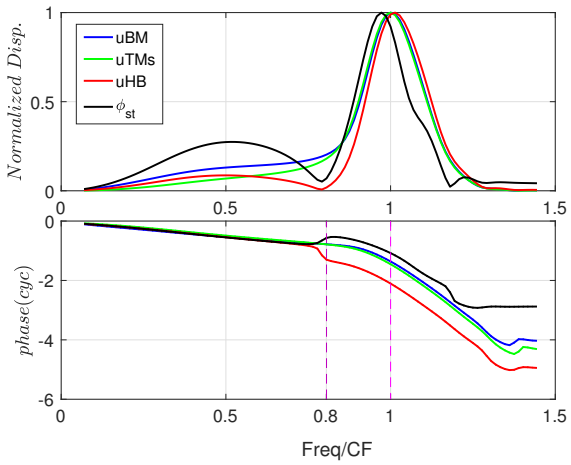

Figure 3.5: The model predictions of the ST voltage (ϕ_{st}), BM transverse (u_{bm}), TM shear (u_{tms}) and HB deflection (u_{hb}) motions under acoustical stimulation; amplitudes are normalized to their relative peaks and frequencies are normalized to the CF=14.4 kHz.

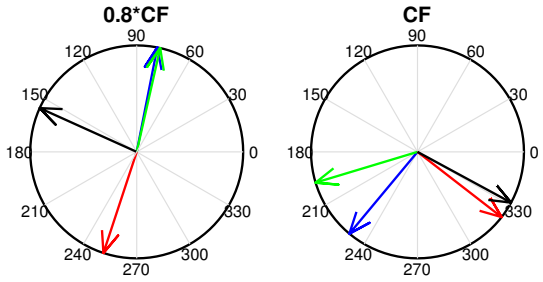

(a) (b)

Figure 3.6: The model predictions of relative phases between electrical and mechanical responses at frequencies (a) 0.8 CF and (b) CF. The color code is as in Fig. 3.5; u_{bm} (blue), u_{tms} (green), ϕ_{st} (black), u_{hb} (red).

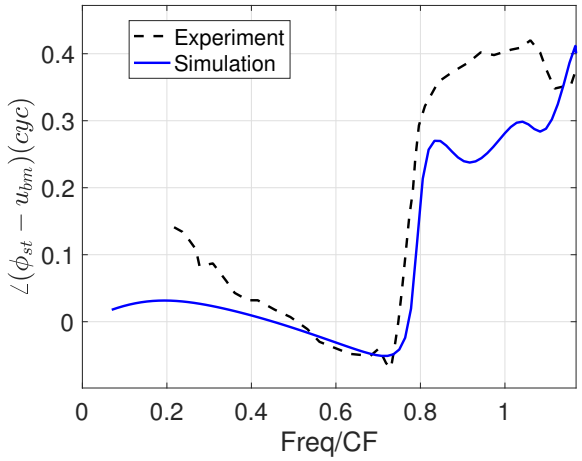

Figure 3.7: Phase difference of the extracellular potential and the BM displacement; experimental data (40 dB SPL, from Dong and Olson [52]) and simulation results.

Fig. 3.5. At $0.8f_{shift}^{mod}$, slightly above the shift frequency, the ST voltage is shown to lead the BM and TM shear motions by ∼1/4 cycle (Fig. 3.6(a)) and nearly maintain this difference at CF (Fig. 3.6(b)). The phase difference between the HB rotation and the voltage monotonically increases from a 1/4 cycle at (Fig. 3.6(a)) to nearly a full cycle (*i.e.,* in phase) at CF (Fig. 3.6(b)). Therefore, while there is a bifurcation point at the shift frequency which results in differences in the phases, the phase difference of all quantities remains nearly constant except for that of the HB, which varies with a different dependence on frequency. As an additional note relating the data of Fig. 3.3 and the model of Fig. 3.5: Fig. 3.5 shows that the voltage notch (black curve) occurs when the BM and TM motions (blue and green curves) are nearly equal in size and phase. The depth of the notch is sensitive to these two conditions and variations in notch depth, as observed in Fig. 3.3, could be produced by very small variations in BM or TM motion. This likely led to the deeper notch observed at 40 dB SPL.

To study the phase transition, we plot the frequency dependence of the measured (from [52]) and predicted phase difference between ϕ_{st} and u_{bm} in Fig. 3.7. Both measurements and theory are seen to undergo a dramatic phase transition of 35% of a cycle (theory) and a measured shift of nearly 45% of a cycle for frequencies

greater than the shift frequency. A phase transition between the HB deflection and BM transverse motion occurs at the notch frequency which is similar to the in vivo measured data by Lee *et al.,* [53]. They show a phase shift of their estimate of the HB rotation relative to the transverse motion of the BM of the mouse at a frequency roughly 70 % of the CF (CF=10 kHz) of the measurement location.

3.4 Mechanism of the Notch

Our model predicts both the experimentally measured phase relation between the ST voltage and BM displacement (Fig. 3.7) and the location of the notch in the voltage amplitude (*cf.* Figs. 3.3 and 3.5). The notch frequency in our model corresponds to the resonance frequency of the uncoupled TM in the radial direction ($2\pi f_{shift}^{mod} = \sqrt{K_{tms}/M_{tms}}$) where K_{tms} is the stiffness of the attachment of the TM to the spiral limbus and M_{tms} is the TM mass (see Fig. 1.1). This finding is tested in our 3-dimensional cochlear model by varying the TM shear stiffness and tracking the notch frequency as shown in Figure 3.8; increasing K_{tms} shifts the notch to higher frequencies. Moreover, Fig. 3.12 denotes that increasing damping of the TM motion (for instance, subtectorial viscosity loss) decreases the notch depth.

As described by Gummer *et al.,* [57] and our present analysis, the uncoupled resonance of the TM and its limbal attachment produces a phase shift of the shear force applied onto the apical pole of the HB. This shift occurs as the uncoupled TM impedance looking in from the HB attachment shifts from stiffness controlled to mass controlled at higher frequencies. At resonance, the force that can be applied to the tip of the HB is minimal (zero in the undamped case). Experimental evidence from mutant mice with TM unattached to the OHC HBs indicates that the resonance frequency of the uncoupled TM is near to or below the local CF [53]. Of course, the *in situ* response of the OoC is more complicated as it is comprised of a multi-degree-of-freedom system with damping, which could slow some of the frequency dependence

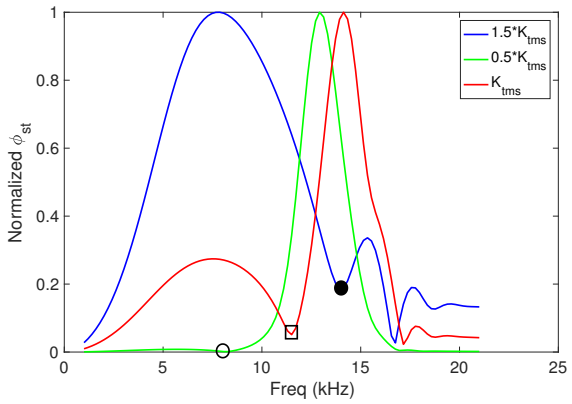

Figure 3.8: Notch location depends on the TM stiffness. The TM shear stiffness is changed from the default value (K_{tms}) and it is observed that the notch frequencies (denoted by markers) shifts up when the K_{tms} increases.

phase transitions.

3.5 What is *TM Resonance*?

While the concept of the resonant TM has been speculated upon for many years, its the importance on the mechanics of the cochlea is still debated. The idea of the TM resonance first was introduced by Zwislocki [58] in a model of the cochlea. He proposed that a resonance mechanism in which the mass is the mass of the TM and the compliance is the stiffness of the outer hair cell stereocilia occurs inside the microstructure of the OoC. Allen [59] discussed this idea further and introduced a model assuming that the compliance is the elastic TM material rather than the stiffness of the stereocilia, as assumed by Zwislocki [58]. In the Allen model a spectral zero (an anti-resonance) is located below the CF and it is argued that any measured neural tuning curve may be closely matched by adjustment of the model spectral zero. The spectral zero is not realizable in a model without mechanical interaction between the TM and stereocilia [59]. Subsequent studies by other researchers (e.g [56, 57, 60] indicated that the TM resonance hypothesis is capable of explaining some important features of the cochlear mechanics. It should be stressed that the expression of TM

resonance is somewhat ambiguous as it is not the resonance of the TM within the fully coupled OoC (electrical, mechanical, and fluid loaded) system. As with any complex multi-degree of freedom system, the coupling stiffness and active forces affect the system resonant frequency. The resonance frequency of the TM should be measured when uncoupled from OHCs as don by Lee [53]. They measured the TM frequency response when detached from the OoC and they found the resonance frequency to be slightly below the CF which is consistent with findings of modeling efforts [56]. At the resonance frequency of the uncoupled TM the mechanical impedance is minimal (zero for undamped system), hence, TM cannot transfer a load to the stereocilias. Furthermore, they demonstrate that the unattached TM undergoes a resonance between 5kHz and 8 kHz (most evident in the spatial mode shape shift seen in Movie 1 of their Fig. 9I and 9J). This is consistent with the modeling result, where the TM resonance is roughly 1/2 octave below the CF [56].

3.5.1 Simple Model Representation

In order to better understand the comprehensive model and experimental results, a much simpler two-degree-of-freedom (2DOF) system is considered as shown in Fig. 3.9. In this system two masses (m_1 and m_2) are connected through several mechanical elements (springs and dampers) (see Fig. 3.9-a). As shown in Fig.3.9-b this simple system represents a conceptual model for the BM and TM mechanical interactions. The HB deflection in this model is analogous to the difference between x_1 and x_2 (representing BM transverse and TM shear modes, respectively). The frequency responses, x_1 and x_2, are plotted in Fig. 3.9-c along with their relative displacement, x_1-x_2. The responses show two peaks associated to the resonance frequencies of this 2DOF system. Moreover, it is noted that the x_1-x_2 quantity shows an antiresonance node at a frequency which coincides with the resonance frequency of m_1 when detached from m_2. At this frequency the impedance of mass m_1 (within the coupled

system) is minimal, giving rise to a node in the force transferred to the mass m_2. Hence, we see an antiresonance node in the relative motion of the masses, x_1-x_2, which is analogous to the deflection of the HB (see Fig. 3.9-b).

For sake of simplicity lets consider $c_1 = c_2 = 0$ and find the closed form relation for x_1 and x_1 displacements:

$$\begin{aligned} x_1 &= \frac{k_2 F_0}{m_1 m_2 \omega^4 - k_2 m_1 \omega^2 - m_2 k_1 \omega^2 + k_1 k_2 - m_2 k_2 \omega^2} \\ x_2 &= \frac{F_0(k_1 + k_2 - m_1 \omega^2)}{m_1 m_2 \omega^4 - k_2 m_1 \omega^2 - m_2 k_1 \omega^2 + k_1 k_2 - m_2 k_2 \omega^2} \end{aligned} \tag{3.1}$$

Form Eq. 3.1 we can find that the amplitudes of $x_1 - x_2$ is minimum when $\omega = \sqrt{\frac{k_1}{m_1}}$ which is the resonance frequency of the mass m_1 when detached from m_2.

3.6 Comparison to in vivo Data

We note that because the TM will be stimulated by the fluid between it and the underlying hair cell epithelium, its motion will be more complex inside the cochlea than the simple model of Fig. 3.9). However, the resonant TM scheme finds support from *in vivo* and *in vitro* observations. For instance, the recent OCT measurements by Lee *et al.* [53] in mice shows a notch similar to that shown by our simple 2DOF model (Fig. 3.9-c). Using their reported data (Fig. 2 of [53]), the vector subtraction of the BM transverse and TM radial displacements for a range of frequencies and intensities are plotted in Fig. 3.10(a). This calculation takes into account the vibratory magnitude and phase of each structure. It is observed that there exist notches near 7.5 kHz while the CF for this preparation is at 10 kHz. At the notch frequency the amplitudes and phases of the BM transverse and TM radial are nearly equal as in the mechanism shown by the simple 2DOF model (Fig. 3.9). We also note that the depth of the notches is level dependent such that higher SPLs demonstrate smaller

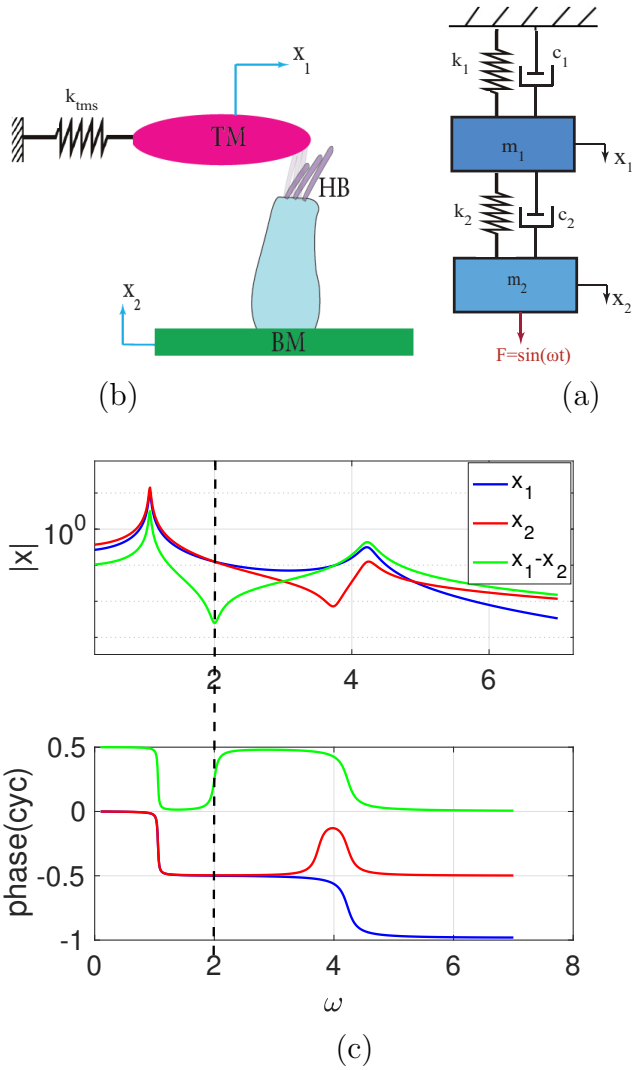

Figure 3.9: An antiresonance node in the frequency response of a 2DOF system describes the notch observed in the complex microstructure of the OoC. (a) a 2DOF system (b) schematic of the equivalent BM and TM degree of freedoms (c) frequency response of the system shown in (a) for parameters: $m_1 = 1$; $m_2 = 2$; k1 = 4; k2 = 7; c1 = 0.1; c2 = 0.1. The x_1-x_2 response shows a node at the resonance frequency of the uncoupled m_1: $\omega_1 = \sqrt{\frac{k1}{m_1}} = 2$

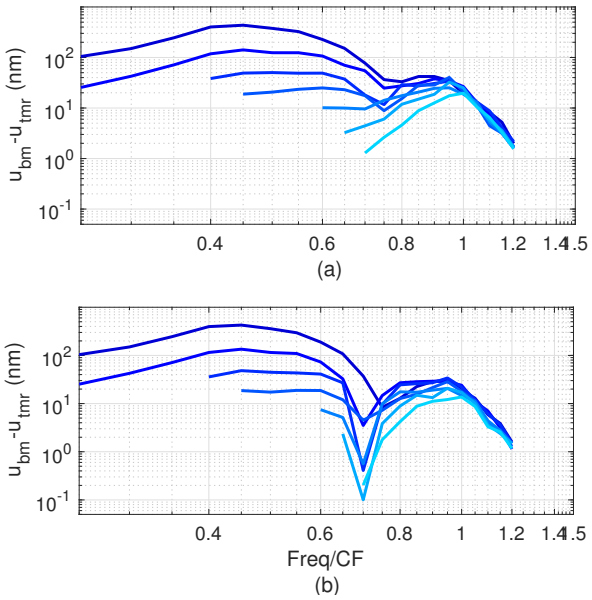

Figure 3.10: Extrapolation of the HB notches from BM and TM *in vivo* data [53]. (a) The vector subtraction of displacements of the BM transverse (u_{bm}) and TM radial (u_{tms}), $|u_{bm} - u_{tms}|$, from *in vivo* data extracted from Fig. 2 of [53] for live mouse preparation. (b) The BM/TM relative motion When ignoring the phase differences; $|u_{bm}| - |u_{tms}|$. SPLs are from 20 to 80 dB with 10 dB increment.

notches than the higher SPLs.

It is noted that *in vivo* phase measurements are susceptible for errors; hence it is reasonable to consider this notation when interpreting the data. When assuming no phase difference between the BM and TM motions at low frequencies, as predicted by our model (see Fig. 3.3), the amplitude difference between BM transverse and TM shear (radial) motions are illustrated in Fig. 3.10(b). The notches are more noticeable in this figure than Fig. 3.10(a).

3.7 OHC Power Amplification

The OHC somatic force is proportional to the cells transmembrane potential [61] as described in Eq. 1.3. Hence, the phase relation between the ST voltage and the BM/RL motions indicates the OHC active power flow direction. The phase transition

between ST voltage and BM motion (Figure 3.7) sets the condition for the OHC somatic force to inject power into the BM motion. The phase shift at the bifurcation frequency brings the phase difference between the somatic force and BM displacement into the generative region. At the CF a phase difference between the somatic force and BM displacement reaches near 90 degree. Hence, the active force is nearly in phase with the BM velocity; a condition required for the effective power injection on the BM motion. Figure 3.11 shows power interaction between OHC and BM/RL for frequencies normalized to the CF. The OHC power is calculated as:

$$P = \frac{1}{2} Re\{F_{som} v^*\} \tag{3.2}$$

where $*$ denotes the complex conjugate and v represents the velocity of the BM or RL. Moreover, $F_{som} = \epsilon_3 \Delta\phi_{ohc}$ is the OHC somatic force (see Eq. 1.3) which is proportional to the OHC transmembrane potential ($\Delta\phi_{ohc}$).

A negative value in this plot indicates power dissipation while generative regions are associated to positive powers. It is noted that the OHC power deposition to the BM is changed from dissipative (below the f_{shift}) to generative (around the CF) while the RL side is dissipative near CF.

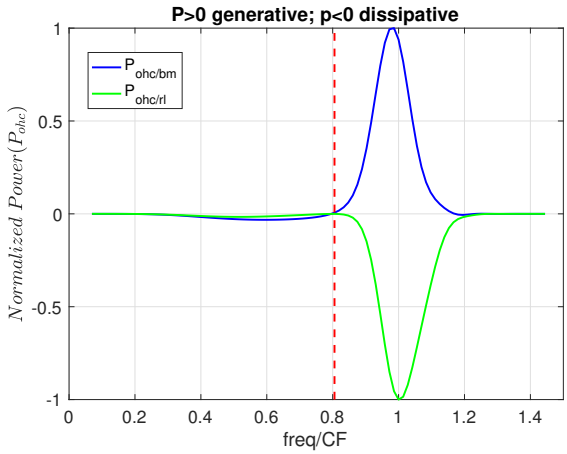

Figure 3.11: Frequency dependence of the active power deposition between OHC and BM. $P < 0$ indicates power dissipation while $P > 0$ denotes power generative region. The OHC powers are calculated for the BM (blue curve) and RL (green curve) motions. For the sake of visual clarity, powers are normalized to their relative peck values. The vertical dashed line indicates frequency boundary where the power deposition changes from dissipative to generative.

3.8 Level Dependency

The notch in the voltage data is generated when the BM transverse and TM radial motion are equal in amplitude and phase (see Fig. 3.9). The depth of the notch is sensitive to these two conditions and variations in notch depth, as observed in Fig. 3.3, could be produced by very small variations in BM or TM motion. This likely led to the deeper notch observed at 40 dB SPL . At SPLs $>$ 60 dB the notch is washed out, likely due to nonlocal OHCs contributing to the measured voltage.

The depth of notch is also damping dependent in the model and can be indiscernible if damping is increased. This finding is shown in Fig. 3.12 where increasing the TM shear damping has decreased the notch depth. The switch of the phase of the voltage (and HB motion in our model) is not, however, damping dependent. The phase transition between mechanical and electrical responses are evident even for higher SPL sounds as shown in Fig. 3.13(a) from experimental data [52] and from our model predictions in Fig. 3.13(b).

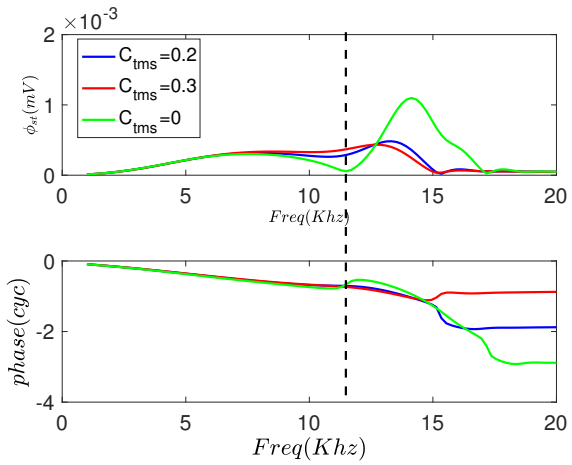

Figure 3.12: Notch dependence on the damping. It is observed that increasing TM shear damping (C_{tms}) decreases the notch depth.

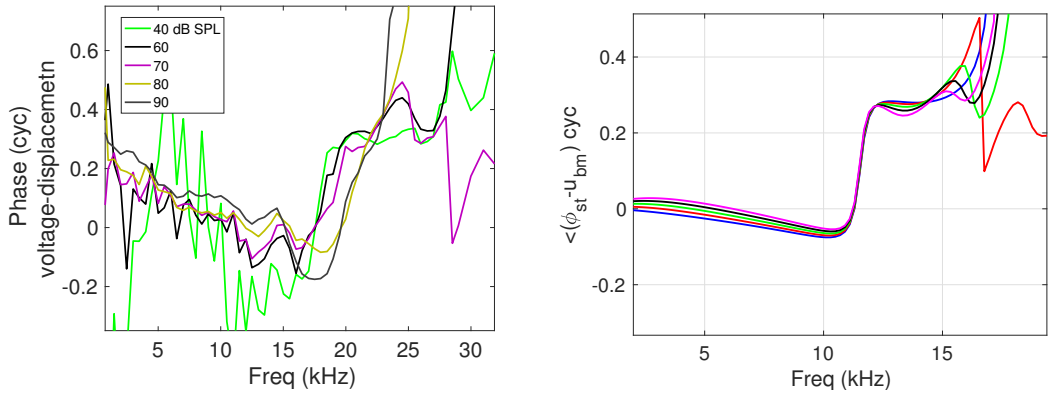

(a) (b)

Figure 3.13: Level dependence of the phase transition observed form (a) experimental data [52] and (b) model. In the model the activity level is changes by varying the EMET scaling factor μ as introduced in Eq. 1.1; $\mu = 0.2, 0.4, 0.6, 0.8, 1$.

The phase shift mechanism is based in passive mechanics, and sets the conditions necessary for amplification, while the size of the amplification, which diminishes in relative terms as SPL increases, is limited by the saturation of OHC mechano-transduction current.

3.9 Discussion

It is hypothesized that the phase transition below the CF (starting from f_{shift}), introduces a mechanism to set the condition for activation of the cochlear amplifier. At low frequencies, the in-phase motion of the cochlear structural and electrical responses (Fig. 3.5) implies that upward movement of the BM pivots the stereocilia to open ion channels and increase current flow in the OHCs, depolarizing the cells. The experimental data shown in Fig. 3.3 reveal that the ST voltage undergoes a phase shift at frequencies below the CF that was not seen in the pressure or displacement responses [52]. This phase shift or bifurcation point coincided with the onset of nonlinearity in this experimental data [52]. The cochlear nonlinearity is a manifestation of the active process we hypothesize to be mediated by the OHC somatic forces. The extracellular voltage is a measure of OHC MET current, flowing through the channels into the cell and generating the somatic-based active force resultant on the basal (Deiters Cells/BM) and apical (RL) poles of the OHCs. The OHC somatic force is proportional to the cell's transmembrane potential. Hence, the phase relation between the ST voltage and the BM/RL motions are also related to electromechanical power transfer.

Our model predicts the notch in the extracellular voltage as well as the phase relations observed from the experiments. The notch frequency in the model corresponds to the TM radial resonance obtained when the TM is attached to the limbus but uncoupled from the OHC cilia. At this resonance, the shearing force applied to the HB by the TM is minimum, resulting in smaller HB deflection, current transductions, and the notch in voltage. Our analysis of the model results shows that the phase shift around this notch introduces the correct phasing between mechanical and electrical responses for effective power amplification. Hence, the model results implicate a central role of the TM in amplification.

The hypothesized mechanism for the cochlear amplifier is illustrated in a flow

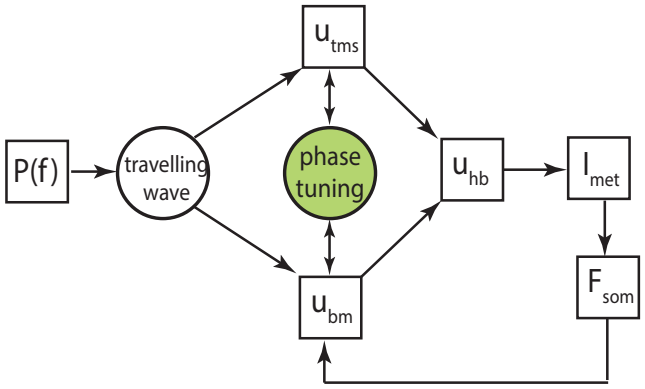

Figure 3.14: A hypothetical system diagram of cochlear amplification. The input sound pressure P(f) with frequency f, creates a traveling wave inside the cochlea, giving rise to the vibrations of the OoC components (e.g, BM, TM, HB). A passive mechanism based on the mechanical interaction between the OoC components sets the phasing condition essential for power amplification mediated by the active force (Fsom).

chart shown in Figure 3.14. In this mechanism, a feedback process that relies on the operation of the MET channels and OHC electromotility provides an active force to the OoC components (i.e BM and RL). The input sound pressure creates a traveling wave along the cochlea which generates vibrations on the OoC components (e.g BM, TM, HB). Deflection of the HBs, induces transduction current through the MET channels giving rise to an transmembrane potential on the OHC. An active somatic force is, then, applied to the BM to provide an amplificatory gain and boost the vibratory responses. A phase tuning mechanism, controlled by the TM and BM mechanical interactions, activates the power amplification at frequencies below the CF. Our model predicts that this phase tuning is essential to observe realistic responses. This phase shift mechanism is based on passive mechanics and set the conditions necessary for amplification. The size of the amplification, which diminishes in relative terms as SPL increases, is limited by the saturation of OHC MET current.

As we have presented here, the resonant TM scheme finds support from *in vivo* and *in vitro* observations, and a detailed physiological model. We note that while a notch is consistently seen in the gerbil ST voltage measured in the present study, such

a notch was not observed in the guinea pig OoC voltage measurements by Fridberger et.al, [62]. This discrepancy could be due to different techniques used for voltage measurements or another as yet unknown effect. Recent advances in imaging motions within the OoC will shed further light on these questions.

CHAPTER IV

Estimation of the OHC Somatic Power Using In Vivo Data

4.1 Introduction

The cochlea detects and amplifies the input sound through a nonlinear process. Two mechanisms have been proposed to undertake the active amplification: OHC somatic motility and HB motility. Since the discovery of OHC somatic electromotility [24] these cells have been the focus of investigation as a mediator of electrical-structural interaction and of amplification. Extensive research studies have been conducted to identify electromechanical properties of the OHC. The electrically induced length changes of the OHC produces an active force to the OoC components and boosts their sounds-borne vibrations; hence, OHC apparatus converts electrical energy to mechanical. The electrical low pass filtering of the cell's transmembrane potential has been cited as a limitation for its ability to generate power *in vivo* at higher frequencies. However, other studies [23] questioned this argument and showed that the OHC low pass filter does not limit its amplifactory property. The other important question regarding the efficacy of the OHC motile process is capability of this process for producing enough force to enhance mechanical response of the OoC. It is not yet possible to simultaneously measure all the relevant quantities (*e.g.* OHC intracellular

potential together with BM and RL motions) for *in vivo* measurement of the somatic power. Meaud and Grosh [51] used a computational model to estimate powers generated by the OHC and HB active processes. Iwasa [63] studied effect of loading on OHC dynamics by introducing a simple one-dimensional model for electromotility of OHC in a dynamic environment. Wang *et al.,* [64] studied OHC power deposition in a model of mouse cochlea. They calculated the net power generation/dissipation in a cross section of the cochlea due to OHC active forces together with fluid viscous dissipation. However, they have not included the subtectorical fluid loss in their calculations.

In order to test capability of the OHC active process hypothesis, the power generation by the OHCs should be calculated and compared with input acoustical power into the cochlea. Ramamoorthy *et al.* [14] estimated the OHC power deposition at the peak frequency (CF), using in vivo data of the BM and RL vibrations along with theoretical estimations of the cochlear electrical responses. They show that the OoC is nearly optimized to receive maximum somatic power *in vivo* and that the estimated somatic power could account for the active amplification. However, they have not taken into account the phase relation between the somatic force and BM/RL motions.

The somatic force of the OHC is proportional and in phase with the cell transmembrane potential [65, 66]. Hence, in order to quantify the power deposition of the OHCs, the cell transmembrane potential should be measured. Because the *in vivo* measurements of the intracellular potentials are very invasive and challenging, we seek a method to estimate them from measurable quantities. A novel method is proposed to calculate the OHC transmembrane potential using the extracellular voltage measured inside the scala ST. Then, the transmembrane potential is used to estimate the active somatic force applied to the BM and RL on basal and apical sides of the OHCs, respectively. The *in vivo* power interaction between the OHCs

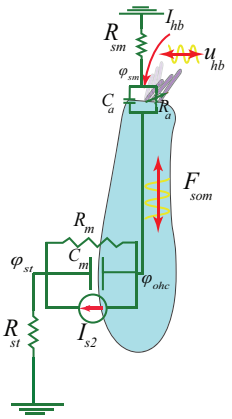

Figure 4.1: Schematic of an isolated OHC and corresponding electrical circuit (see Fig. 1.2)

and other OoC components, are investigated and compared with the literature. This method is tested by our comprehensive computational model of the cochlea.

4.2 Methods

The schematic of an isolated OHC together with an electrical circuit model corresponding to the membrane electrophysiology are demonstrated in Fig.4.1. This circuit model comprises the electrical impedance of the cochlear tissues and biological batteries in the stria vascularis (see Fig. 1.2). The deflection of the HBs (u_{hb}) triggers the MET channels and gives rise to a current transduction flowing inside the cell. The somatic property of the OHCs [24] transfers the electrical energy into mechanical action in form of cell length alteration (which stimulates OHC somatic motility). This elongation applies an active force (F_{som}) to both BM and RL and based on the phasing between force and velocity of this components could generate or dissipate power.

Measuring transmembrane potential, which is a key component of somatic motility, is invasive and challenging *in vivo* and there are little experimental data available (e.g [66]). We propose a method to calculate the transmembrane potential using extracellular voltage measurements inside the ST in conjunction with an circuit model

of the cross section of the cochlea. From Fig. 4.1 the current flow inside the ST for one cross section of the cochlea is estimated as:

$$I_{st} = \frac{\phi_{st}}{R_{st}} \tag{4.1}$$

where ϕ_{st} and R_{st} represent the ST voltage and resistance, respectively. Assuming no current leakage in longitudinal direction (*i.e.* neglecting current flow in the x-direction; see Fig. A), the transmembrane potential can be calculated as:

$$\Delta\phi_{ohc} = (I_{st} - I_{s2})\, Z_m \tag{4.2}$$

where Z_m is the cell membrane impedance and the current source I_{s2} corresponds to the total current due to the piezoelectric-like behavior of the OHC:

$$I_{s2} = \epsilon j\omega u_{ohc} \tag{4.3}$$

where $\epsilon = 0.1\ nN/mV$ is the mechano-electical coupling coefficient of the OHC [63]. Moreover, u_{ohc} is the OHC compression which is a linear function of the BM and TM displacements as introduced in Table A.1. The advanced technique of the optical coherence tomographic (OCT) is recently used for *in vivo* measurements of u_{ohc} [67]. Hence, the OHC transmembrane potential can be estimated using Eqs. 4.2 and 4.3. As in Eq. 1.3, the active somatic force generated by piezoelectricity properties of the OHCs is then calculated as:

$$F_{som} = \epsilon\Delta\phi_{ohc}\,. \tag{4.4}$$

Table 4.1: Electro-mechanical parameters of the OHC model (see Fig. 4.1).

Property	Description	Value
ϵ	mechano-electrical coupling coefficient	0.1 nN/mV
R_{st}	ST fluid resistance	$10^5\ \Omega$
C_m	OHC basolateral capacitance	$15 \times 10^{-12}\ pF$
R_m	OHC basolateral resistance	$10^7\ \Omega$

4.3 Results

The active somatic forces are calculated by applying our method (introduced in previous section) to available experimental data of the OoC displacements and voltages [52, 62, 67]. The experimental data are shown in Fig. 4.2. Two cases (labeled as A and B) are introduced to refer to the experimental data used in this study. Case A refers to the data from [52] and Case B corresponds to the data obtained from [62]. Moreover, u_{ohc} and u_{rl} data are retrieved from [67] for both cases. The parameters used for the OoC cross section model are listed in Table 4.1.

Figure 4.3 illustrates the OHC transmembrane potential and corresponding somatic force for the two sets of data. Since the measurements are conducted in different locations along the cochlea, frequencies are normalized with respect to the frequency corresponding to the maximum displacement, called characteristic frequency (CF) of the location. The transmembrane potential is estimated about 0.1 mV at the CF (Fig. 4.3-a), which gives rise to a force about 10 pN for each OHC (Fig. 4.3-(b)).

In addition to the magnitude of the active force, its phase relation to the movement of the OoC components is important to determine whether the active force is generative or dissipate. Figure 4.4 illustrates phase relation between the transmembrane potential (which is in phase with somatic force [61]) and BM/RL displacements for the two sets of experimental data. The background color demonstrates the generative (green) and dissipative (red) regions. We note that for frequencies below the BM, the two sets of data are in agreement while close to the CF there is inconsistency.

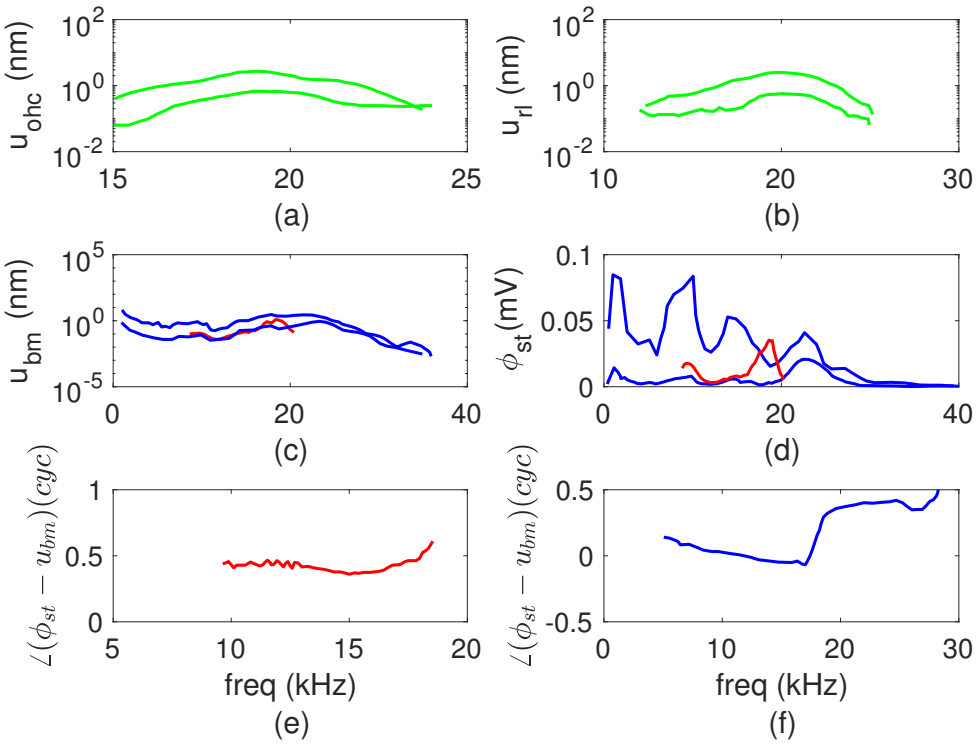

Figure 4.2: Experimental data retrieved from different sources for 40 dB and 80 dB SPL measurements. (a) OHC compression u_{ohc} from [67] (b) RL displacement u_{rl} from [67] (c) BM transverse displacement u_{bm} from [52] (blue) and [62] (red; 40 dB SPL) (d) ST voltage ϕ_{st} from [52] (blue) and [62] (red; 40 dB SPL) (e) phase difference between ϕ_{st} and u_{bm} form [62] (40 dB SPL) (f) phase difference between ϕ_{st} and u_{bm} form [52] (40 dB SPL).

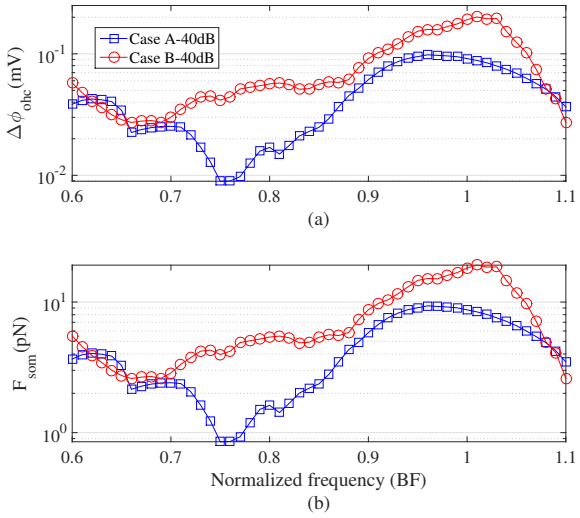

Figure 4.3: Estimated OHC transmembrane potential (panel a) and somatic forces (panel b) from two sets of experimental data by [52] and [62] labeled as Case A and Case B, respectively. The horizontal axis represents the frequency which is normalized with respect to the peck frequency (CF) of the measurement location.

Case A shows that the OHC somatic force is generative in both sides (BM in basal and RL in apical) while the case B demonstrates a dissipation in BM side.

After estimating the OHC active force and corresponding phases, the electro-mechanical power transfer from the OHC and BM/RL elements can be computed as:

$$P_{ohc-bm} = F_{som} v_{bm} \cos(\theta) \tag{4.5}$$

where v_{bm} is BM velocity and θ is the phase between transmembrane potential and BM velocity (Fig. 4.4). Figure 4.5 illustrates power exchange between OHC and BM/RL. Case A indicates that OHC power is injected into the BM motion while case B shows a power dissipation for the BM.

The cochlear nonlinear power amplification is illustrated in Fig. 4.6. In this figure the OHC power gain (somatic power divided by input power) for two SPLs are compared. The input power is calculated as:

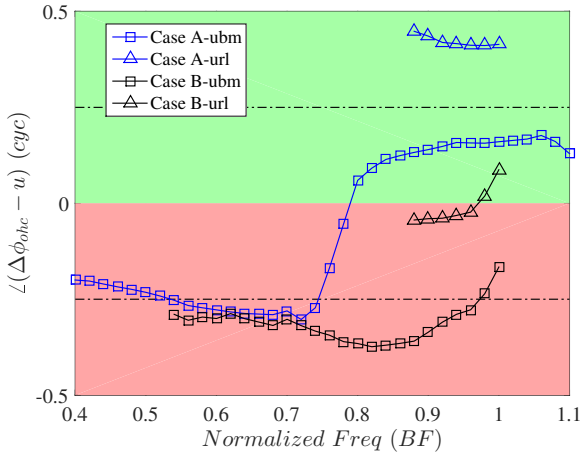

Figure 4.4: Phase between the OHC transmembrane potential and BM/RL displacements. Colors blue and black represent case A and case B, respectively. The background color indicates the regions where the somatic force is generative (green) or dissipative (red). The dash-dot line represents the phase corresponding to the maximum power deposition.

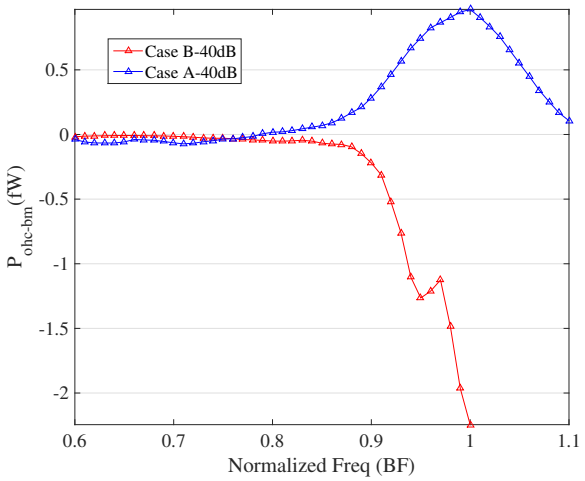

Figure 4.5: Power exchange between one OHC and BM/RL estimated form experimental data of Case A (blue) and Case B (red); positive values correspond to power generation.

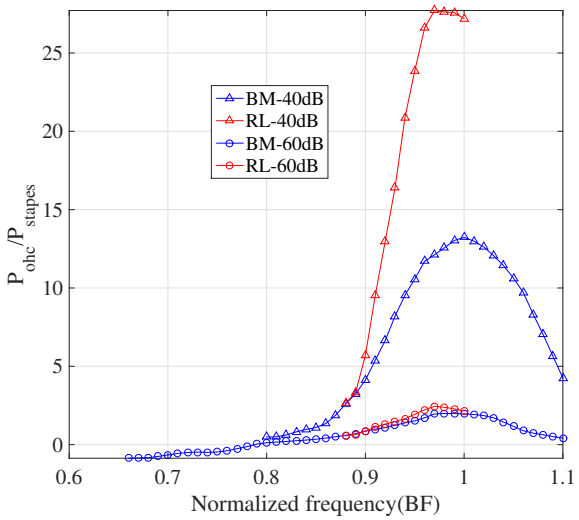

Figure 4.6: The OHC power gain estimated from experimental data of case A ; both BM and RL receive less power gain for higher SPL (60 dB) comparing to the lower SPL (40 dB).

$$P_{stapes} = \frac{1}{2} Re\{Z_s A_s^2 v_s^2\} \tag{4.6}$$

where $Z_s = 2 \times 10^{11} Ns/m^5$ and $A_s = 10^{-6} m^2$ are the stepes impedance and area, respectively [14]. Moreover, v_s is the stapes velocity (0.079×10^{-6} m/s for 40 dB SPL data [14]). It is shown that the lower SPL (40 dB) receives larger gain comparing to higher SPL (60 dB). Moreover, the RL amplification is larger than the BM.

4.4 Validation

Our 3-dimensional cochlear model is used to test the proposed method for estimation of the OHC transmembrane potential. Figure 4.7 compares the FEM results of $\Delta\phi_{ohc}$ with that estimated from the method introduced in Eq. 4.2. It is noted that out estimation is very good for low and high frequencies while there is a larger error close to the CF. Moreover, the phase prediction is matches well with the FEM data. The phase data are, in specific, very important to identify the power generation/dissipation by the OHC electromotility.

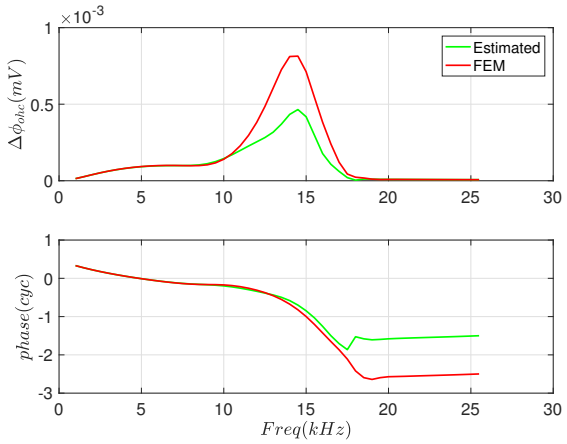

Figure 4.7: Comparing the FEM results with estimated transmembrane potential; $\mu = 0.5$.

In order to improve the accuracy of the estimation method we have used the BM spatial mode shape to extrapolate the spatial voltage data along the ST. Hence, we can include the current distribution along the cochlea (modeled using the cable theory in the FEM model). Figure 4.8 shows the results. We note that the assumption of similar spatial mode shape for the BM as for the voltage data, improves the estimation method significantly.

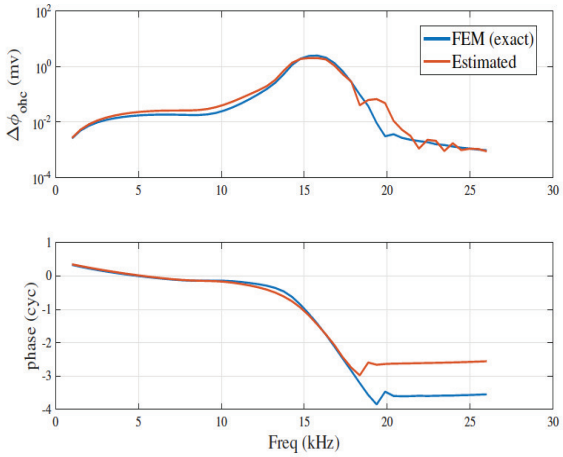

Figure 4.8: Comparing the FEM results with estimated transmembrane potential with assuming similar spatial mode shape for the ST voltage as for the BM; $\mu = 0.5$.

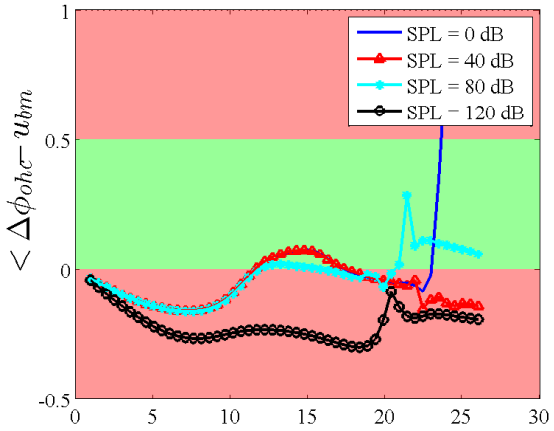

Figure 4.9: Phase relation between transmembrane potential and BM displacement. The background color indicates the generative (green) and dissipative (red) regions.

4.5 FEM Model Predictions

Figure 4.9 illustrates phase relation between the transmembrane potential and the BM displacement for several SPLs calculated from our nonlinear FEM model [56]. Our model predicts that close to the CF the active force is generative for the BM while far from the BM it is dissipative. This result is in agreement with the case A of the experimental data.

4.6 Conclusions

An active process is involved in the cochlea that boosts the sound borne vibration of the OoC via a compressive nonlinearity in the system which enhances frequency selectivity and sensitivity to low level sounds. The somatic motility of the mechanosensory OHC is hypothesized as the key element of the cochlear active mechanism. The OHCs are situated between the BM and RL inside microstructure of the OoC. The mechanoelectrical properties of these cells allows for conversion of electrical energy, induced by actively maintained ionic imbalance inside the cochlea, into mechanical energy (and vice versa). This process results an active force applied on both the

apical and basal ends of the OHCs. In this study, we used the in vivo experimental data on the OHC extracellular receptor potential together with the displacement of the OoC structural components derived from OCT measurements and pressure gradient estimation of the BM velocity to estimate electromechanical energy exchange. The phase relation between somatic force and the BM/RL motions indicate the active power flow direction. A simplified circuit model of the cochlea was introduced in order to approximate the immeasurable quantities (e.g., OHC transmembrane potential). Post processing the experimental data from two separate but related experiments [62] and [67] with our model revealed that the OHC active force dissipates power in the BM side while it amplifies the RL motion. Conversely, another experimental protocol using a single experiment [52] shows that the OHC active power is generative on the BM side (RL displacement was not available from this experiment). The conflicting results point to the need for concomitant OCT and voltage measurements in order to conclusively determine the applied power.

CHAPTER V

Simulation of an Active Excised Cochlear Segment Experiment

5.1 Introduction

In vivo and *in vitro* experiments provide valuable data to expose and analyze the unique properties of the hearing in the auditory periphery. Due to geometrical constraints of the coiled cochlea and also technical measurement limitations, it is difficult to measure the vibration of most regions of the OoC *in vivo*. For instance making a viable measurement of the HB displacement inside an intact cochlea is challenging, because of the inaccessibility of these cells (as discussed in Lukashkin *et al.* [60]). The isolated preparation offers several advantages over existing *in vivo* techniques.

An *in vitro* preparation enables the study of discrete cochlear components. For instance, Beurg *et al.* [68] performed intricate and carefully controlled *in vitro* direct mechanical stimulation of the HB to determine their transduction properties; in this case the TM was stripped off of the preparation to gain access to the HB. As another example, Ghaffari *et al.* [69] isolated the TM to study its traveling wave propagation. Furthermore, the *in vitro* preparations enable us to obtain an integrated understanding of how the individual components interact under mechanical, acousti-

cal or electrical stimulations. Gummer *et al.* [57] prepared freshly isolated sections of the cochlea and investigated contribution of the TM and BM motion to the electromechanics of the OoC. Ulfendahl *et al.* [70] developed an *in vitro* preparation of the guinea pig temporal bone to study the micro-mechanical behavior of the cochlea. This preparation, which is known as ITER, consists of the cochlea opened at the apex, allowing observation of cellular structures within the partition and measurements of cellular vibration. The hemicochlear preparation [71, 72] is another *in vitro* technique that allows access to various cochlear structures with minimal physical distortion. This technique bisects the cochlea such that the tonotopic features of apical, middle and basal regions can be preserved and studied.

An active *in vitro* preparation of a small segment of the cochlea, with minimal physical disruption of the epithelium, is ideal to investigate the cochlear intrinsic dynamics. The *in vitro* preparations of Chan and Hudspeth [3–5] as well as those of Nowotny and Gummer [73] are notable for isolating a segment of the cochlea with controlled mechanical, ionic, and electrical conditions in order to keep the OoC in as pristine state as possible. Both groups demonstrate that the MET channels are kept at least partially operational and measure the inner hair cell (IHC) deflection due to pressure and/or electrical stimulation. These preparations hold the potential for uncovering important structure-function relationships of the auditory periphery, such as the cochlear amplifier. Furthermore, computational simulation of these experiments allows us to analyze the data and explore the influence of variations in mechanical and electrical conditions.

An important question of the biophysics of the cochlea is the effective active mechanism underlying the cochlear nonlinear amplifier. Using the active excised cochlear segment experiment devised by Chan and Hudspeth [3–5] as a model problem, we developed a computational model for studying contribution of the active processes on the cochlear nonlinear response.

The relative contribution of each mechanism to the cochlear performance has yet to be conclusively apportioned. Different techniques have been proposed to study contribution of one active mechanism on the cochlear mechanics with minimal interruption in other mechanism. Santos-Sacchi *et al.* [17] used salicylate, a ototoxicant that works directly on the prestin motor [74] but does not effect on the stereociliar MET channels [75], together with tributyltin (TBT), a chloride ionophore, to alters OHC electromechanical activity and cochlear amplification in a reversible manner. They modulated chloride levels around the basolateral region of the OHCs, a manipulation that should not interfere with the cationic workings of the proposed stereociliar mechanism. Fisher *et al.* [30] developed an optical technique that permits the targeted inactivation of somatic motility without significantly altering passive power transmission. They demonstrated that the somatic active forces interact locally with cochlear traveling waves to achieve enormous mechanical amplification. With recent advances in production of mutants, there was hope to settle the issue of origin of the active process in the cochlea. For instance, a knockin mutant mouse that expresses immotile prestin displays knockout-like hearing thresholds [16], sensitivity [31] and voltage-evoked movements of HBs [32]. Jia and He [32] measured voltage-evoked hair-bundle motions in the gerbil cochlea and prestin-knockout mice to determine if such movements were also present in mammalian OHCs. They observed that the voltage-evoked hair bundle motions are not affected by calcium concentration in the cilary area. Moreover, they measured voltage-evoked hair bundle motions in neonatal gerbils as well as prestin-knockout mice, in the absence of electromotility, and no motion were detected. These findings suggest that prestin-mediated somatic OHC motility is the amplifier.

Although interference with prestin has demonstrated a role for somatic motility in amplification, contribution of the HB motility in the active process remains unclear. The experiments by Chan and Hudspeth [3] along with the study by Kennedy

et al. [22] are the most compelling evidences that support the stereociliary-based amplification in mammals. Kennedy *et al.* [22] demonstrated that the ciliary amplifier is capable of producing sufficient force that could be fast enough *in vivo* to account for amplification, however, technical difficulties precluded the high frequency measurements. Subsequent work by the same group [33] argues for the combined contribution of both candidate mechanisms. Chan and Hudspeth performed a series of experiments [3–5] on an excised segment of the cochlea in order to identify the underlying active process in a simpler preparation than the intact cochlea. They reported existence of the nonlinear amplifier in an active preparation with artificial endolymph containing the N-methyl-D-glucamine (NMDG), a permeant cation that does not traverse the transduction channel [76]. Hence, they attended to disassociat the somatic effect, lending support to direct effect of HB motility on the observed nonlinearity. However, subsequent studies [20, 32, 33] questioned their interpretation of the data, arguing possibility of contribution of the somatic based amplification in that preparation.

The purpose of this study is to model the *in vitro* experiment of an excised section of the cochlea performed by Chan and Hudspeth [3–5] (we will refer to this preparation as *Chan-Hudspeth* experiment). We use a computational model together with analytic calculations in order to simulate acoustical, electrical and mechanical boundary conditions of these preparations. This study aims to test our model construction and assumptions on simulating such an important and difficult experiment.

5.2 Model Geometry and Boundary Conditions

A computational model of the *in vitro* experiment, developed by Chan and Hudspeth [3–5], is built to study the OoC mechanics in a small exposed segment of the cochlea. A schematic of the experimental configuration and the simulation model are illustrated in Fig. 5.1.

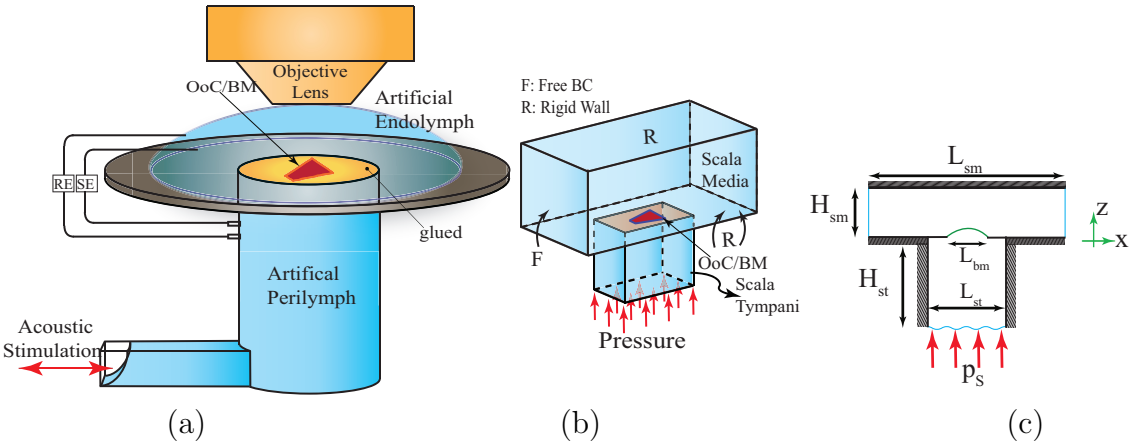

Figure 5.1: The experimental setup [3–5] and simulation; (a) *in vitro* cochlear preparation (not to scale). The apical and basal aspects of the organ of Corti were immersed in artificial endolymph and artificial perilymph, respectively. Pairs of recording electrodes (RE) and stimulating electrodes (SE) measured microphonic potentials and provided transepithelial electrical stimuli. Acoustic stimuli from an earphone (red arrow) were delivered to the basilar membrane through the fluid filled lower compartment. (b) The computational simulation of the cochlear segment experiment. The segment was stimulated through the pressure boundary condition on the bottom side of the fluid (red arrows). Two boxes located on the top and bottom of the OoC, simulated scala tympani and scala media, respectively. Boundary conditions were set as rigid wall (R) or pressure free (F) on each face, according to the experiment configuration as discussed in the text. (c) Longitudinal cross section of the model.

In the experiment, a roughly 700 μm segment of the cochlea was excised from the middle turn of the Mongolian gerbil and mounted in a two compartment recording chamber. A perpendicular transection was applied to the main axis of the cochlea between the basal and middle turns. This bony portion of this small segment of the cochlea was affixed atop a 1.5 mm hole in a 12.5 mm circular plastic disk. The lower compartment was comprised of two sections. The first was a horizontal channel 15 mm long, 1.3 mm by 0.8 mm in cross-section. This horizontal channel connected to the curved surface of cylindrical segment, 1.8 mm in diameter and 1 mm high. Artificial endolymph and perilymph surrounded the cochlear partition from the apical and basal surfaces, respectively (see Fig. 5.1a). The upper and lower compartments were connected through an electrical circuit and a D.C. transepithelial potential was applied to preserve activity. Acoustical stimuli for a range of intensities and frequencies were applied through the lower compartment and movement of the OoC components (*i.e.,* BM, TM and inner hair cell's HB) were measured at various positions across their radial dimension. For the BM measurement [4] the preparation was mounted with its apical end down to allow access to the basilar membrane. In this paper we simulate the configuration used for the TM and HB movement measurements; the apical and basal aspects of the OoC are immersed in artificial endolymph (AE) and artificial perilymph (AP), respectively.

Figures 5.1(b and c) illustrate our three dimensional mathematical model and boundary conditions corresponding to the experiment configuration. Our model is simplified, yet still retains the essential physics of the experimental configuration. The scala tympani and scala media in Fig. 5.1-b are modeled as two chambers, maintaining the fluid volume inside the lower and upper experimental compartments, respectively. The exact geometry of the ST configuration encompasses two channels that are simplified to a single channel in our model (the fluid dynamics of the two configurations are compared in Discussion section). In Table 5.1 the baseline model dimensions are

Table 5.1: Geometrical dimensions of the model corresponding to the Chan-Hudspeth experiment set up. The model dimensions are chosen such that the fluid volume inside the scala tympani and media match, respectively, the reported volume of the fluid in the bottom compartment (2-5 μL) and droplet on top ($600\mu L$)

Property	Description	Value (mm)
L_{st}	scala tympani length	1.8
H_{st}	scala tympani height	2
W_{st}	scala tympani width	1.4
L_{sm}	scala media length	2.5
H_{sm}	scala media height	2.5
W_{sm}	scala media width	11

given. The length (L), width (W), and height (H) represent the x, y, and z dimensions respectively (see Fig. 5.1(c), with the y-direction coming into the page) and the subscripts refer to the two scalae. The domain of the ST occupies the region for $-H_{st} < z < 0$ while the scala media (SM) occupies the region $0 < z < H_{sm}$. The fluid pressure and velocity at $z = 0$ were coupled to our structural model of the OoC and BM over the flexible portion and rigid boundary conditions elsewhere on that plane. In the ST, the surfaces normal to the x and y directions are rigid, while at $z = -H_{st}$ a known external pressure was applied. In the SM, the water-immersion objective lens, located on top of the upper compartment, constrains the SM fluid, hence, that entire surface ($z = H_{sm}$) was modeled as a rigid wall boundary condition. The pressure release (free) condition on the endolymphatic droplet of the experimental configuration is represented by the free (pressure zero) boundary conditions on the x-normal faces in the SM.

5.3 Linear Model Responses

Throughout entire paper, the segment length and pressure stimuli for the reported plots are, respectively, $L_{bm} = 700\ \mu m$ and $p_s = 67$ dB sound pressure level (SPL) relative to 20 μPa, unless noted otherwise. The parameters are set to account for a

segment excised from the apical part of the cochlea; the properties at the segment center match those of an intact cochlea at $x_0 = 9.5\ mm$. As in the Chan-Hudspeth experiment, acoustic stimuli are applied to the base of the fluid in the ST.

5.3.1 Mechanical responses of the OoC to acoustic stimulation

Our FEM model is tested for quantitative comparison of the segment frequency response with the experimental data. The experimental data is from Fig. 5d of [3] where the TM vertical movement is recorded at the CF of the preparation for passive (with the transepithelial potential turned off) and active preparations. Our passive model prediction of the TM displacement is compared with the experimental data of a passive preparation in Fig. 5.2a. We chose a location where the resonance frequency of the model and the experiment match and then proceed to make a level comparison between the two. It is observed that our model prediction is close to the experimental data, however they are not exactly the same. In addition to the passive configurations we used our linear model to predict the measured nonlinear (active) responses by altering the MET channel sensitivity as SPL varies. Figure 5.2b compares the experiment and simulation results; the MET channel sensitivities that we used for each stimulation are denoted in the plot.

5.3.2 Adding fluid in the ST decreases the segment resonance frequency systematically

In the Chan-Hudspeth experiment [3] it is shown that increasing the fluid mass inside the lower compartment gives rise to a linear increase on inverse square of the system natural frequency. Figure 5.3 illustrates the experimental data together with our simulation results. In order to make a quantitative comparison with the experimental measurements, the FEM model for this simulation includes the cross section change in the ST compartment (see section 5.3.4) . It is observed that our

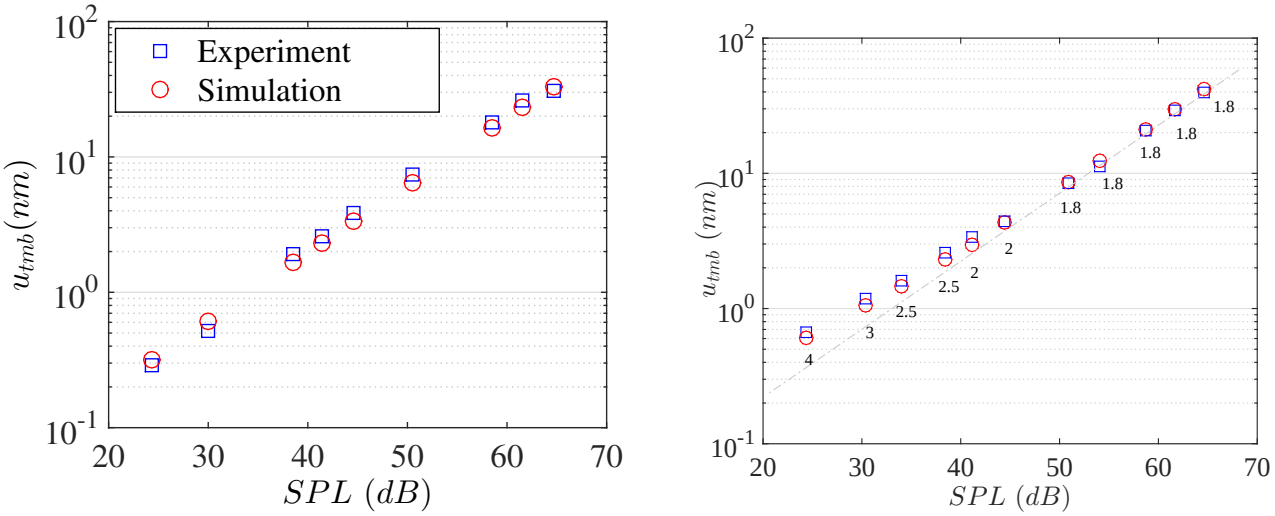

Figure 5.2: Comparing the TM vertical displacement of the experiment and simulation for a range of SPLs. The experimental data are from Fig. 5d of [3] and in the model $x_0 = 11.7\ mm$ (a) The case where the transepithelial potential is turned off and the corresponding passive model ($\mu = 0$) (b) the active experiment (with NMDG) and simulation; in order to match the experimental nonlinear data, the MET channel sensitivity of the model (μ) is decreased as the SPL increases; corresponding values are denoted next to the data of each simulation. The power-law slope of the TM response diverged from linearity (dashed gray line) at low stimulus levels.

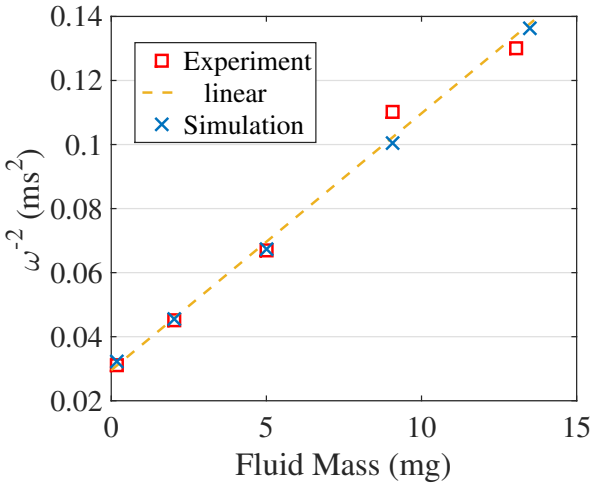

Figure 5.3: The inverse square of the HB resonance frequency increases linearly with fluid mass inside the ST compartment. Our simulation predicts the central characteristic of the experimental data (Fig. 2-e of [3]).

model predicts the experimetnal data, precisely.

The variation of the BM resonance frequency with changing the lower and upper compartments fluid height of the simplified configuration (ST single channel) are presented in Table 5.2 . It is observed that for fixed H_{sm}, increasing the fluid height in the lower channel reduces the resonance frequency, systematically. Moreover, the effect of increasing H_{sm} saturates at 500 μm for $H_{st} = 200$ μm, after which added fluid has little effect. Both of these results match with those of Chan and Hudspeth [3, 4], indicating that our modeling simplifications have captured the macroscopic fluid dynamical boundary conditions, qualitatively.

5.3.3 Traveling waves can exist on small segments of the cochlea

Sound-evoked vibrations transmitted into the mammalian cochlea produce traveling waves along the BM. This phenomenon first was explored by Von Békésy [77] and later *in vivo* by Ren [78]. The traveling wave on BM and TM, are shown to have a significant effect on the stimulation of the mechanosensory receptors of the OoC [69]. However, the precise interplay between the cochlear active process and

Table 5.2: The BM response frequency for various scala tympani and media heights . The resonance frequency decreases with an increase in the scala tympani height, while it is insensitive to the volume (mass) of fluid in the upper compartment for $H_{sm} > 200\ \mu m$.

ST Fluid (H_{sm}=250μm)		SM Fluid (H_{st}=200μm)	
$H_{st}(\mu m)$	$\omega_{res}(Hz)$	$H_{sm}(\mu m)$	$\omega_{res}(Hz)$
200	1235	200	827
300	1215	500	915
500	1195	1500	918
1000	1144	2500	918
1500	1104		
2000	1064		
2500	1034		

traveling wave propagation is not well understood. Avoiding the traveling wave in an active cochlear preparation facilitates exploring the relative contribution of HB active motility and OHC electromotility to the response in a more controlled manner, even though the setting is not the natural, biological one. This idea has been examined in the Chan-Hudspeth experiment on a small excised section of the cochlea. Although one reason for using the small segment was to avoid traveling wave, some experimental preparations [5] showed phase differences of 0.9 radians over the $700\mu m$ length, indicating the presence of a traveling wave component. In order to test the prediction capabilities of our model, we investigate existence of the traveling wave in this experiment by means of simulation. Next, we explore the conditions under which traveling waves may be developed even with such a short cochlear segment.

The activity level of the system (as embodied by the quantity μ which varies from 0 (passive) to 1 (stability boundary) is varied by altering the MET channel sensitivity and propagation of the traveling wave is investigated by computing phase accumulation along the segment. The cochlear activity in this study is generated by the outer hair cells somatic electromotility. The BM displacements along the cochlear segment for a range of activity levels are illustrated in Fig. 5.4a. Increasing

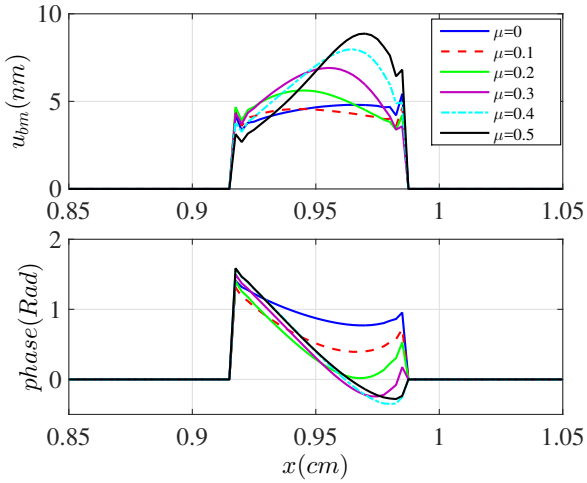

Figure 5.4: The BM displacement under acoustical stimulation with frequency equal to the CF of the segment (freq = 0.9 kHz) for different MET channel sensitivities (varied by μ coefficient; $\mu = 0$ represents the passive preparation and $\mu = 1$ is Hopf point where increasing activity level beyond that causes instability). The amount of phase accumulation increases with increasing MET channel sensitivity.

activity gives rise to a larger phase accumulation along the cochlea. Hence, we predict occurrence of an activity dependent traveling wave, even for very small segments of the cochlea (a few wave lengths long). The BM phase lags increasingly with distance from the basal end (except at the apical end which we attribute that to presence of a backward reflected wave). We note that even for the passive case ($\mu = 0$), a small phase lag is predicted which is related to variation of the structural properties (such as stiffness) along the segment. Comparing the gerbil and guinea pig models (Fig. 5.5) reveals that that phase accumulation is greater in the gerbil than the guinea pig; e.g., for $\mu = 0.5$, phase lags for the gerbil and guinea pig are 1.86 and 1.07 radian, respectively. The phase accumulates more rapidly in the gerbil since the frequency mapping is more spatially compressed compared to the guinea pig. Hudspeth and Chan [5] reported a phase difference of about 0.94 radian between the apical and basal end of the exposed segment, under acoustical stimulation. This phase lag matches our simulation results with $\mu = 0.1$, as indicated in Fig. 5.4a.

In addition to the MET channel sensitivity, the length of the exposed segment

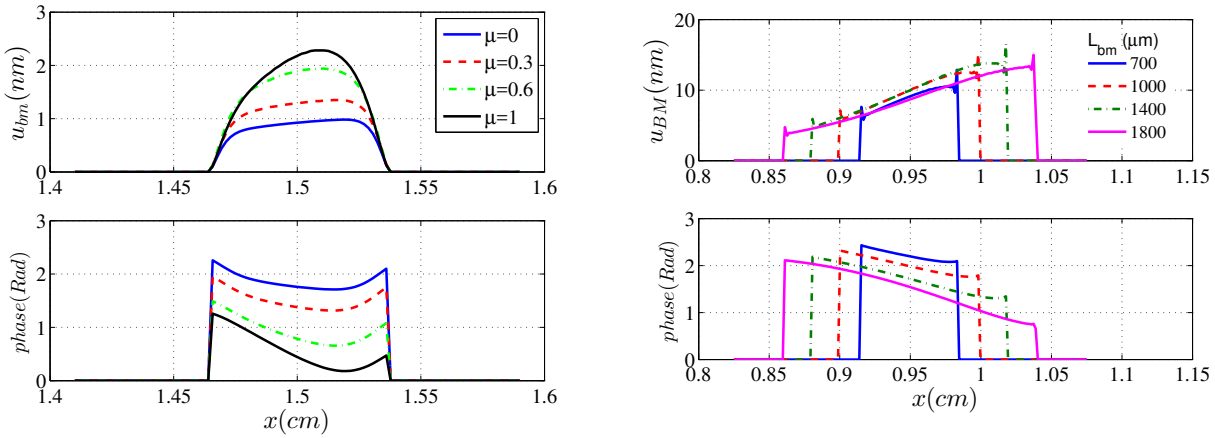

(a) (b)

Figure 5.5: The BM displacement for the cochlear segments with different lengths (L_{bm}). Larger phase accumulation (traveling wave) occurs for longer segments; $freq =$ 0.9 kHz, $\mu = 0.5$. (a) gerbil (b) guinea pig

affects phase lag along the segment. Increasing the BM length, gives rise to a larger phase lag along the segment (results not shown). Therefore, in order to avoid traveling wave in an *in vitro* experimental set up, length of the segment should be very short. However, it is limited by technical difficulties associated with response measurements.

5.3.4 Fluid dynamics of the experimental setup

The experimental configuration in the lower compartment encompasses two sections; a horizontal channel connected to a cylindrical segment underneath the cochlear partition. For the sake of simplicity of mathematical calculations, we have combined the two lower compartments into a single chamber. In this section we compare the fluid dynamics of the two geometries by using our FEM model. The configurations are illustrated in Fig.5.6; they are labeled as FEM1 (left panel) and FEM2 (right panel) for models with 1 and 2 channels in the ST compartment, respectively. Figure 5.6 demonstrates the fluid pressure profile inside the channels. The acoustical pressure is applied from the bottom part of the ST and pressure release boundary conditions are considered for the top faces of the SM compartments. The geometrical dimensions are

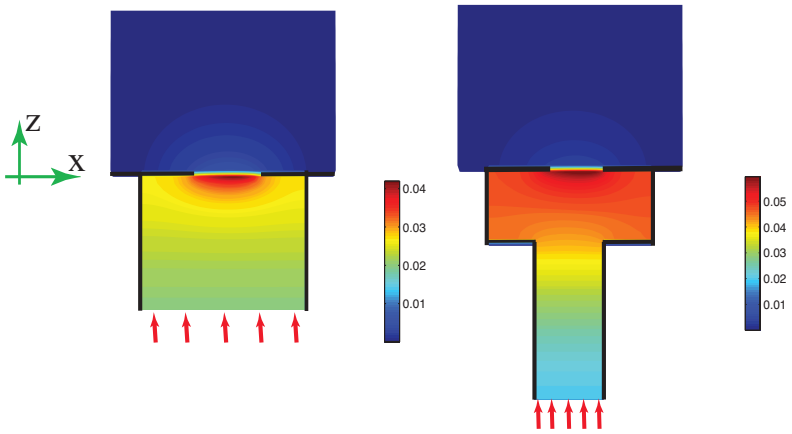

Figure 5.6: Fluid pressure profile (Pa unit) in response to a 60 dB SPL acoustical excitation with frequency equal to the CF of the segment applied at the bottom of the lower compartment; the total fluid mass is the same (5 mg) for the two ST configurations: (a) Single channel; (b) 2 channels.

set such that the amount of fluid in both configurations are the same. It is observed that the fluid dynamics are qualitatively similar for the two configurations: uniform cross section pressure far from the cochlear segment and prominent near field effect close to the segment; however, the pressure amplitude on the BM is larger for the FEM2 model.

5.3.5 Fluid loading added mass on the OoC

The macroscopic fluid boundary conditions of the setup influence the fluid added mass to the OoC and, consequently, the resonance frequency of the cochlear segment. In order to explore this effect further, the lumped fluid added mass to the BM is computed using our FEM matrix formulation Eq. 1.5 as:

$$M_{fl}^{lump-FEM} = \rho \bar{U}^T Q_{fs} K_f^{-1} Q_{sf} \bar{U} \tag{5.1}$$

where ρ denotes the fluid density and the displacement vector ($\bar{U}$) is the normalized solution of the BM response for a given frequency. The distributed added mass is pre

and post multiplied by the displacement vector in order to lump the added mass by integrating out its spacial dependency. The K_f is the dynamical stiffness matrix of the fluid and Q_{fs} and Q_{sf} correspond to fluid-structure coupling at the BM (see Eq. 1.5). The superscripts " T " and "-1", denote transpose and inverse of the corresponding matrix, respectively. The results are shown in Fig.5.7 (green curves). The fluid added mass is decomposed of two components: the near field and far field [79]. The near filed component is generated by the near field pressure close to the OoC which decays rapidly away from the cochlear segment and the far field component is due to the pressure that is uniform across the cross section of the chamber (see Fig.5.6).

The far field component can be well described using the simple 1D control volume analysis. A schematic of the experimental configuration, with the horizontal channel rotated to the vertical position, is pictured in (Fig. 5.8a). In the control volume analysis [80] we have assumed that the cochlear partition (CP) interacts with an incompressible, inviscid fluid whose pressure profile $P(z)$ varies along the length of the duct but is constant in each cross section and that the pressure in the SM is negligible as is mass of CP. A closer inspection of pressure contours obtained from our FEM model (Fig. 5.6) shows that our assumption of a constant pressure contour in each cross section is largely true except in the near field of the BM where that assumption fails (we will see this has a dramatic effect on our estimation of the added mass). Our assumption that the pressure in the SM is much smaller than that in the ST is validated by these simulations ($\sim$1/10 in amplitude). This pressure difference also gives rise to a much smaller fluid loading mass in the SM side comparing to that of the ST ($\sim$1/100); justifying neglecting the SM fluid mass in our simple model. Under these assumptions, the resonance frequency of the segment is approximated as:

$$\omega_{res} = \sqrt{\frac{K_{cp}^{vol} S_{st}}{\rho H}} \tag{5.2}$$

where $K^{vol} = P/U^{vol}$ is the volumetric or acoustical stiffness (see [81]) and $U^{vol} = \int_S uds$ is the volume displacement which is constant along the height. Equation 5.2 predicts that the far field volumetric added mass ($M_{fl}^{vol-1d} = \rho H_{st}/S_{st}$) is simply proportional to the ratio of the height to the cross section area of the duct. Furthermore this equation shows that the resonance frequency decreases with increasing fluid column height (as in the experiment and predicted by three dimensional fluid dynamical simulations (see Fig. 5.3)). Somewhat counterintuitively, the Eq. 5.2 predicts that the resonance frequency increases with increasing channel width and we validated this prediction using 3D simulations (not shown); hence the resonance frequency does not equal the square root of the quotient of the stiffness of the partition and the *total* fluid mass. Note that Eq. 5.2 is different from the equations given in [3, 4].

The 1D control volume analysis can only count for the near filed added mass not the far field component. In Fig. 5.7 the near field added masses are estimated by subtracting the far field added mass from the total FEM calculated added masses (Eq. 5.1). This plot illustrates the near field and far field added mass components for the FEM1 and FEM2 geometries, introduced in Fig.5.6. It is shown that the far field added masses are significantly different for the two configurations; however, the near field components are very similar. Moreover, it is observed that the far field components for both configurations increase by an increase in the ST fluid mass (through increasing the lower channels heights) while the near field added masses are nearly insensitive to that; this can also be observed from our closed form expression of the added mass (Eq. 5.19) in which the hyperbolic tangent function limits dependency of the near field component on the channel height.

5.3.6 Control volume analysis

The control volume analysis [80] is utilized to calculate the resonance frequency of the simplified 1D model of the Chan-Hudspeth experiment, demonstrated in Fig. 5.8.

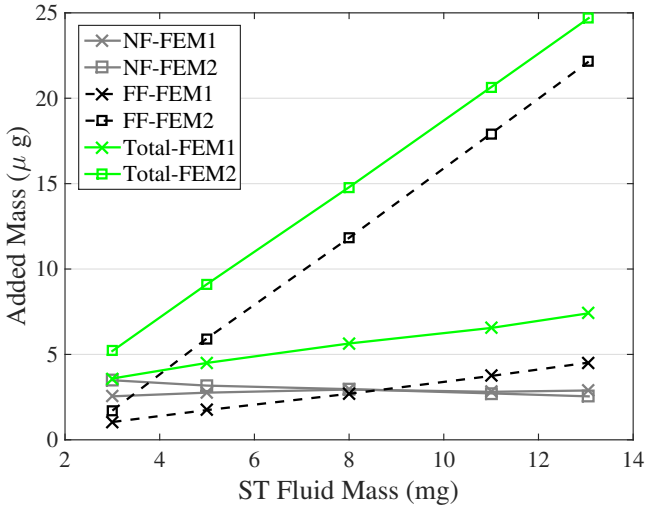

Figure 5.7: The fluid added masses to the BM and their near/far field components for the FEM1 and FEM2 models, illustrated in Fig. 5.6. The total added masses (green curves) and the far field (FF) components are calculated, respectively, from the FEM formulation (Eq .5.1) and the control volume analysis. The near field (NF) components then are estimated by subtracting the far field component from the total added mass.

The conservation of the momentum for the selected control volume results in:

$$P_{st}S_{st} - P_{bm}S_{ch} + P_{ch}(S_{ch} - S_{st}) = -\rho\omega^2 U_{bm}^{vol}(d+h) \tag{5.3}$$

where the S_{ch} and S_{st} are ,respectively, the area of the fluid chamber just below the BM and the area of acoustic stimulation where the pressure P_{st} is applied to the fluid on the bottom of the channel. A separate control volume for the chamber below BM gives rise to:

$$P_{ch}S_{ch} - P_{bm}S_{ch} = -\rho\omega^2 U_{bm}^{vol} h \tag{5.4}$$

Using the Laplace equation for the inviscid fluid dynamics together with the divergence theorem, one can show conservation of the volumetric displacement (velocity):

$$U_{st}^{vol} = U_{bm}^{vol} \tag{5.5}$$

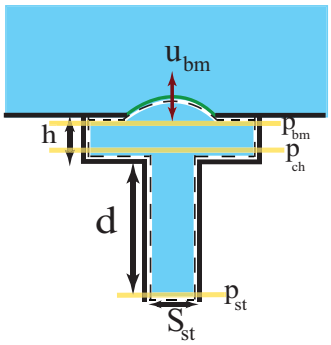

Figure 5.8: The 1D control volume model of the experiment; the lower (narrow) part represents the long horizontal channel in Fig. 5.1. Pressures for three cross sections are labeled in the figure.

Moreover, the fluid pressure below the BM (P_{bm}) can be expressed as multiplication of the cochlear partition volumetric stiffness and the BM volumetric displacements:

$$P_{bm} = K_{cp}^{vol} U_{bm}^{vol} \tag{5.6}$$

Plugging Eqs.5.5 and 5.6 into 5.3 and 5.4, the resonance frequency of the system is derived as:

$$\omega_{res} = \sqrt{\frac{K_{cp}^{vol} S_{st}}{\rho(d + hS_{st}/S_{ch})}} \tag{5.7}$$

In the simplified configuration (single ST channel), we use the case where $S_{st} = S_{ch}$ and the channel height is H:

$$\omega_{res} = \sqrt{\frac{K_{cp}^{vol} S_{st}}{\rho H}} \tag{5.8}$$

5.3.7 Estimation of the cochlear partition effective stiffness from the OoC frequency response

Analyzing the frequency response of the cochlear segment under acoustical stimulation while varying the fluid loading provides us with a means to estimate stiffness of the partition. Stiffness is not a material property, but rather depends on the boundary conditions, geometry, and forcing of the electro-elastic-acoustic system. In this section we show how to use the experimental results to estimate the overall partition volumetric stiffness.

In order to estimate the volumetric (acoustic) stiffness of the cochlear partition, we need not, however, compute the exact added mass for the experimental configuration. We need only have an estimate of the change in the acoustical mass. Although the 1D model incorrectly computes the added mass, when the height is large ($H_{st} > 1mm$) our analytic expression for the variation of the volumetric added mass (ΔM_{fl}^{vol}) of the 3D model asymptotes to the 1D model, $\rho \Delta H_{st}/S_{st}$ because the nonlinear summed terms in Eq. 5.21 reach a limiting value and remain constant as H_{st} increases. Hence the slope of the ω_{res}^{-2} versus the 1D fluid mass yields the inverse of the volumetric stiffness. It is important to estimate the resonance frequency as the peak of the frequency response of the *velocity* rather than displacement to avoid the confounding effect of the changing damping ratio with mass loading (even if the damping itself remains constant).

Using the results predicted by our 3D FEM model as an experiment data (*i.e.,* we did not assume a velocity profile but rather computed it, see Fig. 5.11), we tested this method by comparing our estimation of the volumetric stiffness to the known value of our model. Since we only need the variation of the added mass, the simplified FEM1 configuration can be used to calculate the CP stiffness. Panel (a) of Fig. 5.9 illustrates the square inverse of the frequency corresponding to the peak of BM velocity-frequency response (obtained from FEM simulation) as a function of the

fluid volumetric mass, calculated from two models. The slope of the curves in this figure represents the inverse of the BM volumetric stiffness, as illustrated in panel (b). In this plot the OoC volumetric stiffnesses approximated by the two models (1D and 3D) is shown to converge to a value which we have verified to be the same as exact value of the volumetric stiffness calculated by the FEM model ($K^{vol}_{exact} = 1.09 \times 10^{14}\ N \cdot m^{-5}$). We then applied this method to compute the volumetric stiffness of the experimental data from the Chan-Hudspeth experiment [3] and found it to be $1.9 \times 10^{14}\ N \cdot m^{-5}$.

While the volumetric stiffness is a direct measured value of the method, the point stiffness (more commonly measured) will depend on a model. If we approximate the BM deflection by a strongly orthotropic plate model (Eq. 5.17) with simply supported boundary conditions, and consider the relationship between volumetric and point stiffnesses [82] of the same volumetric stiffness we obtain a point stiffness of 0.06 N/m for the center of the cochlear segment, while the model exact point stiffness of this location ($x = 7.5$ mm from the stapes) is calculated 0.056 N/m. Furthermore, the experimental data by [83] estimates a point stiffness of $k_{measure} = 0.08$ N/m at the same location. We note that the measured point stiffness depends on the radial location and load [82–84]; hence the point stiffness values reported by different investigators does vary.

We used our method for evaluating the stiffness of the cochlear partition using the same method as in Figure 5.9. Using the slope in Fig. 5.10b we find the lumped stiffness of the partition to be 0.225, 0.232, 0.234 N/m for μ equal 0.1, 0.3 and 0.5, respectively. Hence this technique predicts a stiffness that is relatively insensitive to activity. This result is consistent with the experimental data by Olson and Mountain [82], where they did not detect changes in situ between pre-mortem stiffness and stiffness measured within 1 h post-mortem.

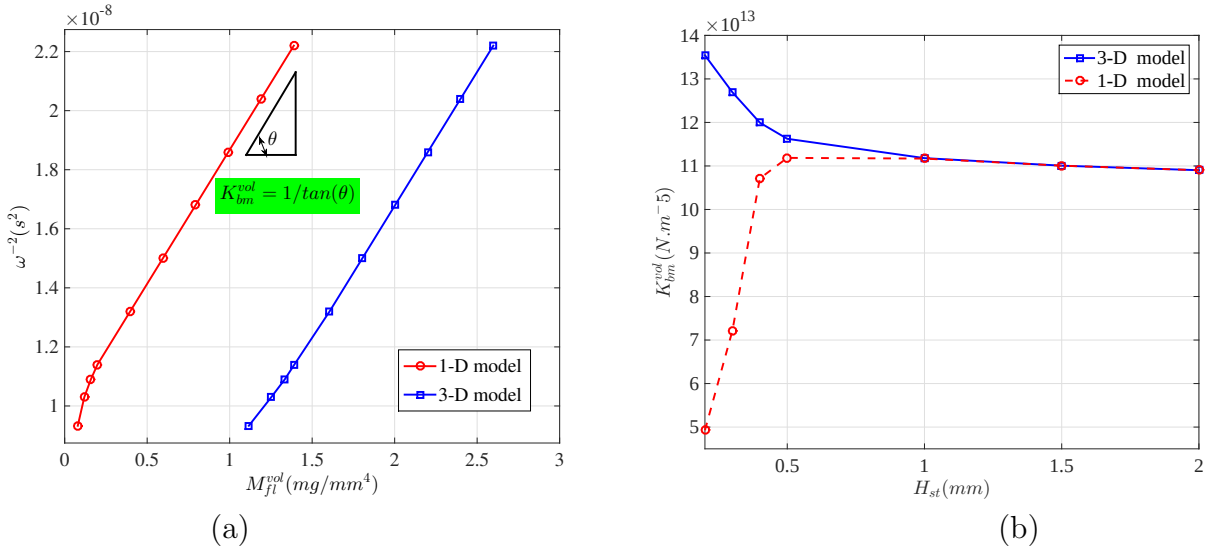

Figure 5.9: Estimation of the cochlear partition volumetric stiffness from the velocity frequency response ; (a) square inverse of the BM resonance (characteristic) frequency (from FEM simulation) versus volumetric added mass, calculated from two models: 1D volumetric (Eq. 5.2) and 3D analytical models (Eq. 5.21). (b) Volumetric stiffness calculated from inverse of slopes of curves in panel (a), assuming a simple harmonic characteristic for the cochlear segment. The OoC volumetric stiffness approximated from the two models are the same ($K^{vol}_{approx.} = 1.09 \times 10^{14}\ N.m^{-5}$) and match the exact volumetric stiffness of the segment, calculated by the FEM model ($K^{vol}_{exact} = P_{bm}/U^{vol}_{bm}$) for uniform pressure on the BM and low frequency stimulation.

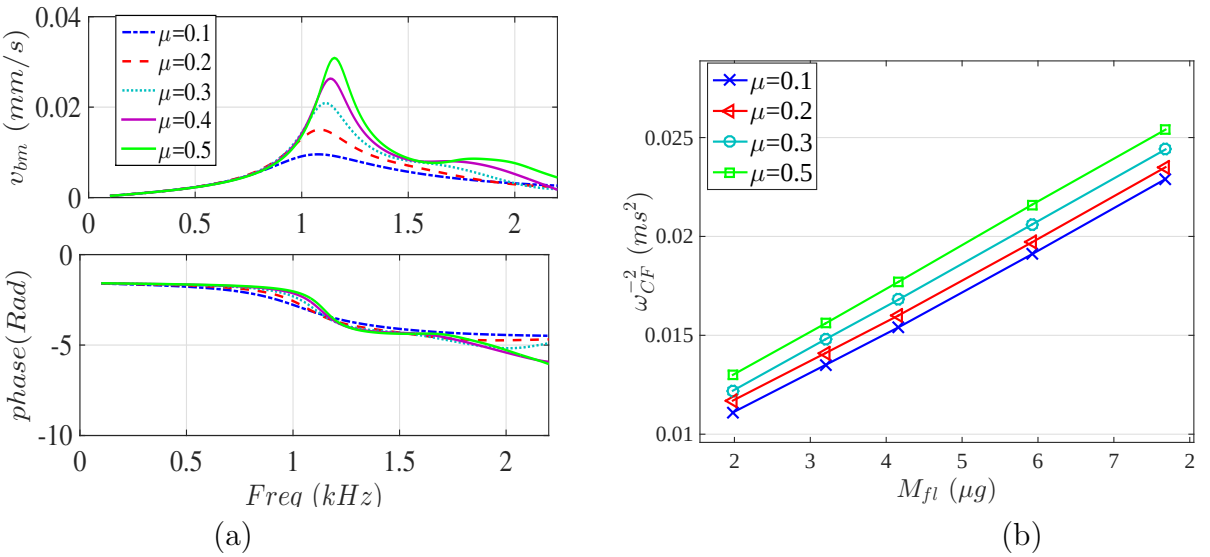

Figure 5.10: (a) Velocity frequency response for different activity levels (μ). Higher MET channel sensitivity gives rise to sharper response with larger CF (b) Inverse of the characteristic frequency with respect to the added mass for different activity levels. The added mass is calculated from the analytical model (Eq. 5.19).

5.3.8 Dynamics of the active excised cochlear segment can be represented by a lumped component model

In vivo analysis of the cochlear mechanics is greatly complicated by the presence of a traveling wave on the cochlear partition. As a result of this mode of movement, different portions of the partition are at any instant responding in quite different ways which makes it more difficult to study cochlear local dynamics. Suppressing the traveling wave along the segment, if possible, allows a simplification of the movement that all of the hair cells function more-or-less in concert and enables studying the active process. One goal of the Chan-Hudspeth configuration is to simplify the movement by encouraging a segment of the cochlear partition to resonate in a simple, second-order mode. However, in previous section we demonstrated that a simulation of this experiment discloses existence of traveling wave which its strength depends on the segment length and activity level. Hence, it is important to identify contribution of the traveling wave on the cochlear response in this preparation. To this end, we propose a lumping method to reduce the fluid dynamics into a loading added mass on the OoC. The reduced order model is called lumped component model. The lumped component model allows for adding HB motility and studying contribution of the active process (somatic electromotility and HB motility) on the cochlear amplifier, while the traveling wave is attenuated.

5.3.9 Analytical approximation of the fluid pressure and added mass

The cochlear partition is stimulated by pressure difference across the OoC. An analytical formulation of the fluid dynamics interacting with the OoC mechanics, provides us with a robust explanation of the results obtained from the computational model. By utilizing a Fourier series along the x and y directions, we approximate the pressure distribution in the fluid. This approach along with the WKB method has been developed by Steele and Taber [85] to calculate the cochlear response in a three di-

mensional model. They employed the WKB method to compute the BM wavelength which is varying spatially along the cochlea. However, compactness of the segment in our simulation, allows us to approximate the wavelength as $\lambda = \pi/L_{bm}$, by assuming a half sine wave shape for the BM displacement. The assumed BM spacial displacement together with the FEM simulation results for two different frequencies and activity levels are depicted in Fig. 5.11. Considering this simplification for the exposed short segment, the pressure distribution inside the scala tympani can be approximated as:

$$P^{st}(x,y,z,t) = \sum_{k}\sum_{j} Q^{st}_{jk}(z)\phi^{st}_{j}(y)\psi^{st}_{k}(x)e^{-i\omega t} \qquad \text{for } z = [-H_{st}, 0] \tag{5.9}$$

Moreover, The boundary condition at $z = -H_{st}$ corresponds to the acoustical pressure stimuli, p_s, in the bottom, while a linearized Euler relation satisfies the BM-fluid interaction at $z = 0$:

$$BC : \begin{cases} P^{st}\Big|_{(z=-H_{st})} = p_s e^{-i\omega t} \\ \frac{\partial P^{st}}{\partial z}\Big|_{(z=0)} = \rho\omega^2 U_{bm}\eta(y)\chi(x)e^{-i\omega t} \end{cases} \tag{5.10}$$

As depicted in Fig.5.1(c), geometrical dimensions corresponding to the scala tympani and scala media are illustrated by " st " and " sm " subscribes, respectively. Moreover, ρ and U_{bm} denote fluid density and BM maximum displacement ($u_{bm} = U_{bm}\eta(y)\chi(x)e^{-i\omega t}$), respectively. A time dependence of $e^{-i\omega t}$ is assumed, where ω is the angular frequency. Considering the rigid wall pressure boundary conditions in x and y directions (see Fig.5.1) and hinged edges for the BM, the representing functions in Eq. 5.9 have the

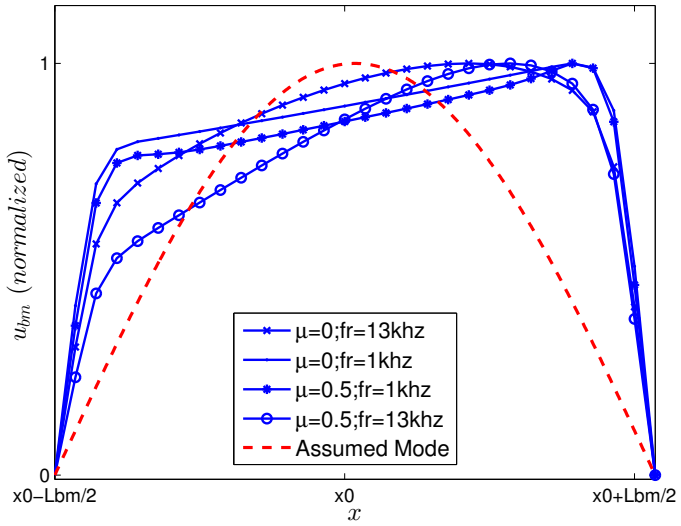

Figure 5.11: The BM displacement along the segment is approximated with a sinusoid function, $\chi(x)$. The BM displacement peaks for the numerical responses are shifted toward the apex due to the BM stiffness spacial variation.

following form:

$$\begin{aligned} \phi_j^{st}(y) &= \cos\left(\frac{j\pi(y+W_{st}/2)}{W_{st}}\right);\ \eta(y) = \sin\left(\frac{\pi(y+b/2)}{b}\right) \\ \psi_k^{st}(x) &= \cos\left(\frac{k\pi(x+L_{st}/2)}{L_{st}}\right);\ \chi(x) = \sin\left(\frac{\pi(x+L_{bm}/2)}{L_{bm}}\right) \end{aligned} \tag{5.11}$$

The functions $\phi_j^{st}(y)$ and $\psi_k^{st}(x)$ represent the pressure components corresponding to modes j and k, respectively. Taking advantage of orthogonality of the modes, we can integrate out the longitudinal and lateral modes by multiplying both sides of the BC by $\psi_K(x)$ and $\phi_J(y)$ and integrating over $(-L_{st}/2, L_{st}/2)$ and $(-W_{st}/2, W_{st}/2)$, respectively:

$$
\begin{aligned}
Q_{jk}^{st}\Big|_{z=-H_{st}} &= \begin{cases} p_s A_0^{st} B_0^{st}/(L_{st}W_{st}) & \text{j=k=0} \\ 0 & \text{otherwise} \end{cases} \\
\frac{\partial Q_{jk}^{st}}{\partial z}\Big|_{z=0} &= \frac{\rho\omega^2 U_{bm} A_j^{st} B_k^{st}}{m_j^{st} m_k^{st} L_{st} W_{st}}
\end{aligned}
\tag{5.12}
$$

where:

$$
\begin{aligned}
m_k^{st} &= \frac{1}{L_{st}} \int_{-L_{st}/2}^{L_{st}/2} \left(\psi_k^{st}\right)^2 dx; \;\; A_j^{st} = \int_{-b/2}^{b/2} \eta \phi_j^{st} dy \\
m_j^{st} &= \frac{1}{W_{st}} \int_{-W_{st}/2}^{W_{st}/2} \left(\phi_j^{st}\right)^2 dy; \;\; B_k^{st} = \int_{-L_{bm}/2}^{L_{bm}/2} \chi \psi_k^{st} dx
\end{aligned}
\tag{5.13}
$$

Note that $\chi(x)$ and $\eta(y)$ are defined in the domain of $(-L_{bm}/2, L_{bm}/2)$ and $(-b/2, b/2)$, respectively, and are zero everywhere else. Considering the Laplace equation for the inviscid and inviscous fluid on the scala tympani, we have:

$$
\nabla^2 P^{st} = 0 \tag{5.14}
$$

Next, we substitute pressure expansion from Eq.5.9 into Eq. 5.14 :

$$
\frac{d^2 Q_{jk}^{st}}{dz^2} - \alpha_{jk}^2 Q_{jk}^{st} = 0 \tag{5.15}
$$

where, ${\alpha_{jk}^{st}}^2 = (k\pi/L_{st})^2 + (j\pi/W_{st})^2$. This second order differential equation together with corresponding boundary condition (Eq.5.12) has an exponential solution for all j's and k's except when, $\alpha_{jk} = 0$ in which then the solution is a linear polynomial:

$$Q_{jk}^{st}(z) = \begin{cases} \frac{\rho\omega^2 U_{bm} A_0 B_0}{W_{st} L_{st}} (z + H_{st}) + p_s & k = j = 0 \\ \frac{\rho\omega^2 U_{bm} A_j^{st} B_k^{st}}{\alpha_{jk}^{st} W_{st} L_{st} m_j^{st} m_k^{st}} \frac{\sinh\left[\alpha_{jk}^{st}(z+H_{st})\right]}{\cosh(\alpha_{jk}^{st} H_{st})} & \text{otherwise} \end{cases} \tag{5.16}$$

where $A_0 = 2b/\pi$ and $B_0 = 2L_{bm}/\pi$. Finally, we plug Eq. 5.16 into Eq. 5.9 and obtain pressure distribution inside the scala tympani. A similar process is performed for the scala media compartment to calculate P^{sm}. Appropriately with the given circumstance, we need to redefine $\psi_k^{sm}(x) = \sin\left(\frac{k\pi(x+L_{sm}/2)}{L_{sm}}\right)$, thus indicating that the pressure boundary condition for the scala media compartment is different than the scala tympani (see Fig. 5.1).

Consequently, the pressure difference between two sides of the BM, produces a harmonic force to the BM which appears in the right hand side of the BM equation of motion (plate model):

$$D_{xx}\frac{\partial^4 u_{bm}}{\partial x^4} + 2(D_{xy}+2D_{sh})\frac{\partial^4 u_{bm}}{\partial x^2 \partial y^2} + D_{yy}\frac{\partial^4 u_{bm}}{\partial y^4} - i\omega C_{bm} u_{bm} - M_{bm}\omega^2 u_{bm} = \left[P^{st} - P^{sm}\right]_{(x,y,0,t)} \tag{5.17}$$

where C_{bm} is the BM viscous damping per unit area and M_{bm} is the mass of the BM per unit area. D_{xx}, D_{yy} ,D_{xy} and D_s are the orthotropic plate bending stiffnesses of the BM mode. Locally reacting model of the BM corresponds to $D_{xx} = D_{xy} = D_s = 0$. Figure. 5.12 exhibits precision of our method by comparing the pressure distribution along the z axis (Eq. 5.9) with the FEM results. An excellent agreement between the two approaches, ratifies the assumed structural model consideration in the analytical calculation.

Next step, we compute the segment lumped model elements by integrating out the x and y components from Eq. 5.17 to get:

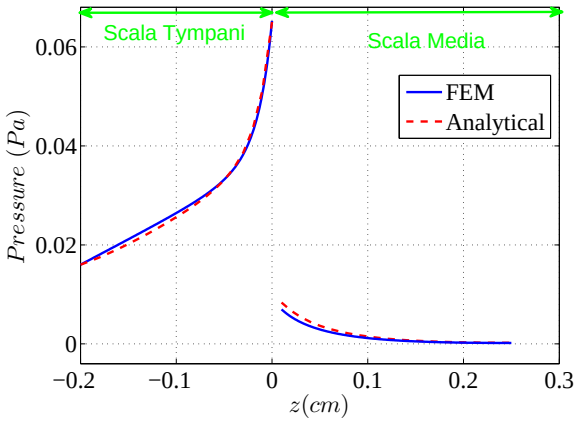

Figure 5.12: The 3D analytical model (Eq. 5.9) reproduces the pressure dependency predicted by the FEM analysis. In analytical calculation, the BM displacement is considered the same as the FEM simulation result.

$$\left(K_{bm}^{lump} - i\omega C_{bm}^{lump} - M_{bm}^{lump}\omega^2\right) U_{bm} = F_{bm}^{lump} \tag{5.18}$$

where $M_{bm}^{lump} = M_{fl}^{lump-analytical} + M_{bm}I$ and $K_{bm}^{lump} = \pi^4 \left(D_{xx}/L_{bm}^4 + 2\left(D_{xy} + 2D_{sh}\right)/b^2 L_{bm}^2 + D_{yy}/b^4\right.$
$C_{bm}^{lump} = C_{bm}I$, $F_{bm}^{lump} = p_s \int_{-L_{bm}/2}^{L_{bm}/2} \int_{-b/2}^{b/2} \eta(y)\chi(x)dydx$ and $I = \int_{-L_{bm}/2}^{L_{bm}/2} \int_{-b/2}^{b/2} \eta(y)^2\chi(x)^2 dydx$.
In this equation, $M_{fl}^{lump-analytical}$ represents the effective fluid lumped added mass to the BM and has the following form:

$$\begin{aligned} M_{fl}^{lump-analytical} = \sum_k \sum_j [& \frac{\rho \left(A_j^{st} B_k^{st}\right)^2}{\alpha_{jk}^{st} W_{st} L_{st} m_j^{st} m_k^{st}} \tanh\left(\alpha_{jk}^{st} H_{st}\right) + \\ & \frac{2\rho \left(A_j^{sm} B_k^{sm}\right)^2}{\alpha_{jk}^{sm} W_{sm} L_{sm} m_j^{sm}} \frac{exp(-2\alpha_{jk}^{sm} H_{sm}) + 1}{exp\left(-2\alpha_{jk}^{sm} H_{sm}\right) - 1}] + \frac{16 H_{st} \rho b^2 L_{bm}^2}{\pi^4 W_{st} L_{st}} \end{aligned} \tag{5.19}$$

This formula involves the near field (summation terms) and 1D volumetric (last term) contributions on the added mass calculation. The number of modes necessary for convergence is determined by the summation limits $j, k = 0, 1, 2, ...$ (except $j = k = 0$, which is separated out in the last term). Number of modes as low as 10 for each x

and y components is enough for convergence in our simulations. One can compute the acoustical/volumetric added mass by dividing Eq. 5.19 by the BM mode shapes:

$$M_{fl}^{vol-analytical} = \frac{M_{fl}^{lump-analytical}}{(16b^2L_{bm}^2/\pi^4)} \tag{5.20}$$

The analytic added mass formulations are utilized in the paper to calculate the segment effective stiffness and interpret the experimental/computational results.

This formula involves the near field (summation terms) and 1D volumetric (last term) contributions on the added mass calculation. The number of modes necessary for convergence is determined by the summation limits $j, k = 0, 1, 2, ...$ (except $j = k = 0$, which is separated out in the last term). Number of modes as low as 10 for each x and y components is enough for convergence in our simulations. One can compute the acoustical/volumetric added mass by dividing Eq. 5.19 by the BM mode shapes:

$$M_{fl}^{vol-analytical} = \frac{M_{fl}^{lump-analytical}}{(16b^2L_{bm}^2/\pi^4)} \tag{5.21}$$

5.4 Nonlinear Reduced-Order Model

The Chan and Hudspeth experiments are known as important evidence that support contribution of the HB motility on the cochlear amplification in mammals. In previous sections we developed a computational model of these experiments and showed that our linear model of the electrical, mechanical, and acoustical boundary conditions of the configuration is able to replicate some of the experimental results. However, in order to identify the root source of the nonlinearities seen in the Chan-Hudspeth experiment, the contribution of the somatic motility, HB motility, and nonlinearity of the MET channels to the overall response must be modeled and analyzed. To this end we build a nonlinear model of the Chan and Hudspeth experiments [3–5] to determine the relative contribution of the active mechanisms on

the cochlear amplifier under acoustical and electrical excitations. A reduced-order nonlinear model is obtained through an assumed mode formulation, based on our previous FEM model [86].

The transduction current is observed to vary nonlinearly with respect to the HB deflections, which is widely hypothesized as the main source of the cochlear nonlinear behavior. Utilizing a first-order Boltzmann function of the HB deflection (u_{hb}), the MET current flowing through the OHC is estimated as shown in Eq. 1.1 [25] (see Fig. 1.3).

5.4.1 Structural dynamics

Equation 5.17 represents the BM mechanics (plate model) with the boundary conditions associated to the Chan-Hudspeth experimental configuration. This equation can be rewritten as:

$$\frac{b}{2}\left(K_{bm}+C_{bm}\frac{d}{dt}+M_{bm}\frac{d^2}{dt^2}\right)\left\{u_{bm}(t)\chi(x)\right\}=q_{bm}(x) \tag{5.22}$$

where $q_{bm}(x)=\int_{-b/2}^{b/2}\left[P^{st}-P^{sm}\right]\eta(y)dy$ is the pressure loading per unit length on the BM and $K_{bm}=D_{xx}\frac{\partial^4}{\partial x^4}+2\pi^2/b^2\left(D_{xy}+D_{sh}\right)\frac{\partial^2}{\partial x^2}+\pi^4/b^4D_{yy}$ is the BM stiffness operator, lumped in the y direction. The BM lumped equation introduced in Eq. 5.22 is incorporated in the microstructure of the OoC which includes the TM shear (u_{tms}) and bending (u_{tmb}) displacements. The structural dynamics equation of the OoC gets the from:

$$\left\{\boldsymbol{K_s}+\boldsymbol{C_s}\frac{d}{dt}+\boldsymbol{M_s}\frac{d^2}{dt^2}\right\}\bar{\boldsymbol{u}}\chi(x)=\boldsymbol{Q_s}\bar{\boldsymbol{u}}\chi(x)=\bar{\boldsymbol{F}}_{\boldsymbol{s}} \tag{5.23}$$

Here, $\boldsymbol{K_s}$, $\boldsymbol{C_s}$ and $\boldsymbol{M_s}$ are, respectively, the structural stiffness, damping and mass matrices (3 by 3 dimensions) applied to the displacement vector $\bar{\boldsymbol{u}}=\left[u_{bm},u_{tms},u_{tmb}\right]^T$,

while the superscript "T" denotes the transpose of the corresponding vector. Moreover, $\bar{\boldsymbol{F}}_{\boldsymbol{s}} = [q_{bm}, 0, 0]^T$ is the force vector representing the external pressure loading on the OoC.

5.4.2 Electrical components

An electrical circuit model is incorporated to describe the current path inside the OoC. The circuit model in a cross section of the Chan-Hudspeth experimental configuration is illustrated in Fig. 1.2. The governing electrical equations for a cross section are driven using the Kirchhoff's laws:

$$\begin{aligned} &-\left(1/R_{sm} + 3Y_a\right)\phi_{sm} + 3Y_a\phi_{ohc} - I_{met} = 0 \\ &3Y_a\phi_{sm} - 3(Y_a + Y_m)\phi_{ohc} + 3Y_m\phi_{st} + I_{met} - I_{pz} = 0 \\ &3Y_m\phi_{ohc} - \left(1/R_{st} + 3Y_m\right)\phi_{st} + I_{pz} = 0 \end{aligned} \tag{5.24}$$

where Y_a and Y_m are admittances of the apical and basolateral portions of the OHC, respectively. The transduction current (I_{met}) and piezoelectric current (I_{pz}) are introduced in Eqs. 1.1 and 1.3, respectively. It is observed that the longitudinal current flow along the cochlea does not contribute significantly on the overall dynamics of this preparation (data not shown), thus it is not included here for the sake of simplicity. In these equations ϕ_{sm}, ϕ_{ohc} and ϕ_{st} represent the electrical voltages in the SM, intracellular OHC and ST, respectively. the voltage vector is defined as $\bar{\boldsymbol{\Phi}} = [\phi_{sm}, \phi_{ohc}, \phi_{st}]$. Using the same longitudinal mode shape for the electrical responses as the mechanical displacements ($\chi(x)$), we can write $\bar{\boldsymbol{\Phi}}(t, x) = \bar{\boldsymbol{\phi}}(t)\chi(x)$.

For the electrical stimulation experiments (section 5.5.2) an AC current is applied between the SM and ST compartments which is simulated by applying external currents (with equal amplitudes but opposite polarity) to the right hand side of the first and third equations of the Eqs. 5.24.

5.4.3 Electro-mechanical Coupling

The electrical and structural components of the OoC are linked through the mechanoelectrial properties of the OHCs (see Eqs. 1.3). Hence, the structural and electrical domains are coupled as follow:

$$\begin{bmatrix} \boldsymbol{Q_s} & \boldsymbol{Q_{se}} \\ \boldsymbol{Q_{es}} & \boldsymbol{Q_e} \end{bmatrix} \begin{bmatrix} \bar{\boldsymbol{u}}\chi(x) \\ \bar{\phi}\chi(x) \end{bmatrix} + \bar{\boldsymbol{\mathcal{N}}}(u_{hb}) = \begin{bmatrix} \bar{\boldsymbol{F}}_{\boldsymbol{s}} \\ \boldsymbol{0} \end{bmatrix} \tag{5.25}$$

where the structural and electrical sub-matrices are denoted by subscripts s and e, respectively. The sub-matrix $\boldsymbol{Q_s}$ contains the structural components as defined in Eq. 5.23, while the electrical components (Eq. 5.24) are introduced in the sub-matrix $\boldsymbol{Q_e}$. Moreover, the sub-matrices $\boldsymbol{Q_{se}}$ and $\boldsymbol{Q_{es}}$ represent the coupling between structural and electrical elements (as introduced in Eqs. 1.1 and 1.3). The nonlinear terms (stem from the MET channels) are separated into the vector $\bar{\boldsymbol{\mathcal{N}}} = [0, 0, 0, -I_{met}, I_{met}, 0]^T$.

Equation 5.25 represents the nonlinear dynamics of a cochlear segment with longitudinal coupling along the cochlea. This model can be further reduced to a lumped model by multiplying both sides of Eq. 5.25 by the assumed mode $\chi(x)$ and integrating over the segment length L_{bm}. Using the modal approximation of the fluid pressure in the x and y directions (Eq. 5.9), the first term of the force vector $\bar{\boldsymbol{F}}_{\boldsymbol{s}}$ takes the form $\int_{-L_{bm}/2}^{L_{bm}/2} q_{bm}(x)\chi(x)dx = -M_{fl}^{lump}\frac{d^2u_{bm}}{dt^2} + F_{bm}^{lump}$, where M_{fl}^{lump} (Eq. 5.19) is the fluid added mass to the BM (calculated from $Q^{st}(z,t)$) and $F_{fl}^{lump} = 4p_sL_{bm}b/\pi^2$ is the loading force to the BM due to the input pressure p_s.

The BM traveling wave along the cochlear partition is measured from the Chan-Hudspeth experiment; 4.6 mm wavelength [86] for a 700 μm segment. The short traveling wave in this preparation allows to reduce the macroscopic fluid dynamics of the configuration to a loading added mass on the BM and simplify the complex FEM model into an analytical lower-order model. Assuming a specific spatial mode

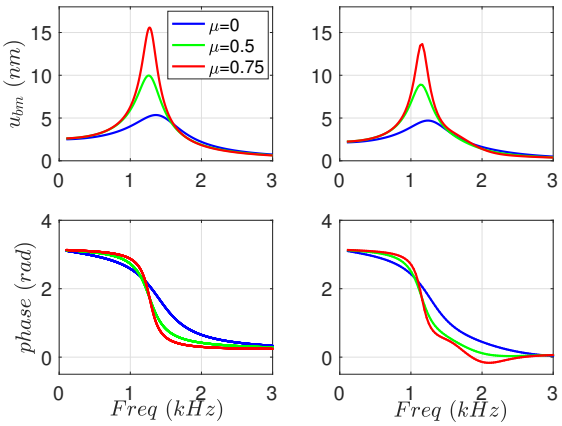

Figure 5.13: The BM frequency response (amplitude and phase) from the FEM (right) and the analytical model (left) for 60 dB SPL and various MET channel sensitivities (controlled by the scaling factor, μ). The reduced-order model represents the main characteristics of the FEM model very well.

shape (half-sinusoidal) for the electrical and mechanical responses, the longitudinal dependency of these quantities are integrated out and a lumped component model for the segment is developed. The reduced-order dynamics is much simpler in terms of interpreting the results as well as computational challenges.

5.4.4 Comparing reduced-order and FEM models

In Fig. 5.13 the BM frequency responses of the analytical reduced-order model and the FEM model are compared. Three different activity levels are simulated by varying the scaling factor μ which is defined in Eq. 1.1. It is shown that our analytical simplified model captures the dynamics of the original system (*i.e.* frequency tuning and amplification properties) very well. However, it is noted that the amplitude responses are slightly overestimated by the reduced-order model which, presumably, resulted from the added mass approximation [86].

5.5 Nonlinear Model Results

5.5.1 NMDG does not abolish somatic based amplification

In the Chan-Hudspeth experiment [3], the cochlear responses were studied under replacement of the normal K^+ rich endolymph by channel-impermeant NMDG which does not traverse the transduction channel [76]. The NMDG-based endolymph lacks the K^+ that ordinarily carries most of the transduction current. The level dependency of the cochlear responses were measured to assess the cochlear amplifier and the underlying mechanism. Acoustic pressures over a range of frequencies and intensities were applied to the basal part of the lower compartment (shown with red arrows in Fig. 5.1) and the OoC motions were measured. We have simulated this configuration as described in the section 5.4. Figure 5.14 shows the experimental data as well as the simulation results of the cochlear microphonics (CM) and HB motions for preparations with different endolymphic fluids.

Figure 5.14(a) shows the HB displacements at the resonance peaks over a range of stimulus levels; experimental data (Fig.5 of [3]) and simulation results. In this figure there are two sets of experimental data corresponding to the preparations with K^+ (square markers) or NMDG (triangle markers). Figure 5.14(a) is in log-log scale and the power-law slopes corresponding to the fitted lines to the experimental data are denoted inside the figure. The cochlear active process is level dependent; for the low SPLs the responses are nonlinear while higher SPLs show a linear input-output relation, as evidenced in the Fig. 5.14(a). Replacing K^+ rich endolymph with NMDG has decreased the nonlinearity level, changing the the power-law slopes from 0.75 to 0.85 (1 being linear). Figure 5.14(a) also shows the simulation results for the experimental data. It is observed that the experimental data of the K^+ preparation is well predicted by our model for $\mu = 0.7$. The NMDG based endolymph is simulated by reducing the MET transduction current sensitivity because only Ca^+ passes through

the transduction channels. As shown in Fig. 5.14(a), a value of $\mu = 0.3$ predicts the the NMDG effect on the MET nonlinearity very well.

Figure 5.14(b) illustrates the CM of the experimental data (right trace) and corresponding simulation results (left trace) for K^+ and NMDG based endolymphic preparations. The experimental data show that CM decreases by replacing K^+ endolymph with the NMDG. Although the model somewhat over predicts the absolute level, the relative change is well-matched. The root-mean-square (RMS) of the CMs for the preparations with K^+ endolymph and NMDG are calculated 18.6 μV and 7.8 μV, respectively; hence, NMDG causes 57.7% reduction on the CM. This drop in the CM is caused by the reduction of the transduction current due to the blockage of the MET channels by the NMDG molecules. The left panel of Fig. 5.14(b) shows the simulation results for the corresponding experiment. In this figure, as in Fig. 5.14(a), replacing normal endolymph with the NMDG is simulated by decreasing the MET sensitivity controlled by the scaling factor μ. It is shown that reducing μ from 0.7 to 0.3 gives rises to 56.8% reduction of the CM, changing the RMS from 27 μV to 11.5 μV.

5.5.2 Electrical stimulation

A sinusoidal current stimulus (30 μA) is applied across the chambers (see Fig. 5.1) and electrically evoked motions of the HBs are measured under variation of the endolympic fluid. Figure 5.15 shows the experimental data (right) next to the simulation results (left). As in the experiment, our model predicts that replacing normal endolymph with NMDG does not affect the electrically evoked motions of the HBs. As for the CM, the theory over predicts the absolute level. This could be due to the difference in the measurements locations (IHC in the experiment and OHC in our model) or the lumping process.

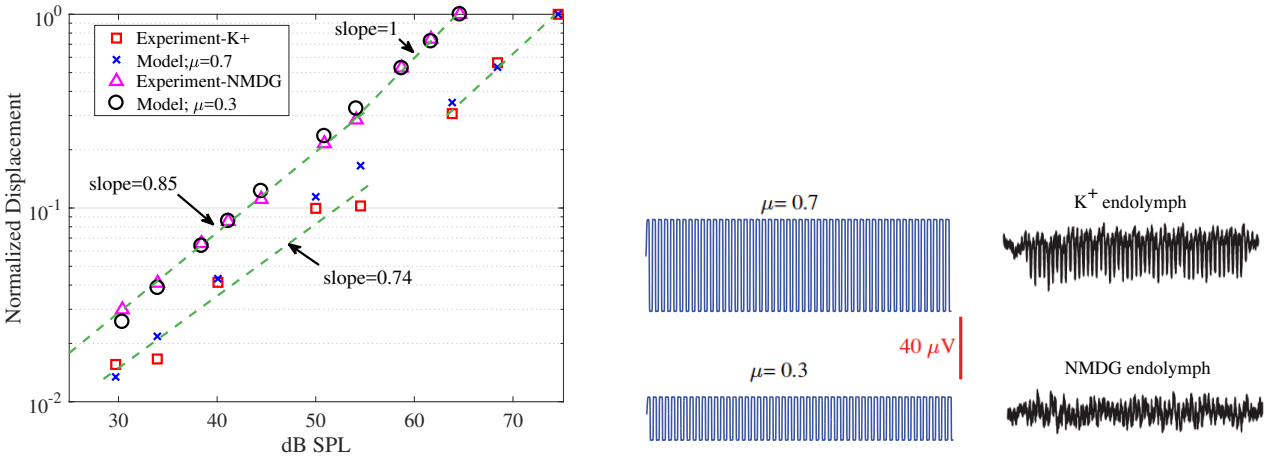

(a) (b)

Figure 5.14: The NMDG effect on the CM and compressive nonlinearity. (a) The HB displacements at the resonance peaks over a range of stimulus levels for preparations with K^+ and NMDG based endolymphs; experimental data (Fig.5 of [3]) and simulations. For visual clarity to compare the slopes (representing the nonlinearity), the data for each preparation are normalized to their relative largest amplitude (highest SPL). The power-law slopes corresponding to the curves fitted to the experimental data are denoted inside the figure (1 being linear). (b) Microphonic response to a 67 dB SPL stimulus; simulation (left) and experimental data from [3] (right). Decreasing μ from 0.7 (top trace) to 0.3 (bottom trace) causes the RMS of the CM to decrease from 27 μV to 11.5 μV that is 56.8% reduction. For the experimental data (right) the reduction is calculated 57.7% (changing from 18.6 μV to 7.8 μV). The HB motility is not incorporated in this simulation.

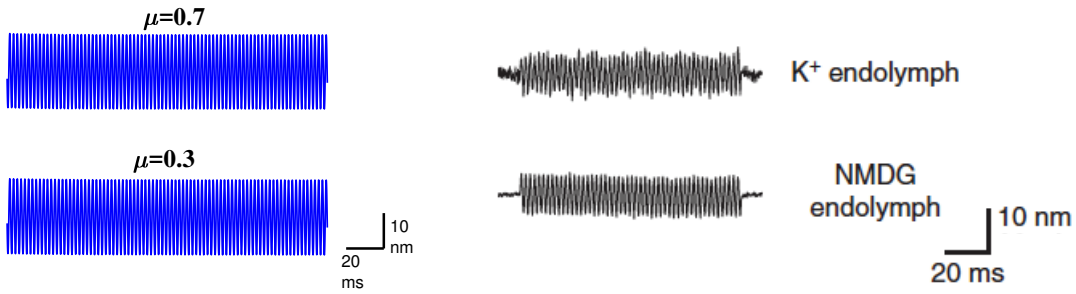

(a) (b)

Figure 5.15: The electrically evoked HB movement for preparations with normal K^+ based endolymph and NMDG. A 500-Hz sinusoidal current stimulus (30 μA peak to peak) is applied across the sensory epithelium and HB motions are presented for (a) simulation (OHC-HB) (b) experimental data from Fig. 4b of [3] (IHC-HB).

5.5.3 Hair Bundle adaptation reduces the MET sensitivity

In this section the alternative active process of HB motility (Eq. 1.4) is incorporated into the reduced-order model and interplay between the two mechanisms is explored. Figure 5.16 shows contribution of the HB adaptation on the cochlear nonlinear amplification. In this figure the normalized amplitude of the HB displacements at resonance are plotted as a function of stimulus level for simulations with and without HB adaptation. In addition, the experimental data from [3] are included for comparison. The OHC piezoelectricity (Eq. 1.3) remains the same for both simulations, while the adaptation motor is set to be stationary ($dx_a/dt = 0$) for the passive HB model (without adaptation). Two sets of parameters (Case I and Case II) are considered for the HB model as listed in Table 5.4. Each parameters set corresponds to a dynamical regimes as discussed in Chapter II. Case I parameters are physiologically valid and give rise to spontaneous oscillations for isolated HB, while Case II parameters are selected such that enhance the MET sensitivity. The MET scaling factor μ is varied for each simulation such that the dynamics is close to the Hopf point where the nonlinearity effect is maximum. As shown in Fig. 5.16(a) the HB motility diminishes the cochlear compressive nonlinearity originated from the OHC electromotility when Case I parameters are used. However, when using the Case II parameters (Fig. 5.16(b)) the HB amplitude and compressive nonlinearity increases significantly. In order to interpret these results, the action of the HB motility on the MET sensitivity is calculated as:

$$Sen = \partial I_{met}/\partial u_{hb} = \mu \Delta V^0 G^{max} C_p \left\{ 1 - \partial x_a/\partial u_{hb} \right\}, \tag{5.26}$$

where the associated parameters are defined in the Table 5.4. A time dependence of $e^{-j\omega t}$ is assumed (where ω is the angular frequency) and the las term of Eq. 5.26 is calculated from the HB dynamics (see Eq. 1.4) as:

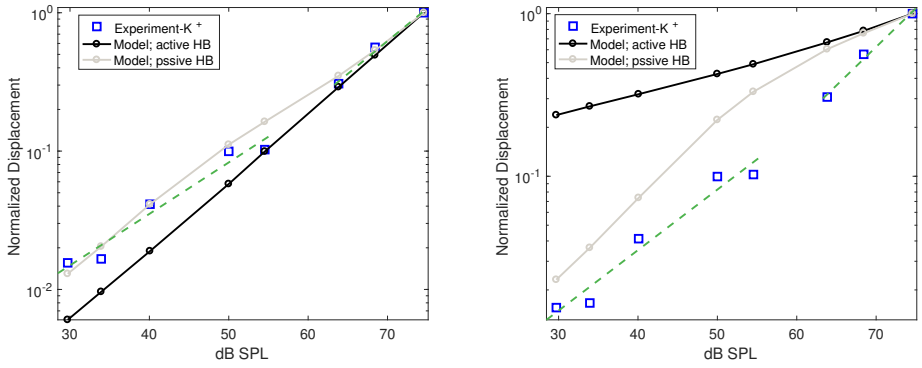

Figure 5.16: The HB motility effect on the compressive nonlinearity. The HB displacements at the resonance peaks over a range of stimulus levels; experimental data (Fig.5 of [3]) and simulation results (with and without HB adaptation) for (a) Case I with μ=0.7 (b) Case II with $\mu = 1.5$. For passive HB motility, the adaptation motor displacement is fixed and gating spring is removed $k_{gs} = 0$ (to avoid instability).

$$\partial x_a/\partial u_{hb} = \frac{-k_{gs} + DC_p k_{gs} + \gamma f_{max}(1 - SC_p)}{-k_{gs} + DC_p k_{gs} - k_{es} - \gamma f_{max} SC_p + j\lambda_a \omega}, \tag{5.27}$$

where $C_p = P_0(1 - P_0)/\Delta X$ is a constant which depends on the resting probability of the MET channels P_0 and the displacement constant ΔX introduced in Eq. 1.1. The adaptation motor (x_a) is set to be stationary for the passive HB simulation ($\partial x_a/\partial u_{hb} = 0$ in Eq. 5.26) while the coupled dynamics of HB motion and the adaptation motor (Eq. 1.4) is implemented for the active HB model. Figure 5.18 compares the frequency dependency of the MET sensitivity for the active and passive HB models. It is shown that implementing the HB adaptation in the MET dynamics reduces the sensitivity significantly for Case I parameters while Case II gives rise to an enhancement in MET sensitivity. This result implies that the HB adaptation process may affect the cochlear dynamics through controlling the MET sensitivity (see Chapter II for more detail). Figure 5.17 shows the transduction current variation relative to the HB motion for Case I (panel a) and Case II (panel b) parameters while μ is set such that the dynamics are near the Hopf point. It is noted that the HB adaptation changes both the shape of the curve as well as the slopes (representative sensitivity).

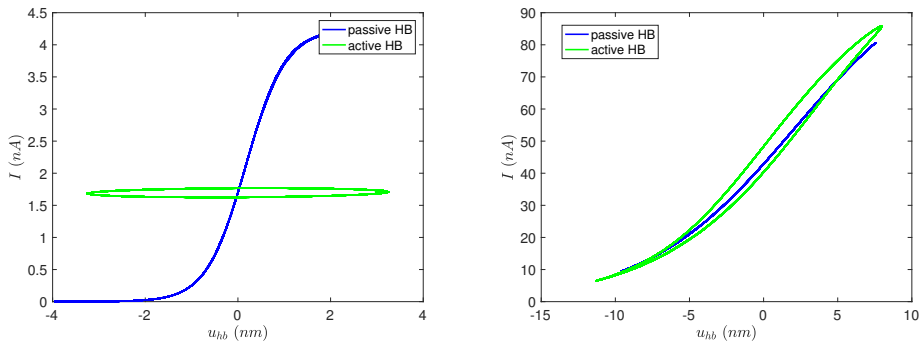

(a) (b)

Figure 5.17: The MET current transduction (a) Case I with μ=0.7(b) Case II with $\mu = 1.5$ for 67 dB SPL and freq=1.18 kHz.

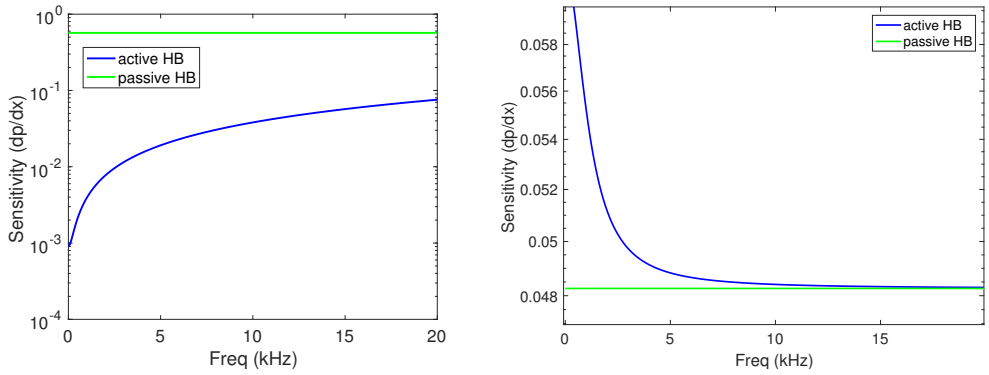

(a) (b)

Figure 5.18: Sensitivity of the MET current transduction for (a) Case I with μ=0.7 and (b) Case II with $\mu = 1.5$.

HB activity creates a hysteresis loop that gives rise a cycle-by-cycle power generation. The HB active model with case I parameters gives rise to a significant decrease in sensitivity while Case II enhances MET sensitivity slightly.

5.6 Discussion

Chan and Hudspeth [3, 4] used artificial endolymphatic fluids that act on the MET channels and examined contribution of the HB motility on the cochlear amplifier. They measured the cochlear response under replacement of the normal K^+ rich endolymph with BAPTA (which disrupts tip links [87]), NMDG (K^+ blocker of

transduction-channel [76]) and amiloride (MET blocker [88]). It is reported [3] that "...when the apical surface of the sensory epithelium was bathed in NMDG-based endolymph and a transepithelial potential was applied, little microphonic potential could be recorded, yet amplification was still observed..." which led the authors to conclude that "this dissociation of the receptor potential (as reflected in the microphonic potential) from the active process (as revealed by the compressive nonlinearity) argues against the participation of any membrane potential based process such as somatic electromotility at the frequencies studied here". However, it is not clearly discussed why the *little* recorded CM is not sufficient for the small nonlinearity observed in these experiments (the power-law slope of 0.7-0.8 comparing to 0.3 measured from the intact cochlea).

Although the Chan-Hudspeth experiments are remarkable for preserving the cochlear activity on an excised segment and observing its manifestation on the nonlinear amplification, their interpretation of the data remains elusive. Hence, their conclusion cannot be reconciled with other studies in mammalian amplifier [30, 32] where they shows the OHC motility is needed for amplification. In order to shed new insights into the Chan and Hudspeth analysis of the underlying active mechanism in mammals we simulated their experiments with corresponding mechanical, acoustical and electrical boundary conditions. Replacement of the K^+ rich endolymph by channel-impermeant NMDG in the experiment [3] was shown to increase the power-law dependency of the compressive nonlinearity from 0.74 to 0.85 (1 being linear) and reduce the microphonic response by 57% (Fig. 5.14(a)). When we simulate the same conditions (allowing only Ca^{2+} ions to pass through the MET channel), the model (with somatic electromotility as the sole mediator of the active process) predicts a 56% reduction in cochlear microphonic (Fig. 5.14(a)) and power-law changes from 0.75 to 0.86 (Fig. 5.14(b)). These results suggest that the CM in this preparation is sufficient for the somatic active process to produce the small nonlinearity seen in the experiments (Fig .5.14(b)).

This finding is also supported by the electrically-evoked motion measurements in the Chan-Hudspeth experiment. As it is illustrated in Fig. 5.15, the electrically evoked motion of the HBs are not changed by altering the CM (*i.e.* using NMDG) implying that the entry of Ca^{2+}, which persists in NMDG endolymph, is sufficient to mediate the full extent of electrically evoked hair-bundle movement. In our model with the HB motility, eliminating the somatic force linearizes the responses (data not shown)

Our physiologically-based model of the cochlea allows us to assess possible contribution of the alternative active mechanism (HB motility) on the measured nonlinear responses. In order to account for the possible contribution of the HB motility on the nonlinear responses seen in the Chan-Hudspeth experiments, a HB active model [1] is incorporated into the microstructure of the OoC (see Fig. 1.2). The HB dynamics is linked to the MET current transduction (see Eq. 1.1) that triggers the OHC somatic electromotility. Hence, implementing the adaptation process to the HB dynamics reflects on the sensitivity of the MET channels as well as the OHC somatic forces. It is shown in our model that the HB adaption with physiologically valid parameter values may reduce the MET sensitivity dramatically (Fig. 5.18(a)) in a frequency dependent fashion. This reduction of the MET sensitivity abolishes the transduction current and thus the compressive nonlinearity (Fig. 5.16(a)).

Table 5.3: Material properties for the gerbil cochlear model (x is in meters) and the geometrical boundary dimensions ($m_0 = 10mg$)

Property	Description	Value
b	BM width	80 μm base - 180 μm apex
L_{bm}	BM length	700 μm
h_{bm}	BM thickness	7 μm base - 1.7 μm apex
K_{bm}	BM stiffness per unit area	$4.49 \times 10^9 (h_{bm}/h_{bm0})^3 (b_0/b)^4$ N/m^3
K_{tms}	TM shear stiffness per unit length	$1.2333 \times 10^4 e^{-672.7x}$ N/m^2
K_{tmb}	TM bending stiffness per unit length	$1.2333 \times 10^4 e^{-672.7x}$ N/m^2
K_{rl}	RL stiffness per unit length	$4.0083 \times 10^3 e^{-706.4x}$ N/m^2
K_{ohc}	OHC stiffness per unit length	$4.0083 \times 10^3 e^{-706.4x}$ N/m^2
K_{st}	Stereocilia stiffness	$1.879 \times 10^4 e^{(-706.4x)}$ N/m^2
M_{bm}	BM mass per unit area	$\rho_{bm} h_{bm}$ ($\rho_{bm} = 1000$ Kg/m^3)
M_{tms}	TM shear mass per unit length	$1.08 \times 10^{-12} e^{(84.09x)} \rho_{tm}$ Kg/m , ($\rho_{tm} = 1000$ Kg/m^3)
M_{tmb}	TM bending mass per unit length	0.7 M_{tms}
c_{bm}	BM damping coefficient per unit length	0.03 Ns/m^2
c_{tms}	TM shear damping coefficient per unit length	0.03 Ns/m^2
c_{tmb}	TM bending damping coefficient per unit length	0.05 Ns/m^2
L_{hb}	HB length	1 μm base - 6 μm apex
G^{max}	saturating HB conductance	800.36×10^4 L_{hb0}/L_{hb} $e^{(-252.3x)}$ S/m^2
ε_3	electromechanical coupling coefficient	$-122e^{-7}$ (base) to $-152e^{-7}$ (apex) N/m/mV
ΔV^0	resting potential difference between v_{sm} and v_{ohc}	150 (base) to 131.5 (apex) mV
H_{sm}	scala media height	2.5 mm
W_{sm}	scala media width	11 mm
L_{sm}	scala media length	2.5 mm
L_{st}	scala tympani length	1.8 mm
W_{st}	scala tympani width	1.4 mm
H_{st}	scala tympani channel height	3.9 mm

Table 5.4: Parameter values for the hair bundle model introduced in Eq. 1.4. Two sets of parameters are considered; Case I from [1, 2] and Case II.

Property	Description	Case I	Case II
k_{gs}	Gating spring stiffness (mN/m)	8	0.95
k_{es}	Extension spring stiffness ($\mu N/m$)	750	4
k_{sp}	Stereocilia pivot stiffness (mN/m)	3.1	4
λ	Effective stereocilia damping ($\mu Ns/m$)	0.28	0.28
λ_a	Adaptation motor damping ($\mu Ns/m$)	0.5	0.5
f_{max}	Motor strength (nN)	1.3	0.02
S	Strength of the Ca^{2+} feedback on the motor force	4	1
γ	Geometric gain	0.25	0.2
d	Microscopic gating swing (nm)	15	8.7
N	Number of transduction elements	50	50
f_{gs}	single channel gating spring force (pN)	9.7	0.82

CHAPTER VI

Application of the WKB Method for an Active Cochlear Model

6.1 Introduction

The Wentzel-Kramers-Brillouin (WKB) method has been used to approximate the solution for systems with slowly varying properties. This analytic method is computationally efficient, and provides insights into the physical problem by decomposing the solution into a dominant wave number and the associated amplitude. This method has been utilized to solve the cochlear mechanics problem which involves slow variation of the parameters along its length (*e.g.,* see [85, 89]). Application of this method in the cochlear problem provides a unique insight into wave propagation while the its simpler computationally comparing to other methods such as FEM. However, there have been some limitations on the WKB method to the cochlear mechanics. When the BM is modeled as a locally reacting impedance, the WKB solution provides a fairly good approximation of cochlear response before the resonance peak, but beyond that, it shows a far-too-large downward slope which fails to agree with other numerical solutions [90]. Because of its computational efficiency, this method provides a convenient means to estimate parameters in a complicated cochlear model, through variation and optimization.

Previously, the WKB method has been used to solve passive cochlear problem which is based on the fluid-structure interaction of the BM and intracochlear fluid. In this study, we extend the WKB approximation to an active model that includes the micromechanics of the OoC coupled to the electrical potentials inside the cochlea. The OHC electromotility is the sole mediator of the active processes. The frequency response of the cochlea together with the dispersion relations are calculated and compared for passive and active models.

6.2 Mathematical Model

6.2.1 Passive cochlea

The simplified passive cochlear model consists of an unwrapped rectangular fluid-filled single duct with dimensions L, L_1 and L_2 in directions x, y and z, respectively, as shown in Fig. 6.1. An incoming sound wave is injected into the fluid from one side of the duct and propagates down the length of the duct, interacting with a flexible membrane on the bottom wall. In this study an orthotropic plate with varying stiffness along its length is used for the BM model. The fluid inside the duct is assumed to be inviscid, compressible, and irrotational. The formulation of the WKB method application on the cochlea passive problem, developed by Steele and Taber [85], is presented in this section. The plate governing equation for an orthotropic model is introduced as:

$$D_{xx}\frac{\partial^4 w_p}{\partial x^4} + 2(D_{xy} + 2D_{sh})\frac{\partial^4 w_p}{\partial x^2 \partial y^2} + D_{yy}\frac{\partial^4 w_p}{\partial y^4} - \rho_p \omega^2 t w_p = -p(x, y, 0) \qquad (6.1)$$

where D_{xy}, D_{sh} and D_{yy} represent the bending stiffness in different directions and ρ_p is the fluid density. w_p is the BM displacement which can be expressed as the summation of the modes in x direction.

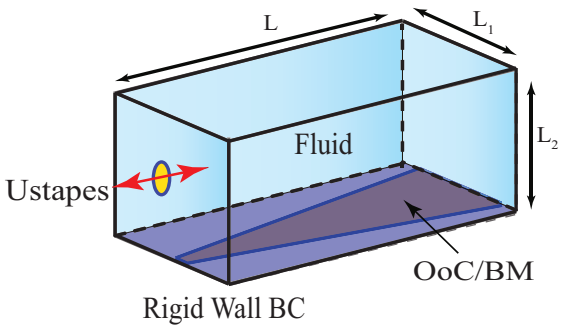

Figure 6.1: Rectangular duct modeling idealization of the cochlea.

$$w_p(x,y,t) = \sum_r W_r(x)\eta(y)e^{i\theta} \tag{6.2}$$

where $W_r(x)$ is the BM spatial variation in the x direction and the phase $\theta(x,t) = \omega t - \lambda x$ contains the wave number λ and frequency ω. We have used the BM first mode in the radial direction for the hinged boundary condition (BC):

$$\eta(y) = \sin\left(\frac{\pi(y+b/2)}{b}\right) \tag{6.3}$$

where b is the BM width. For the sake of convenience, we define the derivative operator of Eq. 6.1 as:

$$\mathcal{L}\,() = D_{xx}\frac{\partial^4()}{\partial x^4} + 2(D_{xy}+2D_{sh})\frac{\partial^4()}{\partial x^2\partial y^2} + D_{yy}\frac{\partial^4()}{\partial y^4} - \rho_p\omega^2 t() \tag{6.4}$$

so, Eq. 6.1 can be expressed as :

$$\mathcal{L}\,[w_p] = -p_{(x,y,0,t)} \tag{6.5}$$

A velocity potential is approximated for the fluid in the x and z directions:

$$\phi = \sum_{j=0} B_j \cosh m_j(z - L_2) \cos(j\pi y/L_1) e^{i\theta} \tag{6.6}$$

where B_j is calculated to satisfy fluid-structure interaction BC at $z = 0$ (after integrating out y the dependence):

$$\frac{\partial w_p}{\partial t}|_{z=0} = \frac{\partial \phi}{\partial z}|_{z=0} \tag{6.7}$$

Substituting the first mode of the BM displacement (Eq. 6.2) and Eq. 6.6 into Eq. 6.7 we get:

$$B_j = \frac{-i\omega W A_j e_j}{m_j L_1 \sinh m_j L_2} \tag{6.8}$$

where $m_j^2 = (j\pi/L1)^2 + \lambda^2$ represents wave constant in z direction and

$$A_j = \int_{-b/2}^{b/2} \eta(y) \cos(j\pi y/L_1) dy \tag{6.9}$$

Now, we can find pressure distribution inside the duct from the velocity potential ($p = -\rho \frac{\partial \phi}{\partial t}$) which then can be plugged into Eq. 6.5 to get:

$$\mathcal{L}\left[W(x)\eta(y)e^{i\theta}\right] = -\rho \sum_j B_j \cosh m_j L_2 \cos(j\pi y/L_1) i\omega e^{i\theta} \tag{6.10}$$

Using the orthogonality properties of the modes, we integrate out the y dependence by multiplying both sides of Eq. 6.10 by $\eta(y)$ and integrating over the BM width:

$$\begin{aligned} D_{xx} D_0 \tfrac{\partial^4 W_r}{\partial x^4} + 2F_1(D_{xy} + 2D_{sh}) \tfrac{\partial^4 W_r}{\partial x^2 \partial y^2} + D_{yy} G_1 \tfrac{\partial^4 w_r}{\partial y^4} - D_0 \rho_p \omega^2 t w_r = \\ \textstyle\sum_j \frac{\rho \omega^2 A_j^2 e_j}{m_j L_1 \sinh m_j L_2} \cosh m_j L_2 W_r \end{aligned} \tag{6.11}$$

where the integration coefficient are calculated as:

$$D_0 = \int_{-b/2}^{b/2} \eta^2 dy \qquad F_1 = \int_{-b/2}^{b/2} \frac{d^2\eta}{dy^2}\eta dy \qquad G_1 = \int_{-b/2}^{b/2} \frac{d^4\eta}{dy^4}\eta dy \tag{6.12}$$

Now we redefine the $\mathcal{L}$ operator to include these coefficients:

$$\mathcal{L}' = D_{xx}D_0\frac{\partial^4}{\partial x^4} + 2F_1(D_{xy} + 2D_{sh})\frac{\partial^2}{\partial x^2} + D_{yy}G_1 - D_0\rho_p\omega^2 t \tag{6.13}$$

hence, Eq. 6.10 get the form

$$\mathcal{L}'\left[W_r\right] = \sum_j \frac{\rho_f\omega^2 A_j^2 e_j}{L_1 m_j \tanh m_j L_2} W_r \tag{6.14}$$

Considering displacement dependence on x as $W_r(x) = We^{i\theta}$ and canceling out W from both sides of this equation we get the *eikonal* equation:

$$f(\lambda)_{passive} = F_r(\lambda) - \rho_f\omega^2 h_{eq}(\lambda) \tag{6.15}$$

This equation represents the BM dispersion relation and the fluid effective height is calculated as:

$$h_{eq} = \sum_j \frac{A_j^2 e_j}{L_1 m_j(\lambda) \tanh\left(m_j(\lambda) L_2\right)} \tag{6.16}$$

where

$$F_r(\lambda) = D_{xx}D_0\lambda^4 - 2F_1(D_{xy} + 2D_{sh})\lambda^2 + D_{yy}G_1 - D_0\rho_p\omega^2 t \tag{6.17}$$

Solving for the roots of Eq. 6.15, we can calculate wave numbers associated with the wave propagating along the BM. Next we plug the corresponding wave numbers into the *transport* equation (see [85]) to calculate the BM vibration amplitude:

$$W = C(\frac{\partial f}{\partial \lambda})^{-1/2} \tag{6.18}$$

6.2.2 Eikonal equation for the OoC microstructure

In the previous section the *eikonal* equation for the configuration of Fig. 6.1 is calculated. Next, we modify the *eikonal* equation to include electro-mechanical components of the OoC. Figure 1.1 depicts a schematic of the OoC and transverse section of the model. For this system we have the following frequency domain dynamical equation in a matrix format:

$$\left[K_{sys}\right]\bar{U} = 0 \tag{6.19}$$

where $\bar{U} = [\mathbf{U}\ \phi]^T$ is the nodal vector of structural displacements $\mathbf{U} = [u_{bm}\ u_{tms}\ u_{tmb}]$ and electrical voltages $\phi = [\phi_{sv}\ \phi_{sm}\ \phi_{ohc}\ \phi_{st}]$. The system dynamical matrix is defined as $\mathbf{K}_{sys} = -\mathbf{M}\omega^2 - i\omega\mathbf{C} + \mathbf{K}$ in which the sub-martices $\mathbf{M}$, $\mathbf{C}$, and $\mathbf{K}$ are the structural mass, damping, and stiffness of the OoC cross section slowly varying along the cochlea. The formulation of the OoC electro-mechanical matrices are defined in the Appendix A.

The *eikonal* equation corresponding to the BM-fluid interaction is calculated in Eq. 6.15. In order to calculate the *eikonal* equation of the whole OoC, a new dynamical matrix $\tilde{\mathbf{K}}$ is formed by substituting the first entry of $\mathbf{K}_{sys}$ for $F_r(\lambda)$ and setting the determinant equal to zero:

$$f(\lambda)_{active} = det(\tilde{K}) = 0 \tag{6.20}$$

Note that only the first element of $\tilde{\mathbf{K}}$, which is the BM dynamical stiffness, is a function of the wave number (λ). This *eikonal* equation is solved using a numerical method (Newton Rophson) to find the root locus along the cochlea for active and passive models. Then Eq. 6.2.1 is used to calculate displacement amplitudes.

Parameters are used for this study are listed in Table 6.1. Moreover, parameters of the OoC model are used from [25].

Table 6.1: WKB model parameters.

Parameter	Value	Description
L	1.85×10^{-2}	duct length (m)
L_1	10^{-3}	duct width (m)
L_2	10^{-3}	duct height (m)
t	8×10^{-6}	plate thickness (m)
b_0	10^{-4}	plate width at x =0 (m)
b_f	8×10^{-4}	plate width at x=L (m)
ρ_f	1000	fluid density (kg/m^3)
ρ_p	1000	BM density (kg/m^3)
c	1500	sound speed in fluid (m/s)
E_y	$10^9(1 + 0.1j)$	Young's Modulus of the Plate in y direction (Pa)
E_x	$0.01 \times 10^9(1 + 0.1j)$	Young's Modulus of the Plate in x direction (Pa)
V_{yx}	0.3	Poisson's ratio

6.3 Results

The geometry of the long slender duct and the mechanical properties of the partition are assumed to be slowly varying functions of the lengthwise coordinate x, allowing use of the WKB approximation to study wave propagation. The OHC electromotility is the mediator of the active process in this model. The active process contribution on the wave numbers are demonstrated in Figs. 6.2. This figure shows the real and imaginary parts of the smallest wavenumbers for the active and passive models. The root with $Re(\lambda) > 0$ and $Im(\lambda) < 0$ represents the right-running wave. It is shown that the activity decreases the wavelength near the CF and makes the imaginary part more negative, which sharpens the responses as shown in Figs. 6.3.

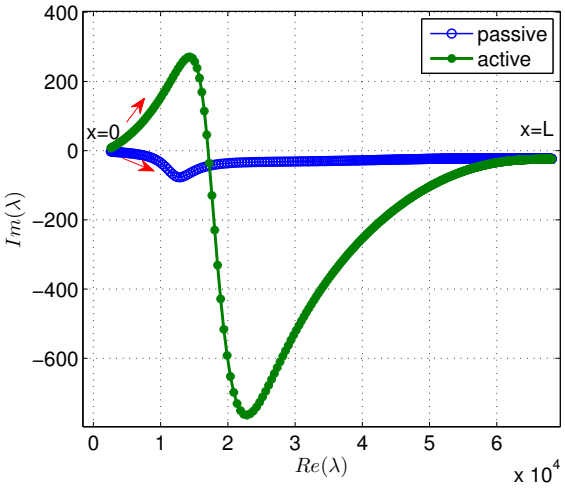

Figure 6.2: The first wave number calculated from the eikonal equation for active and passive models.

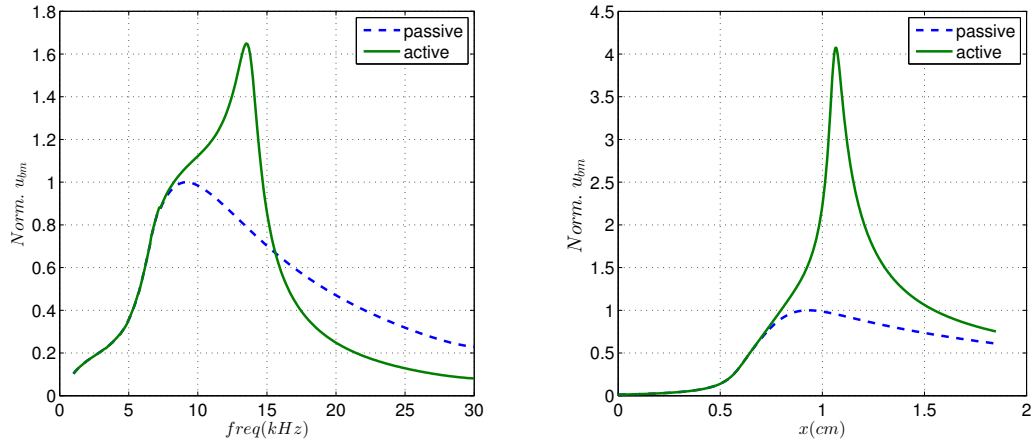

Figure 6.3: (a) The WKB frequency response for active and passive models. Activity sharpen and amplify the response near the characteristic frequency. For higher frequencies the active model response is lower than the passive one which is probably related to involvement of other modes which are neglected. (b) The WKB spatial response for active and passive models.

CHAPTER VII

Conclusions and Future Works

7.1 Conclusions

The overarching goal of this thesis was to develop a computational model of the mammalian auditory system that helps gaining a deeper understanding of the mechanics of hearing. This model describes the response of the cochlea to both external acoustic and internal electrical stimulations. The highly debated issue of the identity of the cochlear amplifier is addressed in this thesis. The proposed active mechanisms (OHC somatic electromotility and HB motility) are implemented into our model and their relative contribution on the cochlear mechanics is investigated. It is shown that somatic based activity plays a fundamental role in the amplifier while the HB motility contribution remains elusive. In this study, we have found that the power gain by hair bundle motility is 10^3-10^5 times smaller than the somatic force. Hence, it is unlikely that hair bundle motility itself can amplify OoC motions and that OHC somatic motility is the the primary driver for cochlear amplification. However, it is shown that by coupling active hair bundle motility to somatic motility, it is possible to hasten the onset of compressive nonlinearity along with an increase in the low stimulus gain. We identify two possible distinct mechanisms through which the HB activity affects the cochlear dynamics. One mechanism generates a cycle-by-cycle power into the OoC dynamics while causes a significant decrease in the MET sensi-

tivity. This mechanism is not able to amplify the cochlear responses as observed *in vivo*. The second mechanism, however, enhances the MET sensitivity which boosts the OHC somatic force. In our model, the first mechanism is most effective at basal locations (higher frequencies) while the second mechanism works better at apical locations (lower frequencies). Hence, a transition of the dynamics from base to apex is proposed as a possible contribution of the HB on the cochlear mechanics.

Furthermore, we modeled an *in vitro* active experiment conducted by Chan and Hudspeth [3–5] as an ideal configuration to study the cochlear nonlinear amplifier in a semi-intact and controlled configuration. It is shown that the OHC somatic electromotility, rather that HB motility, is sufficient to predict the nonlinearities observed in these experiments. The power generation by the HB active mechanism is not sufficient to reproduce the amplification observed in the experimental data, however, the adaptation process can regulate the MET sensitivity and boost the OHC somatic force. We conclude that the somatic force is the primary force transducer in the OoC and that the hair bundle adaptation mechanism most likely controls the larger somatic force by fine modulation of the gating force and MET current.

The compressive nonlinearity is a hallmark of a healthy cochlea. Our model in conjunction with experimental data were used to identify the underlying mechanism that onsets the cochlear nonlinearity. As observed *in vivo*, our model predicts that the OHC extracellular voltages undergo a phase shift at frequencies slightly below the peak, that coincides with the onset of the nonlinear amplification. It is hypothesized that this phase difference between the electrical and mechanical responses gives rise to effective power generation of the OHC somatic force. This phase transition is generated by the TM resonance properties in the radial direction. It is proposed that the TM plays a central role in setting appropriate phase relations between electrical and mechanical components to shift the somatic active force from dissipative to generative at frequencies slightly below the CF. The shear resonant TM scheme finds support

from *in vivo* and *in vitro* observations.

7.2 Future work

While the importance of a resonant TM has been speculated upon for many years [57, 59, 60], our analysis of experimental data in view of our mathematical model has given new insights on how to test this hypothesis. A CM measurement in the otoancorin decient [92] and wild type mouse holds the potential to prove or disprove this hypothesis as the notch in the voltage frequency response and phase shift would not be seen under this hypothesis. A mouse specific model would be needed to simulate both the normal mouse and the otoancorin knock out mouse's response to acoustic stimulus and test our hypothesis.

While some experimental data are supportive of our model guided hypothesis that the phase difference between electrical and mechanical components sets the OHC active force in the generative region, results from [62] do not show this same phase shift. Hence, more investigation is needed to determine if this discrepancy is due to different techniques used for voltage and displacement measurements or another as yet unknown effect. The advent of new measurement techniques, such as OCT holds potential to obtain more consistent data in multiple labs. OCT enables measurement of structures through the tissue at both the base and apex enabling simultaneous measurement of BM, TM, and RL motion [53, 67, 93]. Different groups including Olson lab (Columbia University) and Nuttall lab (Oregon Hearing Research Center) are capable to develop an experimental set up which allows simultaneous measurements of the OoC motions (using OCT) and electrical responses.

The electrical current flow along the ST is hypothesized to play a role in the energy distribution of the active process and effect the longitudinal coupling. However, there are some modeling efforts [94, 95] showing this effect is not significant inasmuch the voltage space constant is too small for electrical coupling between neighboring

cells. The cochlear electro-physiology is not well studied *in vivo*. Hence, more experimental data on electrical paths inside the cochlear ducts are essential in order to validate/invalidate our cable model (described in [27]). One possible experiment is injection of current in the round window and recording voltage responses in a nearby location. These measurement enable us to calculate the voltage space constant inside the ST.

APPENDIX A

Micro-electro-mechanical Model of the OoC

Kinematics of the OoC

Figure A.1 shows a schematic of the microstructure of the OoC used in this study. The variables u_{bm}, u_{tms} and u_{tmb} represent displacements of the BM, TM shear and TM bending modes, respectively.

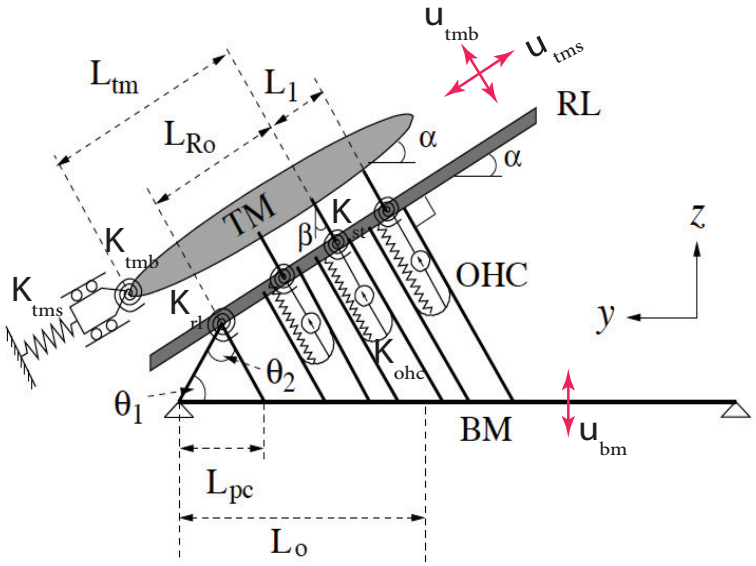

Figure A.1: Microstructure of the OoC model [27].

The Kinematics of the OoC structure is modeled using the Lagrange's method as in [27]. Here we assume that the angles associated to the TM and HB orientations (see Fig. A.1) are equal ($\alpha = \beta$) and also $\theta_1 = \theta_2 = 60°$. Hence, the dynamics of the OoC can be further simplified. The formulation for important quantities are listed in the Table A.1.

Table A.1: Kinematics of the OoC formulations. Th subscripts $j = 1, 2, 3$ denotes the cell number.$\psi_1(y) = \sin\left(\frac{\pi(y+b/2)}{b}\right)$

Description	Formula
OHC-apex toward the BM and along the OHC	$u^a_{ohci} = u_{bm}(x)\psi_1(b/2 - Lpc) \times (-\cos(\theta_1 - \alpha) + a_j \cos(\theta_1 - \beta)) - a_j u_{tmb}(x)$ $, a_1 = 1 - \frac{L_1}{L_{ro}}, a_2 = 1, a_3 = 1 + \frac{L_1}{L_{ro}}$
OHC-base toward the RL and along the OHC	$u^b_{ohci} = u_{bm}(x)\psi_1(b/2 - b_j)\cos(\alpha)$ $, b_1 = L_0 - \frac{L_1}{\cos(\alpha)}, b_2 = L_0, b_3 = L_0 + \frac{L_1}{\cos(\alpha)}$
HB displacement normal to HB toward the outer rows	$u^a_{hbi} = u_{bm}(x)\psi_1(b/2 - Lpc)\sin(\theta_1 - \alpha) + g_j u_{tms}$ $, g_1 = (1 - L1/Ltm), g_2 = 1, g_3 = (1 + L1/Ltm)$
RL displacement normal to RL away form the OHC	$u_{rli} = a_j\left(-u_{bm}(x)\psi_1(b/2 - L_{pc})\cos(\theta_1 - \beta) + u_{tmb}(x)\right)$

Electrical Components

A cable model is used to represent the macroscopic current flow along the cochlear ducts as shown in Fig. A. The deflection of the HB of the OHC triggers the opening of the MET channels resulting in current flow into the OHC. In each cross-sectional circuit branch, there are four electrical potentials corresponding to scala vestibuli (ϕ_{sv}), scala media (ϕ_{sm}), OHC (ϕ_{ohc}) and scala tympani (ϕ_{st}).

$$-\left(\frac{1}{R_{vl}} + \frac{1}{R_v m}\right)\phi_{sv} + \frac{\phi_{sm}}{R_{vm}} = 0 \tag{A.1}$$

$$\frac{1}{R_{vm}}\phi_{sv} - \left(\frac{1}{R_{vm}} + 3Y_a\right)\phi_{sm} + 3Y_a\phi_{ohc} - I_{s1} = 0 \tag{A.2}$$

$$3Y_a\phi_{sm} - 3(Y_a + Y_m)\phi_{ohc} + 3Y_m\phi_{st} + I_{s1} - I_{s2} = 0 \tag{A.3}$$

$$3Y_m\phi_{ohc} - \left(\frac{1}{R_{tl}} + 3Y_m\right)\phi_{st} + I_{s2} = 0 \tag{A.4}$$

where $Y_a = 1/R_a^0 + i\omega C_a$ is the apical OHC admittance and $Y_m = 1/R_m + i\omega C_m$ is the basolateral admittance.

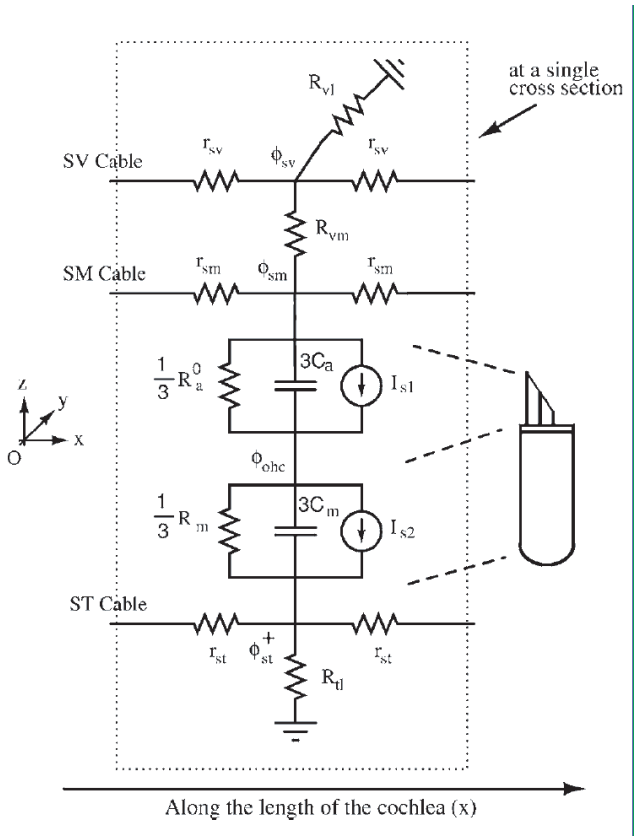

Figure A.2: Electric Network at Cross Section [27].

Hair Bundle and OHC

The HBs are assumed to have a conductance which changes nonlinearly with the deflection of the HB. It can be linearized to:

$$I_{hbj} = G_{aj} V_{sm/ohc} \tag{A.5}$$

where $V_{sm/ohc}$ represents the voltage difference between SM and OHC:

$$V_{sm/ohc} = (\phi_{sm} + V_{sm}) - (\phi_{ohc} + V_{ohc}) \tag{A.6}$$

Here V_{sm} and V_{ohc} are the SM and OHC voltages at resting state while ϕ_{sm} and ϕ_{ohc} are fluctuating parts of the voltage introduced in Eqs. 5.24-**??**. In Eq. A.5 the conductance for the jth HB (G_{aj}) is the summation of the conductance at the resting state ($G_a^0 = 1/R_a^0$) and the fluctuating part:

$$G_{aj} = G_a^0 + G_a^1 u_{hbj} \tag{A.7}$$

where the HB displacement (u_{hb}) is presented in the Table A.1. The HB current can be calculated as:

$$I_{hbj} = (G_a^0 + G_a^1 u_{hbj} + i\omega C_a) * (\phi_{sm} - \phi_{ohc} + V_{sm} - V_{ohc}) \tag{A.8}$$

and after neglecting small terms we have:

$$I_{hbj} = (G_a^0 + i\omega C_a)(\phi_{sm} - \phi_{ohc}) + (V_{sm} - V_{ohc}) G_a^1 u_{hbj} \tag{A.9}$$

The HB current source (I_{s1}) shown in Fig. A is the part that varies by HB motion:

$$I_{s1} = (V_{sm} - V_{ohc}) G_a^1 \sum u_{hbj} \tag{A.10}$$

The OHC active force is modeled as:

$$F_{ohcj} = K_{ohc} u_{ohcj}^{com} + \epsilon_3 (\phi_{ohc} - \phi_{st}) \tag{A.11}$$

where $u^{com}_{ohcj} = u^{a}_{ohcj} + u^{b}_{ohcj}$ (see Table A.1) is the OHC compression and ϵ_3 is the OHC electromechanical coupling coefficient. Moreover, the OHC current is:

$$I_{ohcj} = (\phi_{ohc} - \phi_{st})/Z_m - i\omega\epsilon_3 u^{com}_{ohcj} \tag{A.12}$$

where Z_m is the OHC basolateral impedance, ε_3 is the electromechanical coupling coefficient and K_{ohc} represents the OHC stiffness. The OHC current source (I_{s2}) is the OHC motion dependent part:

$$I_{s2} = -\epsilon_3 d(u_{ohc})/dt = -i\omega\epsilon_3 u^{com}_{ohcj} \tag{A.13}$$

The OoC Cross Section Equations of Motion

The equations of motion for the OoC electro-mechanical components can be derived in the following matrix format:

$$\begin{bmatrix} M_s & 0 \\ 0 & 0 \end{bmatrix} \begin{bmatrix} \ddot{\mathbf{U}} \\ \ddot{\phi} \end{bmatrix} + \begin{bmatrix} C_s & C_{se} \\ C_{es} & C_e \end{bmatrix} \begin{bmatrix} \dot{\mathbf{U}} \\ \dot{\phi} \end{bmatrix} + \begin{bmatrix} K_s & K_{se} \\ K_{es} & K_e \end{bmatrix} \begin{bmatrix} \mathbf{U} \\ \phi \end{bmatrix} = F; \tag{A.14}$$

These equations relate the OHC strain and transmembrane voltage to the OHC force and current. Based on these equations we have $K_{se} = C^T_{es}$ which, indicates that energy is conserved through the OHC electromotility.

that couples the structural displacements $\mathbf{U} = [u_{bm}\ u_{tms}\ u_{tmb}]^T$ to the electrical voltages $\phi = [\phi_{sv}\ \phi_{sm}\ \phi_{ohc}\ \phi_{st}]^T$ where T represents transpose and the structural-electrical sub-matrices are:

$$\mathbf{M_s} = \begin{bmatrix} M_{bm} & 0 & 0 \\ 0 & M_{tms} & 0 \\ 0 & 0 & M_{tmb} \end{bmatrix};\ \mathbf{C_s} = \begin{bmatrix} c_{11} & c_{12} & c_{13} \\ c_{21} & c_{22} & c_{23} \\ c_{31} & c_{32} & c_{33} \end{bmatrix};\ \mathbf{C_e} = \begin{bmatrix} 0 & 0 & 0 & 0 \\ 0 & -C_a & C_a & 0 \\ 0 & C_a & -C_a - C_m & C_m \\ 0 & 0 & C_m & -C_m \end{bmatrix}$$

$$\mathbf{C_{es}} = \begin{bmatrix} 0 & 0 & 0 \\ 0 & 0 & 0 \\ \epsilon_3(C_1 + E_1) & \epsilon_3 C_3 & \epsilon_3 C_4 \\ -\epsilon_3(C_1 + E_1) & -\epsilon_3 C_3 & -\epsilon_3 C_4 \end{bmatrix};\ C_{se} = [0];\ \mathbf{K_s} = \begin{bmatrix} k_{11} & k_{12} & k_{13} \\ k_{21} & k_{22} & k_{23} \\ k_{31} & k_{32} & k_{33} \end{bmatrix};$$

$$\mathbf{K_{se}} = \begin{bmatrix} 0 & 0 & (C_1 + E_1)\epsilon_3 & -(C_1 + E_1)\epsilon_3 \\ 0 & 0 & C_3\epsilon_3 & -C_3\epsilon_3 \\ 0 & 0 & C_4\epsilon_3 & -C_4\epsilon_3 \end{bmatrix};\ \mathbf{K_{es}} = \begin{bmatrix} 0 & 0 & 0 \\ -A_1 q & -A_3 q & -A_4 q \\ A_1 q & A_3 q & A_4 q \\ 0 & 0 & 0 \end{bmatrix};$$

$$\mathbf{K_e} = \begin{bmatrix} -1/R_{vl} - 1/R_{vm} & 1/R_{vm} & 0 & 0 \\ 1/R_{vm} & -1/R_{vm} - 1/R_{a0} & 1/R_{a0} & 0 \\ 0 & 1/R_{a0} & -1/R_{a0} - 1/R_m & 1/R_m \\ 0 & 0 & 1/R_m & -1/R_{tl} - 1/R_m \end{bmatrix};$$

(A.15)

in which

$$C_1 = 0;\ E_1 = \sin(\frac{\pi(L_0 - L_1/\cos(\alpha))}{b} + \sin(\frac{\pi L_0}{b}) + \sin(\frac{\pi(L_0 + L_1/\cos(\alpha))}{b})\cos(\alpha)$$

$$C_3 = 0;\ C_4 = -3; A_1 = 3H\sin(\theta_1 - \alpha);\ H = \sin(\pi L_{pc}/b);\ A_3 = 3;\ A_4 = 0;$$

(A.16)

APPENDIX B

Hopf Normal Form

It has been suggested that the negative stiffness seen in mammalian OHCs, together with spontaneous oscillations of the hair bundle that has been observed in lower vertebrates, e.g. in bullfrogs, mean that the nonlinearity of hair cells can be essentially modeled as that of a nonlinear oscillator undergoing a Hopf bifurcation. Based on this fact, Eguluz et al. [40] presented the Hopf bifurcation normal form as a possible process of amplification. They argued that near resonance the response to stimulus relation is close to a cubic root, whereas at sufficient distance form resonance the linear relation will become dominant. Magnasco [37] used Hopf bifurcation to explain the shape of the cochlea tuning curves by analyzing energy flow and dissipation. Kim et al. [38] proposed a model including both damping and stiffness nonlinearity. They reported the stiffness nonlinearity, modeled with Duffing equation, increases frequency selectivity at high levels. Ó Maoiléidigh and Jülicher [2] proposed a model considering somatic motility, transduction current adaptation and nonlinearity and showed it is consistent with the experimental results by Kennedy et al. [22]. They incorporated myosin motor dynamics in their model of OHC which also included electrical domain through charge dynamics. Later Szalai et al. [39] simplified Maoiléidighh's model and studied two different bifurcations that may be the source

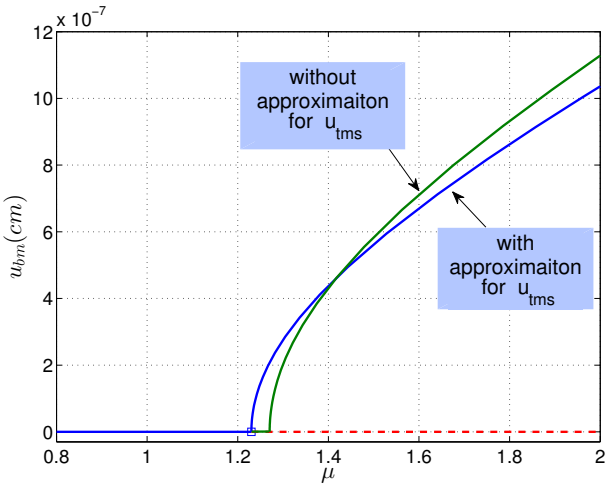

Figure B.1: Bifurcation diagram for BM displacement with and without TM shear mode approximation. Simplification reserves dynamics characteristic qualitatively.

of amplification. They argued that it is not necessary for local model of the OHC dynamics to take form of Hopf oscillator and there is possibility of other type of local bifurcation including saddle-node and cusp.

Hopf Normal From

In this section, we reduce the nonlinear dynamical system of Eq. B.1 near a Hopf bifurcation point.

$$\begin{bmatrix} M_s & 0 \\ 0 & 0 \end{bmatrix} \begin{bmatrix} \ddot{\mathbf{U}} \\ \ddot{\phi} \end{bmatrix} + \begin{bmatrix} C_s & C_{se} \\ C_{es} & C_e \end{bmatrix} \begin{bmatrix} \dot{\mathbf{U}} \\ \dot{\phi} \end{bmatrix} + \begin{bmatrix} K_s & K_{se} \\ 0 & K_e \end{bmatrix} \begin{bmatrix} \mathbf{U} \\ \phi \end{bmatrix} + f(\mathbf{U}) = F; \quad \text{(B.1)}$$

where the nonlinear terms (arising from MET transduction current) are set inside f. Numerical simulations revealed that TM shear displacement can be approximated as a linear function of BM displacement ($u_{tms} = \alpha u_{bm}$), while the dynamics are qualitatively consistent (Fig.B.1). Performing this simplification and shifting the bifurcation parameter to $\tilde{\mu}$=0, we can write the system in a state space as:

$$\dot{X} = A\mathbf{X} + \tilde{\mu}B\mathbf{X} + f(\mathbf{X}) \quad \text{(B.2)}$$

where $\mathbf{X}$=$[u_{bm}\ u_{tmb}\ \phi_{ohc}\ \phi_{st}\ \dot{u}_{bm}\ \dot{u}_{tmb}\ ]^T$ is the state vector, A and B represent the linear part of the dynamics, while f contains nonlinear terms. Because the origin is a Hopf bifurcation, two of the eigenvalues are purely imaginary complex conjugates (i.e., $\lambda_{1,2} = \pm i\omega$) and the remaining eigenvalues $(\lambda_3, ...\lambda_6)$ are in the left half of the complex plane. The idea is to find the normal form of Eq. (B.2) near $\mathbf{X} = 0$ for small $\tilde{\mu}$. We first decouple the linear part by introducing the transformation $\mathbf{X} = T\mathbf{Y}$ and obtain:

$$\dot{\mathbf{Y}} = J\mathbf{Y} + T^{-1}\tilde{\mu}BT\mathbf{Y} + T^{-1}f(T\mathbf{Y}) \tag{B.3}$$

where $J = T^{-1}AT$. We note that J can be written as:

$$J = \begin{bmatrix} J_c & 0 \\ 0 & J_s \end{bmatrix};\ J_c = \begin{bmatrix} i\omega & 0 \\ 0 & -i\omega \end{bmatrix} \tag{B.4}$$

and J_s is a 4×4 matrix whose eigenvalues are $\lambda_3, ..., \lambda_6$. We can express Eq. (B.3) in two parts, defining $\mathbf{Y_c}$ and $\mathbf{Y_s}$, where $\mathbf{Y_c}$ is a 2 dimensional vector with the component y_1 and y_2 and $\mathbf{Y_s}$ is 4 dimensional vector with the component $y_3, ...y_6$.

$$\begin{aligned} \dot{\mathbf{Y}}_\mathbf{c} &= J_c\mathbf{Y_c} + \tilde{\mu}B_{1c}\mathbf{Y_c} + \tilde{\mu}B_{1s}\mathbf{Y_s} + F_c(\mathbf{Y_c}, \mathbf{Y_s}) \\ \dot{\mathbf{Y}}_\mathbf{s} &= J_s\mathbf{Y_s} + \tilde{\mu}B_{2c}\mathbf{Y_c} + \tilde{\mu}B_{2s}\mathbf{Y_s} + F_s(\mathbf{Y_c}, \mathbf{Y_s}) \end{aligned} \tag{B.5}$$

Lets consider a local center manifold of the form:

$$\mathbf{Y_s} = \mathbf{N}(\mathbf{Y_c}) \tag{B.6}$$

where $\mathbf{N}$ consists polynomials as a function of $\mathbf{Y_c} = [y_{c1}, y_{c2}]$ satisfying two conditions: $N_i(0) = 0$ and $dN_i(0)/dY_c = 0$ for $i = 1, ..., 4$.

$$N_i = n_{1i}y_{c1}^2 + n_{2i}y_{c2}^2 + n_{3i}y_{c1}y_{c2} \tag{B.7}$$

After having manipulated Eqs. B.5-B.7 to obtain 4 polynomials and equating the coefficients of the different powers on both sides, one obtains a system of algebraic equations for the coefficients of the polynomials. Solving these equations, we obtain a first approximation to the center manifold $\mathbf{Y_s} = \mathbf{N}(\mathbf{Y_c})$. Therefore, we can substitute $\mathbf{Y_s}$ into the Eq. (B.5) and obtain the following two-dimensional system describing the dynamics on the center manifold.

$$\begin{aligned} \dot{y}_{c1} &= \omega y_{c2} + \tilde{\mu} C_{11} y_{c1} + \tilde{\mu} C_{12} y_{c2} + F_{c1}(y_{c1}, y_{c2}) \\ \dot{y}_{c2} &= -\omega y_{c1} + \tilde{\mu} C_{21} y_{c1} + \tilde{\mu} C_{22} y_{c2} + F_{c2}(y_{c1}, y_{c2}) \end{aligned} \tag{B.8}$$

Next, we use the method of normal forms to simplify the center manifold. First we calculate left and right eigenvector corresponding to J_c and call them $\mathbf{q}$ and $\mathbf{p}$ respectively. Then, we switch into a complex coordinate system, introducing:

$$\begin{pmatrix} y_{c1} \\ \\ y_{c2} \end{pmatrix} = \mathbf{p}u(t) + \bar{\mathbf{p}}\bar{u}(t) \tag{B.9}$$

where $\bar{\mathbf{p}}$ and $\bar{u}$ are complex conjugate of $\mathbf{p}$ and u respectively. Substituting Eq. B.9 into the center manifold equation (Eq. B.8) and multiplying the result from the left with $\mathbf{q}$ yields:

$$\dot{u} = i\omega u + \beta\tilde{\mu}u + P^2(u, \bar{u}, \tilde{\mu}) + P^3(u, \bar{u}, \tilde{\mu}) + H.O.T \tag{B.10}$$

where P^2 and P^3 are second and third order polynomials respectively and H.O.T denotes higher order terms. Now, we introduce a near-identity transformation [96] of the form:

$$u = v + H(v) \tag{B.11}$$

where $H(v) = b_1 v^2 + b_2 \bar{v}^2 + b_3 v\bar{v}$. Substituting this transformation into Eq. (B.10)

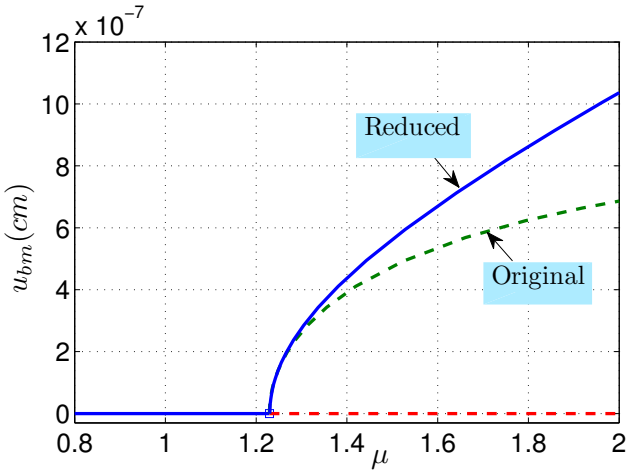

Figure B.2: Comparing Bifurcation Diagram for Original and Reduced system

and considering $(1 + D_v H(v))^{-1} \approx (1 - D_v H(v))$ we can get:

$$\dot{v} = \omega v + \beta\tilde{\mu}v + \tilde{P}^2(u, \bar{u}, \tilde{\mu}, b_j) + \tilde{P}^3(u, \bar{u}, \tilde{\mu}) + H.O.T \tag{B.12}$$

in which $\tilde{P}^2$ involves H(v) coefficients (b_j; j=1,2,3). We chose the $b_{1,2,3}$ and substitute in Eq. (B.12) to eliminate the quadratic terms. Finally we obtain the normal form of the Hopf bifurcation as:

$$\dot{v} = \omega v + \beta\tilde{\mu}v + p_1 v^3 + p_2 v^2\bar{v} + p_3\bar{v}^2 v + p_4\bar{v}^3 \tag{B.13}$$

Note that the remaining terms cannot be eliminated through a new near-identity transformation, since they are so called resonance terms and Eq. (B.13) is the simplest possible form of the original equation (Eq. B.3). Figure .B.2 indicates that bifurcation diagram of the original system and the reduced model are qualitatively the same. Specifically for small $\tilde{\mu}$, where polynomial approximations are valid, they are well matched. Moreover, Fig .B.3 compares the BM time response for the approximate and original models and demonstrates a good agreement.

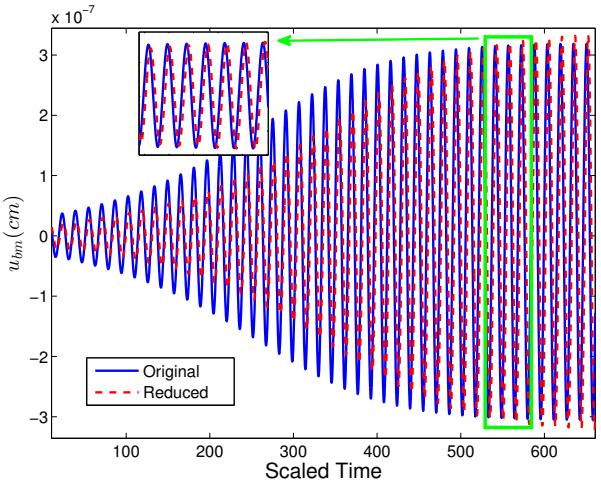

Figure B.3: Exact and approximate solution for the BM displacement; $\varepsilon_3 = -0.04$, $\tilde{\mu} = 0.1$

BIBLIOGRAPHY

[1] Jean-Yves Tinevez, Frank Jülicher, and Pascal Martin. Unifying the various incarnations of active hair-bundle motility by the vertebrate hair cell. *Biophysical journal*, 93(11):4053–67, 2007.

[2] Dáibhid O Maoiléidigh and Frank Jülicher. The interplay between active hair bundle motility and electromotility in the cochlea. *The Journal of the Acoustical Society of America*, 128(3):1175–90, 2010.

[3] Dylan K Chan and A J Hudspeth. Ca2+ currentdriven nonlinear amplification by the mammalian cochlea in vitro. *Nature Neuroscience*, pages 149–155, 2005.

[4] Dylan K Chan and A J Hudspeth. Mechanical responses of the organ of corti to acoustic and electrical stimulation in vitro. *Biophysical Journal*, 89:4382–4395, 2005.

[5] A. J. Hudspeth and Dylan K. Chan. An experimental preparation of the mammalian cochlea that displays compressive nonlinearity in vitro. *Auditory Mechanisms: Processes and Models*, pages 127–137, 2006.

[6] Robert Szalai, Alan Champneys, Martin Homer, Daibhid O. Maoileidigh, Helen Kennedy, and Nigel Cooper. Comparison of nonlinear mammalian cochlear-partition models. *Journal of the Acoustical Society of America*, 133(1):323–336, January 2013.

[7] Thomas Gold. Hearing. ii. the physical basis of the action of the cochlea. *Proceedings of the Royal Society of London B: Biological Sciences*, 135(881):492–498, 1948.

[8] BM Johnstone and AJF Boyle. Basilar membrane vibration examined with the mössbauer technique. *Science*, 158(3799):389–390, 1967.

[9] William S Rhode. Observations of the vibration of the basilar membrane in squirrel monkeys using the mössbauer technique. *The Journal of the Acoustical Society of America*, 49(4B):1218–1231, 1971.

[10] D T Kemp. Stimulated acoustic emissions from within the human auditory system. *JASA*, 64(5):1386–1391, 1978.

[11] AJ Hudspeth. Integrating the active process of hair cells with cochlear function. *Nature Reviews Neuroscience*, 15(9):600–614, 2014.

[12] Pascal Martin and AJ Hudspeth. Active hair-bundle movements can amplify a hair cells response to oscillatory mechanical stimuli. *Proceedings of the National Academy of Sciences*, 96(25):14306–14311, 1999.

[13] Helen J Kennedy, Michael G Evans, Andrew C Crawford, and Robert Fettiplace. Fast adaptation of mechanoelectrical transducer channels in mammalian cochlear hair cells. *Nature neuroscience*, 6(8):832–836, 2003.

[14] Sripriya Ramamoorthy and Alfred L. Nuttall. Outer hair cell somatic electromotility in vivo and power transfer to the organ of corti. *Biophysical Journal*, 102(3):388–398, February 2012.

[15] Peter Mombaerts Local. Prestin is required for electromotility of the outer hair cell and for the cochlear amplifier. *Nature*, 419(September):300–304, 2002.

[16] Peter Dallos, Xudong Wu, Mary Ann Cheatham, Jiangang Gao, Jing Zheng, Charles T. Anderson, Shuping Jia, Xiang Wang, Wendy H Y Cheng, Soma Sengupta, David Z Z He, and Jian Zuo. Prestin-Based Outer Hair Cell Motility Is Necessary for Mammalian Cochlear Amplification. *Neuron*, 58(3):333–339, 2008.

[17] Joseph Santos-Sacchi, Lei Song, Jiefu Zheng, and Alfred L Nuttall. Control of mammalian cochlear amplification by chloride anions. *Journal of Neuroscience*, 26(15):3992–3998, 2006.

[18] Peter Dallos. Cochlear amplification, outer hair cells and prestin. *Current opinion in neurobiology*, 18(4):370–376, 2008.

[19] David ZZ He, Kirk W Beisel, Lin Chen, Da-Lian Ding, Shuping Jia, Bernd Fritzsch, and Richard Salvi. Chick hair cells do not exhibit voltage-dependent somatic motility. *The Journal of physiology*, 546(2):511–520, 2003.

[20] W. E. Brownell P. Dallos K. Dierkes R. Fettiplace K. Grosh C. M. Hackney A. J. Hudspeth F. Juelicher B. Lindner P. Martin J. Meaud C. Petit J. R. Santos Sacchi J. Ashmore, P. Avan and B. Canlon. The remarkable cochlear amplifier. *Hearing Research*, 266:1–17, 2010.

[21] J H Nam and R Fettiplace. Theoretical Conditions for High-Frequency Hair Bundle Oscillations in Auditory Hair Cells. *Biophys. J.*, 95(10):4948–4962, 2008.

[22] HJ J Kennedy, AC C Crawford, and R Fettiplace. Force generation by mammalian hair bundles supports a role in cochlear amplification. *Nature*, 433(February):880–884, 2005.

[23] Stuart L Johnson, Maryline Beurg, Walter Marcotti, and Robert Fettiplace. Prestin-driven cochlear amplification is not limited by the outer hair cell membrane time constant. *NEURON*, 70(6):1143–1154, jun 2011.

[24] D Bertrand W. E. Brownell C. R. Bader and Y. D. Ribaupierre. Evoked mechanical responses of isolated cochlear hair cells. *Science*, 227:194–196, 1985.

[25] Julien Meaud and Karl Grosh. Response to a pure tone in a nonlinear mechanical-electrical-acoustical model of the cochlea. *Biophysical Journal*, 102:1237–1246, 2012.

[26] A. J. Hudspeth. Making an effort to listen: Mechanical amplification in the ear. *Neuron*, 59(4):530–545, August 2008.

[27] S. Ramamoorthy, K. Grosh, and T. G. Nawar. A mechano-electro-acoustical model for the cochlea: Response to acoustic stimuli. *Journal of the Acoustical Society of America*, 121(5):2758–2773, 2007.

[28] Pascal Martin and AJ Hudspeth. Active hair-bundle movements can amplify a hair cells response to oscillatory mechanical stimuli. *Proceedings of the National Academy of Sciences*, 96(25):14306–14311, 1999.

[29] J. Howard and A. J. Hudspeth. Compliance of the hair bundle associated with gating of mechanoelectrical transduction channels in the bullfrog's saccular hair cell. *Neuron*, 1(3):189–199, 1988.

[30] Jonathan AN Fisher, Fumiaki Nin, Tobias Reichenbach, Revathy C Uthaiah, and AJ Hudspeth. The spatial pattern of cochlear amplification. *Neuron*, 76(5):989–997, 2012.

[31] M Charles Liberman, Jiangang Gao, David ZZ He, Xudong Wu, Shuping Jia, and Jian Zuo. Prestin is required for electromotility of the outer hair cell and for the cochlear amplifier. *Nature*, 419(6904):300–304, 2002.

[32] Shuping Jia and David ZZ He. Motility-associated hair-bundle motion in mammalian outer hair cells. *Nature neuroscience*, 8(8):1028–1034, 2005.

[33] Helen J Kennedy, Michael G Evans, Andrew C Crawford, and Robert Fettiplace. Depolarization of cochlear outer hair cells evokes active hair bundle motion by two mechanisms. *Journal of Neuroscience*, 26(10):2757–2766, 2006.

[34] Tianying Ren, Wenxuan He, Yizeng Li, Karl Grosh, and Anders Fridberger. Light-induced vibration in the hearing organ. *Scientific Reports*, 4:5941, August 2014.

[35] H Duifhuis, HW Hoogstraten, SM Van Netten, RJ Diependaal, and W Bialek. Modelling the cochlear partition with coupled van der pol oscillators. In *Peripheral Auditory Mechanisms*, pages 290–297. Springer, 1986.

[36] V M Eguíluz, M Ospeck, Y Choe, a J Hudspeth, and M O Magnasco. Essential nonlinearities in hearing. *Physical review letters*, 84(22):5232–5235, 2000.

[37] Marcelo O Magnasco. A wave traveling over a hopf instability shapes the cochlear tuning curve. *Physical review letters*, 90(5):058101, 2003.

[38] D O Kim, C E Molnar, and R R Pfeiffer. A system of nonlinear differential equations modeling basilar-membrane motion. *J Acoust Soc Am*, 54(6):1517–1529, 1973.

[39] ó Maoiléidigh D. Kennedy H. Cooper N. Champneys A. R. Szalai, R. and M Homer. On the origins of the compressive cochlear nonlinearity. *Preprint, University of Bristol, UK*, pages 1–40, 2011.

[40] Víctor M Eguíluz, Mark Ospeck, Y Choe, AJ Hudspeth, and Marcelo O Magnasco. Essential nonlinearities in hearing. *Physical Review Letters*, 84(22):5232, 2000.

[41] AJ Hudspeth. Integrating the active process of hair cells with cochlear function. *Nature Reviews Neuroscience*, 15(9):600–614, 2014.

[42] AJ Hudspeth, Frank Jülicher, and Pascal Martin. A critique of the critical cochlea: Hopfa bifurcationis better than none. *Journal of neurophysiology*, 104(3):1219–1229, 2010.

[43] Amir Nankali, Karl Grosh, K Domenica Karavitaki, and David P Corey. On the stability and compressive nonlinearity of a physiologically based model of the cochlea. In *AIP Conference Proceedings*, volume 1703, page 070016. AIP Publishing, 2015.

[44] Luis Robles and Mario a. Ruggero. Mechanics of the mammalian cochlea. *Physiological Reviews*, 81:1305–1352, 2001.

[45] Amir Nankali and Karl Grosh. Stability and bifurcation analysis of a nonlinear cochlear model. In *Proceedings of the ASME International Design Engineering Technical Conferences and Computers and Information in Engineering Conference,*, volume 8. ASME, 2014.

[46] Luzyanina T. Engelborghs, K. and D. Roose. Numerical bifurcation analysis of delay differential equations using dde-biftool. *ACM Transactions on Mathematical Software*, 28:1–21, 2002.

[47] Marcia M Mellado Lagarde, Markus Drexl, Victoria A Lukashkina, Andrei N Lukashkin, and Ian J Russell. Outer hair cell somatic, not hair bundle, motility is the basis of the cochlear amplifier. *Nature neuroscience*, 11(7):746–748, 2008.

[48] Fumiaki Nin, Tobias Reichenbach, Jonathan A. N. Fisher, and A. J. Hudspeth. Contribution of active hair-bundle motility to nonlinear amplification in the mammalian cochlea. *Proceedings of the National Academy of Sciences*, 109(51):21076–21080, 2012.

[49] Jiefu Zheng, Niranjan Deo, Yuan Zou, Karl Grosh, and Alfred L Nuttall. Chlorpromazine alters cochlear mechanics and amplification: in vivo evidence for a role of stiffness modulation in the organ of corti. *Journal of neurophysiology*, 97(2):994–1004, 2007.

[50] Nigel P Cooper. Harmonic distortion on the basilar membrane in the basal turn of the guinea-pig cochlea. *The Journal of physiology*, 509(1):277–288, 1998.

[51] Julien Meaud and Karl Grosh. Coupling active hair bundle mechanics, fast adaptation, and somatic motility in a cochlear model. *Biophysical Journal*, 100(11):2576–2585, June 2011.

[52] Wei Dong and Elizabeth S. Olson. Detection of cochlear amplification and its activation. *Biophysical Journal*, 105:1067–1078, 2013.

[53] Hee Yoon Lee, Patrick D Raphael, Anping Xia, Jinkyung Kim, Nicolas Grillet, Brian E Applegate, Audrey K Ellerbee Bowden, and John S Oghalai. Two-dimensional cochlear micromechanics measured in vivo demonstrate radial tuning within the mouse organ of corti. *Journal of Neuroscience*, 36(31):8160–8173, 2016.

[54] Jiefu Zheng, Niranjan Deo, Yuan Zou, Karl Grosh, and Alfred L Nuttall. Chlorpromazine alters cochlear mechanics and amplification: in vivo evidence for a role of stiffness modulation in the organ of corti. *Journal of neurophysiology*, 97(2):994–1004, 2007.

[55] Graeme K Yates and Brian M Johnstone. Localized cochlear microphonics recorded from the spiral lamina. *The Journal of the Acoustical Society of America*, 59(2):476–479, 1976.

[56] Julien Meaud and Karl Grosh. Effect of the attachment of the tectorial membrane on cochlear micromechanics and two-tone suppression. *Biophysical Journal*, 106:1398–1405, 2014.

[57] Anthony W. Gummer, Werner Hemmert, and Hans-Peter Zenner. Resonant tectorial membrane motion in the inner ear: Its crucial role in frequency tuning. *PNAS*, 93:8727–8732, 1996.

[58] JJ Zwislocki. Five decades of research on cochlear mechanics. *The Journal of the Acoustical Society of America*, 67(5):1679–1685, 1980.

[59] Jont B Allen. Cochlear micromechanicsa physical model of transduction. *The Journal of the Acoustical Society of America*, 68(6):1660–1670, 1980.

[60] Andrei N. Lukashkin, Guy P. Richardson, and Ian J. Russell. Multiple roles for the tectorial membrane in the active cochlea. *Hearing Research*, 266(1-2):26–35, July 2010.

[61] Peter Dallos and Burt N. Evans. High-frequency motility of outer hair cells and the cochlear amplifier. *Science*, 267(5206):2006–2009, 1995.

[62] Jiefu Zheng Ning Hu Yuan Zou Tianying Ren Anders Fridberger, Jacques Boutet de Monvel and Alfred Nuttallr. Organ of corti potentials and the motion of the basilar membrane. *The Journal of Neuroscience*, 24(45):10057–10063, 2004.

[63] K. H. Iwasa and M. Adachi. Force generation in the outer hair cell of the cochlea. *Biophysical Journal*, 73(1):546–555, July 1997.

[64] Yanli Wang, Charles R. Steele, and Sunil Puria. Cochlear outer-hair-cell power generation and viscous fluid loss. *Scientific Reports*, 6:19475, January 2016.

[65] Werner Hemmert Gerhard Frank and Anthony W. Gummer. Limiting dynamics of high-frequency electromechanical transduction of outer hair cells. *PNAS*, 96:4420–4425, 1999.

[66] M. Kossl and I. J. Russell. The phase and magnitude of hair cell-receptor potentials and frequency tuning in the guinea-pig cochlea. *Journal of Neuroscience*, 12(5):1575–1586, May 1992.

[67] Sripriya Ramamoorthy Anders Fridberger Niloy Choudhury Steven L. Jacques Ruikang K. Wang Alfred L. Nuttall Dingjun Zha, Fangyi Chen. In vivo outer hair cell length changes expose the active process in the cochlea. *PlosOne*, 7(4):1–9, 2012.

[68] Maryline Beurg, Michael G. Evans, Carole M. Hackney, and Robert Fettiplace. A large-conductance calcium-selective mechanotransducer channel in mammalian cochlear hair cells. *Journal of Neuroscience*, 26(43):10992–11000, 2006.

[69] Roozbeh Ghaffari, Alexander J. Aranyosi, and Dennis M. Freeman. Longitudinally propagating traveling waves of the mammalian tectorial membrane. *PNAS*, 104(42):16510–16515, 2007.

[70] M. Ulfendahl, A. Flock, and S. M. Khanna. A temporal bone preparation for the study of cochlear micromechanics at the cellular-level. *Hearing Research*, 40(1-2):55–64, June 1989.

[71] Ingo Ulrik Teudt and Claus-Peter Richter. The hemicochlea preparation of the guinea pig and other mammalian cochleae. *Journal of Neuroscience Methods*, 162(1-2):187–197, May 2007.

[72] X. T. Hu, B. N. Evans, and P. Dallos. Direct visualization of organ of corti kinematics in a hemicochlea. *Journal of Neurophysiology*, 82(5):2798–2807, November 1999.

[73] Manuela Nowotny and Anthony W. Gummer. Nanomechanics of the subtectorial space caused by electromechanics of cochlear outer hair cells. *PNAS*, 2006.

[74] MJ Tunstall, JE Gale, and JF Ashmore. Action of salicylate on membrane capacitance of outer hair cells from the guinea-pig cochlea. *The Journal of physiology*, 485(3):739–752, 1995.

[75] T Kimitsuki, T Nakagawa, K Hisashi, S Komune, and T Uemura. The effects of ototoxic drugs on mechano-electric transduction channels in chick cochlear hair cells. *European archives of oto-rhino-laryngology*, 251:S53–S56, 1994.

[76] Ellen A Lumpkin, Robert E Marquis, and AJ Hudspeth. The selectivity of the hair cells mechanoelectrical-transduction channel promotes ca2+ flux at low ca2+ concentrations. *Proceedings of the National Academy of Sciences*, 94(20):10997–11002, 1997.

[77] Von Bekesy G. *Experiments in Hearing*. McGrawHill, New York, 1960.

[78] T Y Ren. Longitudinal pattern of basilar membrane vibration in the sensitive cochlea. *Proc. Natl. Acad. Sci. U. S. A.*, 99:17101–17106, 2002.

[79] Guangjian Ni and Stephen J. Elliott. Comparing methods of modeling near field fluid coupling in the cochlea. *Journal Of The Acoustical Society Of America*, 137(3):1309–1317, MAR 2015.

[80] Frank M. White. *Fluid Mechanics*. Number ISBN 0-07-240217-2. McGrawHill, 2003.

[81] Lawrence E. Kinsler, Austin R. Frey, Alan B. Coppens, and James V. Sanders. *Fundamentals of Acoustics*. ISBN 978-0471847892. Wiley, 1999.

[82] E. S. Olson and D. C. Mountain. Invivo measurement of basilar-membrane stiffness. *Journal of the Acoustical Society of America*, 89(3):1262–1275, March 1991.

[83] G. Emadi, C. P. Richter, and P. Dallos. Stiffness of the gerbil basilar membrane: Radial and longitudinal variations. *Journal of Neurophysiology*, 91(1):474–488, January 2004.

[84] Ram C. Naidu and David C. Mountain. Basilar membrane tension calculations for the gerbil cochlea. *Journal of the Acoustical Society of America*, 121(2):994–1002, February 2007.

[85] C. R. Steele and L. A. Taber. Comparison of wkb calculations and experimental results for three-dimensional cochlear models. *Journal of the Acoustical Society of America*, 65:1007–1018, 1979.

[86] Amir Nankali and Karl Grosh. Simulating the chan-hudspeth experiment on an active excised cochlear segment. *The Journal of the Acoustical Society of America*, 2017.

[87] John A Assad, Gordon MG Shepherd, and David P Corey. Tip-link integrity and mechanical transduction in vertebrate hair cells. *Neuron*, 7(6):985–994, 1991.

[88] F Jørgensen and H Ohmori. Amiloride blocks the mechano-electrical transduction channel of hair cells of the chick. *The Journal of Physiology*, 403(1):577–588, 1988.

[89] E. K. Dimitriadist R. S. Chadwickt and K. H. Iwasa. Active control of waves in a cochlear model with subpartitions. *Proc. Natl. Acad. Sci*, 93:2564–2569, 1996.

[90] Lei Cheng. *Cochlear-based transducers: Modeling and design.* PhD thesis, 2007.

[91] J. Meaud and K. Grosh. The effect of tectorial membrane and basilar membrane longitudinal coupling in cochlear mechanics. *J. Acoust. Soc. Am.*, 127(3):1411–1421, 2010.

[92] Andrei N Lukashkin, P Kevin Legan, Thomas D Weddell, Victoria A Lukashkina, Richard J Goodyear, Lindsey J Welstead, Christine Petit, Ian J Russell, and Guy P Richardson. A mouse model for human deafness dfnb22 reveals that hearing impairment is due to a loss of inner hair cell stimulation. *Proceedings of the National Academy of Sciences*, 109(47):19351–19356, 2012.

[93] Tianying Ren, Wenxuan He, and Peter G. Barr-Gillespie. Reverse transduction measured in the living cochlea by low-coherence heterodyne interferometry. *Nature communications*, 7:10282–10282, January 2016.

[94] David Strelioff. A computer simulation of the generation and distribution of cochlear potentials. *The Journal of the Acoustical Society of America*, 54(3):620–629, 1973.

[95] Paul D Teal and Guangjian Ni. Finite element modelling of cochlear electrical coupling. *The Journal of the Acoustical Society of America*, 140(4):2769–2779, 2016.

[96] Ali H Nayfeh and Dean T Mook. *Nonlinear oscillations*. John Wiley & Sons, 2008.